A COMPUTATIONAL MAGNETOHYDRODYNAMIC MODEL OF A GASDYNAMIC FUSION SPACE PROPULSION SYSTEM

by

Chad J. R. Ohlandt

A dissertation submitted in partial fulfillment
of the requirements for the degree of
Doctor of Philosophy
(Aerospace Engineering and Scientific Computing)
in The University of Michigan
2011

Doctoral Committee:

Professor Kenneth G. Powell, Chairperson
Professor Iain D. Boyd
Professor Alec D. Gallimore
Professor James P. Holloway

To my wife, D. M. R. Ohlandt, for her nearly infinite patience with me and this thesis. To my parents, Herb C. and Carol W. Ohlandt, for their support through many, many years of education. To my grandparents, Herbert I. Ohlandt, Marilyn J. Ohlandt, Howard E. Weidman, and Velma C. Weidman, whose values and work ethic set this all in motion.

ACKNOWLEDGEMENTS

Thanks to my advisor, Professor Ken Powell, for his continued support over the years leading to the completion of this work.

Thanks to Professor Terry Kammash for getting me started on gasdynamic mirrors and nuclear fusion space propulsion systems.

Thanks to fellow members of the CFD group who contributed directly and indirectly to my education and this work, including Eric Charlton, Timur Linde, Jeff Benko, Jeff Hittinger, and David Mott.

TABLE OF CONTENTS

LIST OF FIGURES

LIST OF TABLES

LIST OF APPENDICES

CHAPTER I

INTRODUCTION

1.1 Motivation

1.1.1 Advanced Space Propulsion

It's been over 40 years since the first human walked on the Moon, yet little progress has been made towards the human exploration and settlement of Mars. The discovery of extra-solar planets by astronomic observation has become almost routine, yet the first and only probe sent to Pluto is not expected to arrive until 2015, after being launched in 2006. A key limiting factor in the exploration of our solar system is interplanetary space propulsion.

In the 20th century, great advances in chemical rockets enabled space probes and humans to escape Earth's atmosphere. While these high-thrust systems have the power (joules/second) to accelerate spacecraft into orbit and beyond, they are fundamentally energy (joules) limited by the energy density of chemical fuels. Like a V8 car engine, they have lots of power, but very poor gas mileage or, in propulsion parlance, poor specific impulse, I_{sp}. Far more efficient advanced electric propulsion systems that depend on solar power cells are effectively energy unlimited, but these low thrust systems are power limited. Their specific power being constant; solar powered electric propulsion power levels scale with the mass of the solar panels and

associated power conversion equipment. In order to achieve the propulsive power and energy requirements suited for accelerated interplanetary exploration, one needs to consider nuclear power propulsion.

Nuclear space propulsion comes in a number of flavors. Most concepts can be cataloged by two traits, whether they are fission/fusion and whether they are closed/open. Closed systems would include nuclear fission electric reactors that provide power to some form of electric propulsion system. The increased specific power of nuclear electric power sources certainly enables electric propulsion systems with greater thrust, but the mass of nuclear electric power systems and associated shielding does limit their potential. Theoretically, nuclear fusion electric power systems might improve the specific power available, but this has yet to be demonstrated in the laboratory setting.

Open systems directly expel the reactors' plasma or coolant as propellant. NASA's most recent Mars baseline mission plan calls for nuclear fission thermal propulsion systems.[14] Such systems were designed and tested in the 1960s, but never flown. Typically, a hydrogen propellant flows through a nuclear fission reactor and exhausts out a traditional rocket nozzle. They can deliver high-thrust with specific impulse close to double that of chemical propulsion, but the material thermal limits bound performance to that level. Lastly, open nuclear fusion systems offer the potential for revolutionary propulsion systems with high thrust and high efficiency. The gasdynamic mirror (GDM) fusion space propulsion system is one such open fusion reactor where the fusion plasma is exhausted out a magnetic nozzle to produce thrust. GDMs are high-thrust systems that are potentially 100 times more specific impulse than even nuclear thermal propulsion.

1.1.2 Gasdynamic Mirror Developments

Kammash published the original GDM concept [22, 23], which is described in detail in Chapter II. In short, using only analytical models, Kammash demonstrated that GDMs are physically feasible, although they require advanced magnet and radiative cooling technology that is not yet available. Even with the development of those technologies, the systems are likely very large, in the 100s of metric tons, but are plausible given a heavy lift vehicle such as the Saturn V or a proposed NASA heavy lift vehicle, such as Ares V or Shuttle-C.

More recently, limited experimental research has been conducted on non-fusion capable GDM configurations. Emrich built an experimental GDM setup at NASA Marshall to test plasma stability. [15, 16] His work does suggest that there are instability challenges in simple GDM configurations due to bad magnetic curvature. Past fusion power research has documented similar instabilities and proposed numerous potential solutions to improve stability.

Plasma rockets, which are very similar to GDMs but not fusion capable, have made steady progress in the last decade. Chang-Diaz continues to develop the Variable Specific Impulse Magnetoplasma Rocket (VASIMR) system.[8, 7] VASIMR is a non-fusion plasma rocket, with a magnetic confinement and nozzle system. Technologies being matured and lessons being learned in VASIMR development will be broadly applicable to future GDM implementations, if GDMs are shown to be practical. Additionally, plasma rockets similar to VASMR that are “turbo-charge” with unsteady fusion energy injections may provide a viable development path to fully capable GDM systems.

1.1.3 Computational Magnetohydrodynamics

Computational fluid dynamics (CFD) models are routinely used in aerospace, automotive, and other fields for preliminary design work. CFD is a cost effective approach to eliminate poor designs. Resources, both time and money, can then be focused on the most promising design concepts. Given the costs and safety issues surrounding nuclear fusion experiments, a CFD approach for a GDM is quite logical.

The nuclear fusion physics community has certainly used computational models in the efforts to understand and predict nuclear fusion plasmas. However, their models tend to be highly focused physics models created to shed light on fundamental plasma physics behavior, which often makes them unsuitable for systems design work. Additionally, they generally focus on low density plasmas where the mean free path is not much less than the characteristic length of containment.

At the University of Michigan, significant progress has been made in magnetohydrodynamic (MHD) modeling of the solar wind and space weather.[34, 28, 13] While the plasmas are certainly low density, the length scales make continuum CFD approaches viable. In fully ionized plasmas, Coulombic or electrostatic forces are dominant in particle collisions as the electrostatic potential is felt at greater distances than van der Waals or Pauli atomic forces. Given the greater range of electrostatic particle collisions, ionized plasmas can be treated as continuum flows and modeled with MHD at lower densities than non-ionized gases. The relatively high density plasmas found in GDMs makes this particularly true, where the mean free path is much less than the length of the GDM.

An independent line of inquiry in numerical modeling at the University of Michigan revolved around modeling complex geometries with Cartesian grids and traditional finite-volume Euler solvers.[12, 3, 4, 9] Methods for adaptive refinement were

developed in 2-D grids and extended to 3-D. The ability to rapidly generate geometries based on geometric parameters, rather than complex design drawing tools, was also established. All of these capabilities are applicable to the geometries of ring magnets and radiator panels of GDMs, as well as other electric propulsion systems such as arcjets or magnetoplasmadynamic thrusters.

1.2 Objectives and Scope of the Work

The goal of this work is to advance our understanding of GDMs as potential interplanetary space propulsion systems, initially with analytical models and ultimately by developing an ideal MHD tool for designing complex 3-D GDM concepts. The starting point was to extend Kammash's analytical model to explore alternative GDM configurations with advanced fusion fuels and supplemental nuclear electric power. Next to move beyond the analytical model by developing a 3-D MHD modeling tool to allow the exploration of alternative GDM concepts. Many challenges and solutions to numerically modeling GDMs are addressed in this work.

The computational model aspects include:

1. three-dimensional adaptive Cartesian gridding
2. arbitrary geometric and magnetic field configurations
3. ideal MHD finite-volume, characteristic-based, high-resolution flow-solver
4. explicit and implicit iterative algorithms
5. parallel implementation of the implicit scheme

Extremely fast wave speeds with very small length scales aggravated the naturally slow relaxation time of large GDM systems. While too computationally demanding

for system design studies given available resources, MHD computational results presented here provide new insights into the energy losses in the GDMs. The understanding of the computational bottlenecks for GDM simulations developed in this work also suggests potential future approaches that are likely to produce effective design tools.

1.3 Organization of Dissertation

Chapter II Gasdynamic Mirror Space Propulsion Systems reviews the GDM concept in detail highlighting their potential and their pitfalls. Past work and results on GDMs by Kammash are documented. Chapter III Parametric Studies of Advanced Fusion Fuel Gasdynamic Mirror Systems extends Kammash's analytical model with new work on advanced fusion fuel, proton-^{11}boron, and the potential for nuclear electric driven GDM systems. Chapter IV Computational Magnetohydrodynamic Modeling Tool describes the ideal-MHD finite-volume algorithm with Cartesian grids and adaptive refinement. Chapter V MHD Computational Results documents the computational results including validation with shock polars, a simulation of Emrich's experimental GDM that is not fusion capable, and Kammash's $deuterium - tritium$ GDM concept. Chapter VI Conclusions summarizes the collective findings of this research on GDMs.

The author's new contributions form the bulk of Chapters III, IV, and V. Chapter III involves new optimization studies of $p-^{11}B$ GDMs and a modification of the Kammash model to account for externally driven GDMs. Chapter IV describes how the author adapted an Euler 3-D Cartesian adaptive-grid finite-volume CFD code and MHD Roe-approximate explicit flux solvers to modeling GDMs, and then implemented new algorithms for stretched grid cells, arbitrary background magnetic fields,

and a parallel implicit MHD with split magnetic field solver. Chapter V includes the author's findings when comparing the MHD model's results with experiment and previous GDM performance estimates.

CHAPTER II

GASDYNAMIC MIRROR SPACE PROPULSION SYSTEMS

2.1 Introduction

In space propulsion, as with automobiles, the key performance parameters are thrust and specific impulse, or horsepower and gas mileage. The various space propulsion options offer an engineering trade between these two factors. Chemical rockets offer thrust levels up to millions of Newtons (1.25×10^7 Newtons per Space Shuttle Rocket Booster (SRB)), but with less than stellar specific impulses between 200 and 450 seconds. Advanced electric propulsion systems offer much higher specific impulses, 600-10,000 seconds, but their thrusts levels are often measured in milli-Newtons.

To break out of this paradigm, we look to revolutionary technologies such as nuclear fission or nuclear fusion. Nuclear fission rockets have been developed and even tested.[1] However, most nuclear fission propulsion system designs still require a propellant to flow through a physical structure that contains the radioactive fuel rods which limits the temperatures to roughly 3000K and the specific impulse to 900 seconds. Designs where the radioactive fuel is suspended in the propellant have been proposed and studied, but have many engineering challenges.[37, 38, 24] Nu-

clear fusion propulsion systems offer another option for high thrust and high specific impulse systems. Nuclear fusion can be instigated using inertial or magnetic confinement methods. Inertial systems are generally pulsed and require a high level of precision to operate. This makes them less than ideal for a space propulsion system, although not completely unfeasible. Magnetic confinement fusion has been well-studied and verified with numerous experimental devices over the past half century. Magnetic confinement systems are divided into two classes, open and closed. In closed systems, the fusion plasma is completely contained by the magnetic fields and energy is recovered mostly from the escape of high energy neutrons captured in shielding surrounding the plasma as heat. Currently, they are the most studied and are considered the most promising for terrestrial energy production. Open systems do vent plasma from the magnetic containment field in addition to producing neutrons and electromagnetic radiation. In relation to space propulsion, open magnetic confinement fusion plasmas can theoretically produce propulsion systems with thrust levels of 10,000s-100,000s of Newtons and a specific impulse of 100,000s of seconds as well.

One such open magnetic confinement fusion space propulsion system is the gasdynamic mirror proposed by Kammash.[22] The gasdynamic mirror fusion space propulsion concept originated with magnetic mirror fusion energy experiments. Fusion mirror concepts involve containing a plasma between two magnetic mirrors. While the open confinement magnetic field of standard mirror devices are simpler and more stable than closed confinement devices such as tokamaks or stellarators, they suffer the natural loss of plasma and energy from the openings in the magnetic field. Traditional mirror fusion device designs assume low density collisionless plasmas to minimize the loss of plasma and energy escaping from the mirrors.

Unfortunately, this introduces micro-instabilities from the resulting non-Maxwellian velocity distribution. Since a propulsion system derives its power from the 'loss' of plasma, Kammash conceived of a gasdynamic tandem mirror propulsion system. With enough particle collisions that it remains Maxwellian and stable, the gasdynamic mirror (GDM) propulsion system's increased plasma loss at the mirrors simply results in greater thrust and a more powerful rocket.

Kammash developed a parametric model for GDM propulsion systems to determine their potential and produce preliminary designs.[22, 23] This chapter provides background on magnetic mirrors and Kammash's GDM model and explores the designs that resulted from Kammash's modeling work.

2.2 Magnetic Mirror Fusion

The simplest magnetic mirror is a ring magnet, where the magnetic field along the axis is strongest at the center of the ring and continually decreases moving away from the ring along the axis. Any charged particle moving towards the center of the ring magnet will feel the increasing gradient of the magnetic field. How it feels the magnetic field depends on the particle's velocity relative to the magnetic field line, see Figure 2.1. The particle's velocity has two components, parallel and perpendicular ($v_{\parallel}$ and $v_{\perp}$), to the magnetic field line that it is attached to. If $v_{\perp} = 0$, then the particle will simply follow the field line at $v_{\parallel}$ passing easily through the ring magnet. If $v_{\parallel} = 0$, then the particle is not moving towards the ring magnet and simply orbits its magnetic field line with the velocity $v_{\perp}$. Usually neither $v_{\parallel}$ nor $v_{\perp}$ is zero, resulting in a particle spiraling around the field line as it approaches the ring magnet. Due to conservation of the magnetic moment, as the particle approaches the magnet mirror it must spin faster around the field line. Then, accounting for the

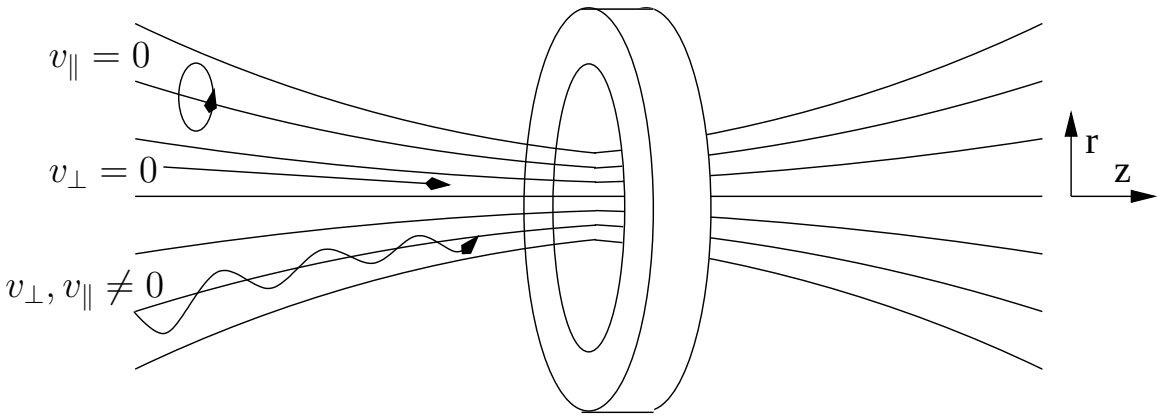

Figure 2.1: Simple ring magnet with moving charged particles.

conservation of energy requires a transfer of parallel kinetic energy into rotational energy. This slowing effect as the particle approaches the ring magnet acts as a force pushing the particle back away from the ring magnet. If $v_\parallel$ becomes zero before reaching the plane of the ring magnet, then the particle will be reflected from the ring magnet or magnetic mirror. Otherwise, the particle will pass through the ring magnet and accelerate back out the other side of the ring magnet.

A simple magnetic mirror confinement system is two such rings placed in series. Under ideal assumptions any charged particle that lacks the velocity parallel to the field lines to escape will simply bounce back and forth between the two mirrors indefinitely. However, simple magnetic mirror systems have two inherent instability issues: micro-instabilities and flute instabilities.

If a low density or collisionless population of particles with a Maxwellian velocity distribution is trapped between two mirrors, the velocity distribution will evolve into a loss cone velocity distribution as particles with larger axial velocities, v_z, escape and those with primarily radial velocities, v_r, remain trapped. Unfortunately, such a velocity distribution as seen in Figure 2.2 turns out to be unstable. Loss cone

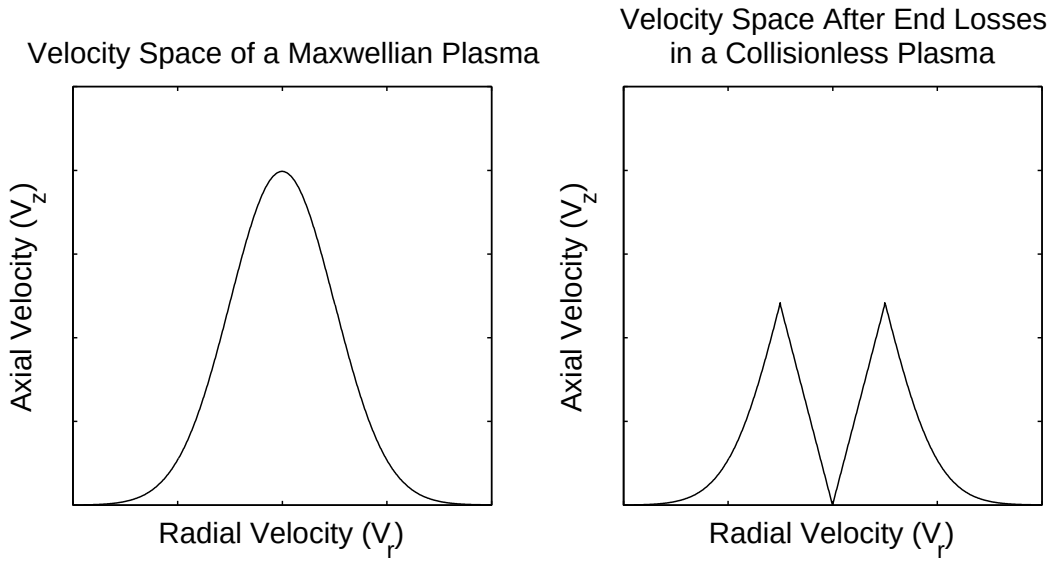

Figure 2.2: Initial Maxwellian velocity distribution and the resulting loss cone distribution due to escaping ions.

instabilities are often referred to as micro-instabilities. In short, micro-instabilities result from resonance between various electromagnetic waves in the plasma and gyrating particles that remain trapped in the mirror device.[2] Increasing the particle density, the plasma is no longer collisionless and the axial velocity space is repopulated. While this avoids the micro-instabilities, the plasma continues to lose mass and energy as particles with significant enough axial velocities escape through the mirrors. The goal of terrestrial fusion power production is to get a plasma hot and dense enough and contain it long enough such that nuclear fusion occurs. With magnetic mirror containment there is an inverse trade off between increasing density and decreasing containment time.

A second problem with simple mirrors is that they contain a region of bad curvature where the magnetic fields of the two mirrors meet. Regions of a magnetic containment field where the field lines appear convex to the plasma are considered

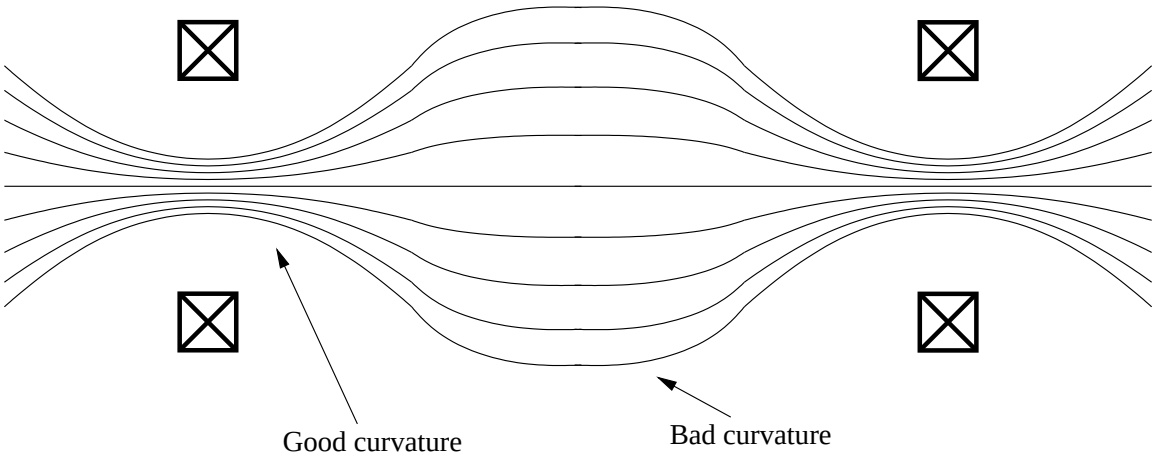

Figure 2.3: Cross section of a simple mirror magnetic field.

regions of bad curvature. Within regions of bad curvature a perturbation of the contained plasma surface can result in a growing flute instability and the loss of containment. Various methods to decrease or eliminate bad curvature have been proposed.[20] Lengthening the containment field with ring magnets or a solenoid magnet will help. Imposing a multipole field, such as Ioffe bars, on top of the mirror fields minimizes bad curvature effects on the surface of the plasma. True magnetic wells, that have no bad curvature, include baseball coils or yin-yang coils. All these solutions greatly increase the complexity of the fusion reactor design and construction. Alternatively, bad curvature effects can be limited by drowning them out with good curvature.[30] To achieve this a greater number of particles must be present in good curvature regions than in bad curvature regions. However, this leads to increasing the plasma density within the mirrors or just outside the mirrors, where the good curvature is present.

Of course, greater density in the mirrors results in greater energy losses as more particles escape, thus limiting the system's production of fusion energy. Proponents of magnetic mirror systems have proposed numerous modifications to improve

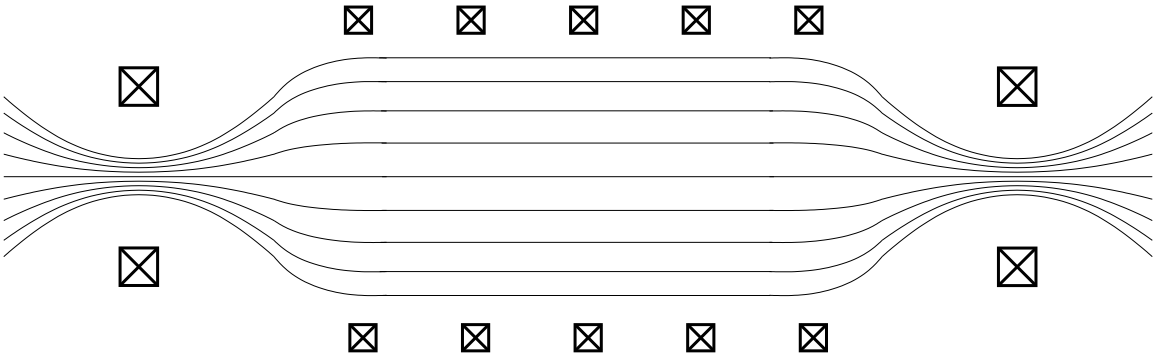

Figure 2.4: Cross section of a lengthened simple mirror magnetic field as used for a gasdynamic mirror.

the containment. Lengthening the distance between the mirrors by inserting ring magnets or a solenoid as seen in Figure 2.4 linearly increases containment time. Putting a number of mirrors in series would increase containment time as well. Creating some sort of plug at the mirror to limit the rate of loss through the mirror has been proposed, including electrostatic, thermal barriers, or field-reversed configurations.[17, 33]

In the 1980s, the U.S. Department of Energy was supporting three major initiatives in fusion research:

- open magnetic confinement (tandem mirrors)
- closed magnetic confinement (tokamaks/stellarators)
- inertial confinement (lasers).

Tandem mirrors are the modern descendants of simple mirror systems. Tandem mirrors generally have non-axisymmetric fields capped with magnetic well mirrors and plugs of various types. Open magnetic confinement systems were deemed the least likely to produce fusion power systems that might compete economically with fossil fuels. Due to budget cuts, the tandem mirror experiment, MFTF-B, at Lawrence

Livermore Labs was mothballed. Tokamaks and laser-based fusion efforts continue through to today, although viable systems have yet to be developed.

Since then, open configuration magnetic confinement research has continued overseas. The Budker Institute of Nuclear Physics in Novosibirsk, Russia, operates three magnetic mirror experiments. GOL-3 is a multi-mirror system, AMBAL-M is an ambipolar trap, and GDT is a gasdynamic trap.[26] In Japan at the University of Tsukuba, they continue to operate GAMMA 10, a relatively traditional tandem mirror.[10] The Korea Basic Science Institute in Daejeon, Korea operates a simple mirror experiment known as HANBIT.[27] Regardless, much of the world's fusion research establishment continues to focus on closed fusion systems and the construction of the new ITER reactor in France.

Of particular interest to our work is the GDT experiment in Novosibirsk. The GDT is a high density mirror system intended to be a compact neutron source for testing materials used in the construction of future fusion reactors. As the only currently active high density plasma mirror experiment, the GDT continues to demonstrate the ability to maintain MHD stability by the presence of plasma in the regions of good curvature. The current goal is proof-of-concept for using a GDT as neutron source for testing reactor materials.

2.3 GDM Fusion Space Propulsion

How can we build a fusion space propulsion system when terrestrial fusion energy production is not yet possible? Some variation of this question is the primary argument against the feasibility of fusion space propulsion. However, the design objectives for fusion energy production and fusion space propulsion have two fundamental differences. In contrast to fusion energy production, fusion space propulsion

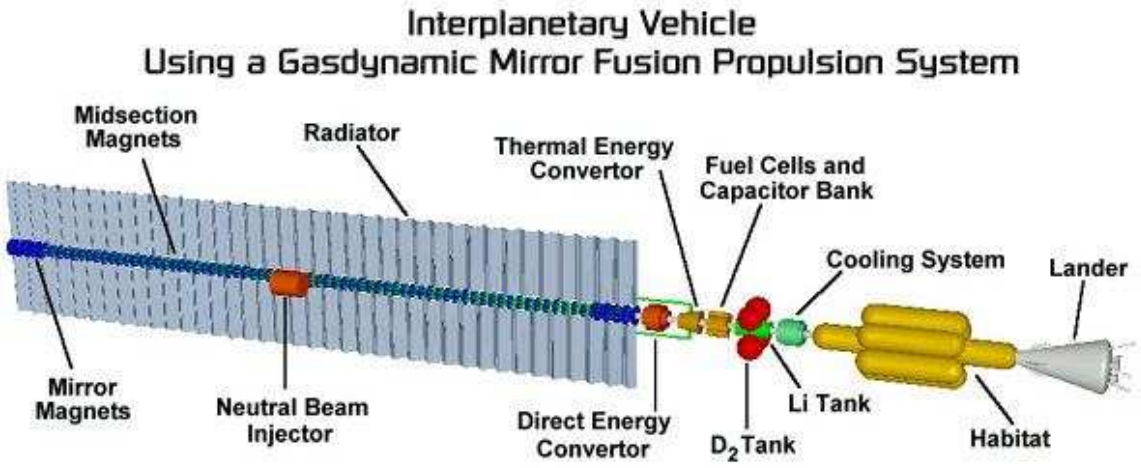

Figure 2.5: Conceptual drawing of a GDM fusion space propulsion system.

systems do not have to be economically competitive. Second, to generate rocket thrust, they must vent to space a significant fraction of the power produced.

First and foremost, fusion energy production must compete economically with other sources of energy such as fossil fuels, nuclear fission, wind, and solar. In order to compete with fossil fuels, the Q factor, P_f/P_i, the fusion power generated over the power injected into the fusion reactor, must be somewhere between 10 and 50. In contrast to such a large Q, a fusion space propulsion system with a mere $Q = .5$ still means 50% more propulsive power than a comparable plasma rocket. A fusion propulsion system with only $Q = 1.2$ would be able to operate in a self-sustaining fashion without any external power source needed to drive it. All the various mirror machine configurations proposed over the years have estimated Q values between 1 and 10 due to the inherent loss of plasma from the open magnetic field configuration. As a result, the US and most of the world's fusion research establishment have ignored magnetic mirror fusion reactors since the late 1980s and pursued closed confinement systems such as tokamaks. This is unfortunate, since any open system with a Q from 1 to 10 would make an ideal space propulsion system.

Second, the open magnetic confinement fusion systems make suitable propulsion systems given the simplicity of ejecting hot plasma from such systems. Traditional mirror fusion reactors would appear to make excellent space propulsion systems. Unfortunately in order to achieve the objective of higher Q values, they are designed to operate in a collisionless regime which produces instabilities described previously. Operating with higher plasma densities is much more stable, but increased plasma leakage decreases Q values to order 1. However, not only can space propulsion systems operate with a Q of 1, but our goal is to use the plasma for thrust. The more plasma 'leaks' from the reactor, the more thrust you get from the rocket.

2.4 Parametric Model

Recognizing that higher density magnetic mirror fusion systems would make suitable propulsion systems, Kammash developed a model and conducted a number of design studies for gasdynamic mirror (GDM) fusion space propulsion systems. Optimizing for a large number of input parameters, including fuel type, density, plasma temperature and mirror ratio, he found a deuterium-tritium fueled GDM weighing 400 metric tons could reach Mars in just over two months.[22] The flight to Mars would involve continuous thrusting, accelerating and decelerating along a straight-line trajectory. Besides the obvious advantage that two months is a fourth of the travel time required for traditional chemical propulsion using an orbit transfer trajectory, a GDM propulsion system could return to Earth in a few months in the event of an emergency while a traditional orbital trajectory would still require over two years to return to Earth following a complete solar orbit.

Kammash's model starts with a simple axisymmetric magnetic mirror with a large aspect ratio, similar to Figure 2.4 but stretched even longer. Generally the plasma

radius, r_p, is a few centimeters, and the length, L, of the plasma column is 10s, 100s, or even 1000s of meters. The plasma density is high enough to ensure that the mean free path is much less than the plasma length, $\lambda \ll L$. Given a gasdynamic regime, the escape of plasma through each end mirror is similar to the escape of gaskinetic particles through a hole into a vacuum. Treating the plasma column as homogeneous in density and temperature and with the radius, r_p, and length, L, you can calculate the mass and energy balance of the system accounting for all losses and gains. Mass is injected in the center, lost through the mirrors, and converted into energy during fusion reactions. Energy is injected, lost through the mirrors with the plasma, produced by fusion reactions, and emitted as bremsstrahlung and synchrotron radiation.

$$L = \frac{(E_{in} - 2T)}{nc_0R(p_0 + s_0T^{1.5} - .25 < \sigma v > (2E_{in} + E_0)T^{-.5})} \tag{2.1}$$

$$E_{in}(Q) = -\frac{\xi}{4} + \sqrt{(\frac{\xi}{4})^2 + \frac{E_0E_L}{2Q}} \tag{2.2}$$

$$\xi = E_0(\frac{1}{Q} + 1) - \frac{4(P_b + P_s)}{n^2 < \sigma v >} \tag{2.3}$$

where the variables are defined in Table 2.1.

Given a set of defined system parameters and assuming a particular Q value, usually 1 or 1.2, iteratively solve the mass and energy conservation equations for different plasma lengths, L, until the required value of Q is achieved. With system length defined, then the total power produced by radiation and neutron losses is tallied. With the dimensions and magnetic field strengths, one can determine the necessary magnet mass. Knowing the thermal power absorbed by the engine from

E_{in}	injection energy
T	plasma temperature
n	particle density
c_0	constant $\sqrt{\pi m/8}$
R	mirror ratio
p_0	constant from bremsstrahlung power equation
s_0	constant from synchrotron power equation
$< \sigma v >$	velocity averaged fusion cross section
E_0	fusion energy
Q	reactor gain factor
P_b	bremsstrahlung radiated power $P_b(T, n)$
P_s	synchrotron radiated power $P_s(T, n)$

Table 2.1: Variable definitions used by Kammash.

the plasma, the mass of the necessary power conversion, shielding, refrigeration and radiator equipment can be computed. Finally combining the total system mass with the generated thrust power, the system performance and travel time to Mars or elsewhere is calculated.

2.5 Baseline GDM System Designs

Kammash and Lee[22] demonstrated that a $D-T$ GDM was conceptually feasible. The first baseline design focused on minimizing the length of the system under the assumption that the major mass driver would be the magnets containing the plasma. Given the space shuttle's ability to deliver 25 t to low earth orbit (LEO), an interplanetary propulsion system of 1847 t seems unreasonable. A new design optimized for total mass rather than length or speed was found. This design has a mass of 295 t. The trip time to Mars increases from 1.7 months to 2.0 months, but it is still far less than the 6-9 months required for chemical propulsion. Parameters for both designs can be found in Table 2.2.

While the new design requires more than 12 shuttle missions to launch, it is less

Optimized for	length	low mass
Reaction Type	$D-T$	$D-T$
Plasma Density	1e+16 $\#/cm^3$	2e+15 $\#/cm^3$
Plasma Temperature	15 keV	10 keV
Beta (vacuum)	0.95	0.95
Plasma Mirror Ratio	50	100
Plasma Mirror Radius	0.01 m	0.005 m
Destination Mars	7.8e+10 m	7.8e+10 m
—Calculated Parameters—		
Vacuum magnetic field, Bp0	11.3 Tesla	4.12 Tesla
Gain Factor, Q	1.0	1.0
Plasma Length, L	31.7 m	107 m
Thrust	2.52e+4 N	3360 N
Total Dry Mass	1847.1 t	295 t
I_{sp}	158,000 s	129,000 s
Round Trip Time	3.4 months	4.1 months
Trip Time AB	1.7 months	2.0 months

Table 2.2: Optimized $D-T$ GDMs.

massive than the International Space Station. Although Ares I, a medium lift launch system for human access to LEO, has been canceled, NASA is expected to go forward with designing a new heavy lift launch vehicle, Ares V, which is expected to launch 125 t to LEO, similar to the ability of the Apollo Project's Saturn V. The low mass design could be easily launched on three Ares V. It is even plausible that the larger GDM designs could be launched to LEO on a few dozen heavy lift vehicles. Keep in mind that the GDM fusion propulsion systems would not be expendable, and with repair and replacement of key components could be used over and over again for supplying a Martian settlement or various interplanetary missions.

Originally, GDMs were expected to be massive simply due to the large magnets required for the containment field. However, the early design work revealed that the mass of the radiators accounted for 75-85% of the system mass. Not the magnet mass, but the radiators were the main driver of a $D-T$ GDM system mass. The

Fuel	Products	Total Energy [MeV]	Charged Particle Energy [MeV]	Optimal Ignition Tempera ture [keV]
$D-T$	$n+^4He$	17.6	3.5	10.5
$D-D$	$p+T$	4.0	4.0	15
	$n+^3He$	3.3	.8	15
$D-^3He$	$p+^4He$	18.3	18.3	60
$^3He-^3He$	$2p+^4He$	12.9	12.9	1000
$p-^{11}B$	3^4He	8.7	8.7	150

Table 2.3: Table of fusion fuels with relevant parameters.

large radiators are necessary in the vacuum of space to remove excess waste heat due to neutron impacts. Alternative fusion fuels that minimize neutron production and energy loss via neutral particles might also minimize the radiator mass.

2.6 Fusion Fuels

Fusion fuel candidates are listed in Table 2.3. With the lowest ignition temperature, a deuterium and tritium GDM is the logical starting point. Kammash determined that D-T GDM optimized for travel time to Mars would be over 1500 tons and arrive at Mars in just under 60 days, while a D-T GDM optimized for total mass might be only 300 tons with a travel time of slightly more than 60 days. The primary disadvantage of D-T is that 80% of the fusion energy produced resides in the neutrons, which are not contained by the magnetic fields. Propulsion system components must be shielded from the neutrons. Although some of the neutron energy can be reclaimed thermodynamically, the majority of it must be radiated into space.

Kammash also considered a $deuterium-^3helium$ GDM. While a $D-^3He$ reaction produces more energy than a $D-T$ reaction and most of it resides in charged particles, the reaction requires a much higher ignition temperature. While this minimizes neutron energy losses, the higher plasma temperature greatly increases

—Input Parameters—			
Reaction Type	$D-T$	$D-^3He$	$p-^{11}B$
Plasma Density	1e+16 $\#/cm^3$	1e+16 $\#/cm^3$	2e+16 $\#/cm^3$
Plasma Temperature	15 keV	100 keV	300 keV
Beta (vacuum)	0.95	0.95	0.95
Plasma Mirror Ratio	50	50	100
Plasma Mirror Radius	0.01 m	0.01 m	0.005 m
Magnet Current Den.	50.0 MA/m^2	50.0	2.5e+08 MA/m^2
Destination Mars	7.8e+10 m	7.8e+10 m	7.8e+10 m
—Calculated Parameters—			
Vacuum magnetic field, Bp0	11.3 Tesla	29.1	80.07 Tesla
Gain Factor, Q	1.0	1.0	1.22222
Plasma Length, L	31.7 m	2857.9 m	23635 m
Thrust	25,200 N	168,000 N	150,985 N
Thrust Power	3.89e+4 MW	6.70e+5 MW	4.44e+05 MW
Fusion Power	9562.5 MW	5.32e+5 MW	2.65e+06 MW
Bremsstrahlung Power	103.3 MW	1.12e+5 MW	4.67e+06 MW
Synchrotron Power	53.1 MW	1.18e+5 MW	1.67e+05 MW
Total Dry Mass	1847.1 t	105,381 t	1.28+06 t
Engine Mass Fraction	0.12	0.38	0.29
Converters Mass Fraction	0.034	0.13	0.30
Radiator Mass Fraction	0.85	0.49	0.41
I_{sp}	158,000 s	407,000 s	693,791 s
Round Trip Time	3.4 months	7.6 months	3.27 years
Trip Time AB	1.7 months	3.8 months	1.63 years

Table 2.4: Optimized $Q > 1$ $p-^{11}B$ GDM.

bremsstrahlung and synchrotron radiation losses. Given the lower reaction rate and the greater radiation losses, the $D-^3He$ systems are much longer and heavier than their $D-T$ counterparts. One example given by Kammash for a $D-^3He$ systems is over 100,000 tons and just under 3km long.

A *proton* and ^{11}*boron* fuel combination has also been suggested. New parametric studies of GDMs operating on $p-^{11}B$ have been conducted by the author and appear in Chapter 3. In brief, they suffer from problems similar to those of the $D-^3He$ GDM. The order-of-magnitude higher plasma temperatures produce more radiation losses.

While it appears that $D-^3He$ and $p-^{11}B$ GDMs fail to offer a feasible alternative to $D-T$ GDMs, that is not the whole story. Kammash's parametric model of a GDM assumes a column of plasma, homogeneous in density and temperature, where fusion reactions occur from random kinetic collisions between the fuel species. Under those conditions, $D-T$ fuels offer a clear advantage. However, if you consider a much cooler plasma, although with a temperature still measured in keV, with the second fuel species injected with a high relative velocity by particle accelerators, you can produce fusion energy at defined locations within the plasma without the radiation losses from heating the whole plasma. The need for a computer simulation to model such systems is the prime driver behind the development of the computer model presented in Chapter 4. Second, the driven nature of fusion energy systems that are dependent on particle accelerators and on the efficiency losses implicit in particle acceleration often results in lower theoretical values of Q. Economically, the lower Qs suggest an inability to compete with other forms of energy production and consequently result in limited interest from the fusion energy research establishment. However, the driven systems with Qs near or below 1 may still produce interesting propulsion systems. New work by the author on driven GDM systems is also presented in Chapter 3.

2.7 Electrostatic Force Effects

While all of the work presented in this thesis assumes a quasi-neutral plasma as a basis for ideal MHD assumptions, in reality the GDM plasma is composed of ions and electrons. The possibility of charge separation and electrostatic forces developing has two significant effects, that must be mentioned, while not explored in this work. Both local and global charge separation may occur in GDM configurations.

Local charge separation on the surface of the plasma can lead to flute instabilities.

Flute instabilities result in the loss of plasma confinement as the electrostatic forces become unstable as they interact with the magnetic fields with bad curvature. Flute instabilities are well documented and well understood by the fusion research establishment. Recent work by Emrich to study plasma stability in a GDM configuration has found that avoiding flute instabilities in GDMs may be harder than anticipated due to the interaction of the magnetic nozzle flow conditions and the regions of good and bad curvature.[16] However, as mentioned previously, the fusion research establishment has developed numerous methods to improve confinement and limit flute instabilities in magnetic mirrors with alternate magnetic field configurations to reduce bad curvature or the introduction of additional plasma in regions of good curvature. Applying these methods to GDMs would increase the complexity of the magnetic field or would reduce the specific impulse, but should not fundamentally alter or limit the system.

On the macro-scale, physics models predict that charge separation will definitely occur in GDMs. The smaller mass of the electrons compared with plasma ions allow them to escape through the magnetic mirrors faster. As more electrons than ions continue to escape, a positive electrostatic potential will grow inside the GDM's contained plasma. This net positive charge will accelerate the escape of ions and will slow the loss of electrons until an equilibrium is achieved. In a third paper on GDMs, Kammash and Galbraith explored the impact of an electrostatic potential on GDM designs.[21] First, the ions are accelerated by the potential, improving performance of the GDM rocket. However, since the ions are escaping faster, their confinement time decreases. To compensate, the GDM must be longer, thereby increasing the minimum allowable GDM design length and mass. Nonetheless, Kammash and Galbraith found that the performance improvement outweighs the increased mass re-

quirements. Systems were roughly 5-10% faster than equivalent designs that did not account for an electrostatic potential, although larger in size. Of note, the magnetic field requirements were also reduced.

Given the largely speculative nature of GDM system designs, an improvement of less than 10% is not significant in comparison to the increased complexity when moving from MHD equations to a multi-species electro-magnetic hydrodynamic (EMHD) model. In future work, an intermediate step to avoid moving to a full EMHD model may be to impose an external force or electrostatic 'pressure' gradient along the axis of the GDM to simulate the effect. However, the increased electrostatic 'pressure' would not be expected to alter the plasma flow significantly.

CHAPTER III

PARAMETRIC STUDIES OF ADVANCED FUSION FUEL GASDYNAMIC MIRROR PROPULSION SYSTEMS

3.1 Introduction

Traditional fusion research efforts have discarded magnetic mirrors as a viable option due to the plasma losses from the open configuration. Fortunately, a primary design criterion of a plasma propulsion system is significant plasma "loss" that results in thrust. Taking advantage of this, Kammash et al. designed a gas dynamic mirror fusion propulsion system.[22, 23, 21] While potentially feasible, the resulting GDM configurations had masses of 400-1000 metric tons (or 1 to 2.5 times the mass of International Space Station for comparison) and are unlikely to be launched into space in the near future. Up to 75% of the GDM mass budget is devoted to thermal converters and radiators to eliminate waste heat primarily from neutrons produced by the fusion of the $deuterium - tritium$ $(D - T)$ fuel. A reduction in neutron production would significantly decrease the GDM mass requirements. Additionally, high energy neutrons require additional shielding to protect system components. Finally, tritium is a radioactive fuel which creates safety concerns during launch into orbit or possible re-entry into the Earth's atmosphere. This chapter focuses on

Fuel	Products	Total Energy [MeV]	Charged Particle Energy [MeV]	Optimal Ignition Temperature [keV]
$D-T$	$n+^4He$	17.6	3.5	10.5
$D-D$	$p+T$	4.0	4.0	15
	$n+^3He$	3.3	.8	15
$D-^3He$	$p+^4He$	18.3	18.3	60
$^3He-^3He$	$2p+^4He$	12.9	12.9	1000
$p-^{11}B$	3^4He	8.7	8.7	150

Table 3.1: Table of fusion fuels with relevant parameters.

addressing these issues with two possibilities, advanced fusion fuels and/or assisted reactor systems ($Q < 1$).

Again, traditional fusion research has studied advanced fusion fuels such as $D-^3He$, $^3He-^3He$, and $p-^{11}B$ which all generate lower levels of neutron production or none at all. The non-dimensional variable β is the ratio of the plasma pressure over the magnetic pressure, $\beta = nkT/(B^2/2\mu)$. β of 1 is required for plasma containment, and βs that approach one are considered high. Advanced fusion fuels have generally been regarded as unsuitable for low β reactors such as the popular tokamak configuration and uneconomical for power production due to radiation power losses and limited Q-values.[29, 25, 19, 5, 32] However, these fuels could be ideal for a high-β GDM propulsion system. While Q only needs to exceed breakeven and radiation can be used for thrust enhancement[23], the aneutronic nature of the fuels could reduce the weight of a GDM propulsion system. Such a revolutionary system, not limited by the traditional assumptions of the fusion research establishment, would open the solar system to exploration and development.

Using advanced fusion fuels with no or minimal neutron production would reduce the waste heat and therefore the mass of the thermal converters and radiators. Table 3.1 lists various fusion fuels and their corresponding parameters. The aneutronic

$^3He{-}^3He$ and $p{-}^{11}B$ reactions avoid neutron energy loss, but require much larger ignition temperatures. The compromise reaction, $D{-}^3He$, has been studied and offers lower relative neutron power levels, but the resulting configuration is significantly more massive than the original $D-T$ concept. Looking at completely aneutronic fuels, $p{-}^{11}B$ is the most promising for further study with an ignition temperature more than 6 times lower than $^3He{-}^3He$.

In all Kammash's previous work, he assumed a $Q = 1$ or $Q = 1.22$ to achieve ignition and steady state operation. While ignition is a natural goal, there is no reason that Q must exceed 1. If the system does not exceed a critical value, Q_c, then an external power supply can used to supplement the injection energy and maintain a steady state of operation. While perhaps not ideal, such a system has the potential to reduce the total mass and size of a GDM, making it easier to launch into low earth orbit, and may provide a development path from simple plasma rockets to fully ignited fusion GDM systems.

3.2 Analytical GDM Model

Presented here is the model developed by Kammash. [22, 23] The equations for mass and energy conservation for the system on a per unit volume basis are

$$S - \frac{n_1 + n_2}{\tau} - 2n_1 n_2 \langle \sigma v \rangle = 0, \tag{3.1}$$

which is the mass source, S, less particles that escape through the mirrors, $\frac{n_1+n_2}{\tau}$, and the particles lost to each fusion reaction, $2n_1n_2\langle\sigma v\rangle$, and

$$SE_{in} + n_1 n_2 \langle \sigma v \rangle E_0 - \frac{(n_1 + n_2)E_L}{\tau} - P_b - P_s = 0, \tag{3.2}$$

which is injected energy, SE_{in}, and fusion energy from charged particle products, $n_1n_2\langle\sigma v\rangle E_0$, less the energy losses through the mirrors, $\frac{(n_1+n_2)E_L}{\tau}$, and from bremsstrahlung

and synchrotron radiation losses, P_b and P_s . Substituting the first into the second to eliminate S and solving for τ, we get

$$\tau = \frac{(n_1 + n_2)(E_{in} + E_L)}{P_b + P_s - 2n_1 n_2 \langle \sigma v \rangle E_{in} - n_1 n_2 \langle \sigma v \rangle E_0}. \tag{3.3}$$

The confinement time, τ, is really a proxy for the length of the GDM, as the longer the device, the longer it takes for particles to escape.

$$L = \frac{\tau v_{th}}{R} \tag{3.4}$$

and

$$v_{th} = \sqrt{\frac{\pi m}{8T}} \tag{3.5}$$

$E_L = 2T$ and $\langle \sigma v \rangle$ are functions of temperature, while P_b and P_s are functions of density and temperature. E_0, the fusion energy found in the resulting charged particles, is a constant for the particular fuel combination. Given the particle density of both fuel species and a plasma temperature, the only unknown is the injection energy, E_{in}.

Rather than guess at E_{in}, we can solve for it using the definition of Q.

$$Q = \frac{P_f}{P_i} = \frac{n_1 n_2 \langle \sigma v \rangle E_f}{E_{in}(\frac{n_1 + n_2}{\tau})} \tag{3.6}$$

Substitute this into Equation 3.3 and eliminate τ, then solve the resulting quadratic for E_{in}.

$$E_{in}(Q) = -\frac{\xi}{4} + \sqrt{(\frac{\xi}{4})^2 + \frac{E_f E_L}{2Q}} \tag{3.7}$$

$$\xi = E_0 + \frac{E_f}{Q} - \frac{P_b + P_s}{n_1 n_2 \langle \sigma v \rangle} \tag{3.8}$$

Early on, Kammash simply assumed a Q of 1. A power flow analysis with assumed efficiencies for the various components of the system including injection, direct MHD

E_{in}	injection energy
T	plasma temperature
n_i	particle densities of each fuel component
R	mirror ratio
$\langle\sigma v\rangle$	velocity averaged fusion cross section
E_0	fusion energy in charged particles
E_f	total fusion energy per reaction
Q	reactor gain factor
P_b	bremsstrahlung radiated power $P_b(T, n)$
P_s	synchrotron radiated power $P_s(T, n)$

Table 3.2: Variable definitions used by Kammash.

converter, and thermal power converter efficiencies produces a critical $Q = 1.22$.[23] The equation for this power flow analysis can be found in Section 3.4.

Given fuel densities and the plasma temperature, we solve for E_{in} using Equation 3.7. Then with Equation 3.3 and an assumed mirror ratio and β giving us the effective mirror ratio, $R = R_0/\sqrt{1-\beta}$, we get

$$L = \frac{v_{th}}{R}\frac{(n_1+n_2)(E_{in}+E_L)}{P_b+P_s-2n_1n_2\langle\sigma v\rangle E_{in}-n_1n_2\langle\sigma v\rangle E_0}. \tag{3.9}$$

Based on various system efficiencies, we get a Q critical of 1.22. Having assumed a plasma temperature, a plasma density, fuel type and ratios, magnetic to plasma pressure ratio, and mirror ratio, we can solve for an injection energy and then the system length. Then it is relatively straightforward to calculate the volume of the system and the total neutron, radiation, and charged particle powers of the system. With the total powers, we can estimate the mass of the system and then compute the trip time for a particular mission. All that follows in this chapter is new work based on this model and extending it.

3.3 Proton-^{11}Boron Gasdynamic Mirror Propulsion Systems

The $p-^{11}B$ fuel combination appears very attractive given its largely aneutronic nature, availability, and reasonable ignition temperature. However, the primary challenge of advanced fusion fuels is the higher plasma temperatures. At these temperatures, bremsstrahlung and synchrotron radiation losses become so significant as to limit the Q factor or even the ability to reach ignition. Previously developed parametric models[22, 23] with $p-^{11}B$ parameters were modified to take into account that T_e is not equal to T_i. Here Dawson[11] is used to find T_e, and bremsstrahlung power is calculated as done in Nevins[31]. The important characteristics of this model include a high density (Maxwellian plasma) in a large aspect ratio GDM propulsion system with homogeneous properties throughout, a Q of slightly greater than 1 to account for efficiency losses, and a mission trajectory which assumes a direct line from origin to destination with constant acceleration or deceleration during transit.

The charts in Figure 3.1 indicate radiation powers as multiples of the fusion power generated. Equations 4.57, 4.63, and 4.66 define these powers, and any additional assumed system properties can be found in Table 3.3. These charts are generally representative of this fuel choice and β as the densities in P_b and P_f cancel and P_s/P_f is proportional to β. GDM designs assume shielding with high radiative reflectivity to reduce the thermal load on the spacecraft and return the radiative energy back to the plasma column. Materials that are nearly 100% reflective have been demonstrated for synchrotron radiation; most of the losses represent that fraction of the plasma column's surface that cannot be shielded in a practical manner, such as injection points or the ends of the plasma column. With a non-dimensional reflectivity of .9, the synchrotron power is too much. Increasing the reflectivity to .99, a potential

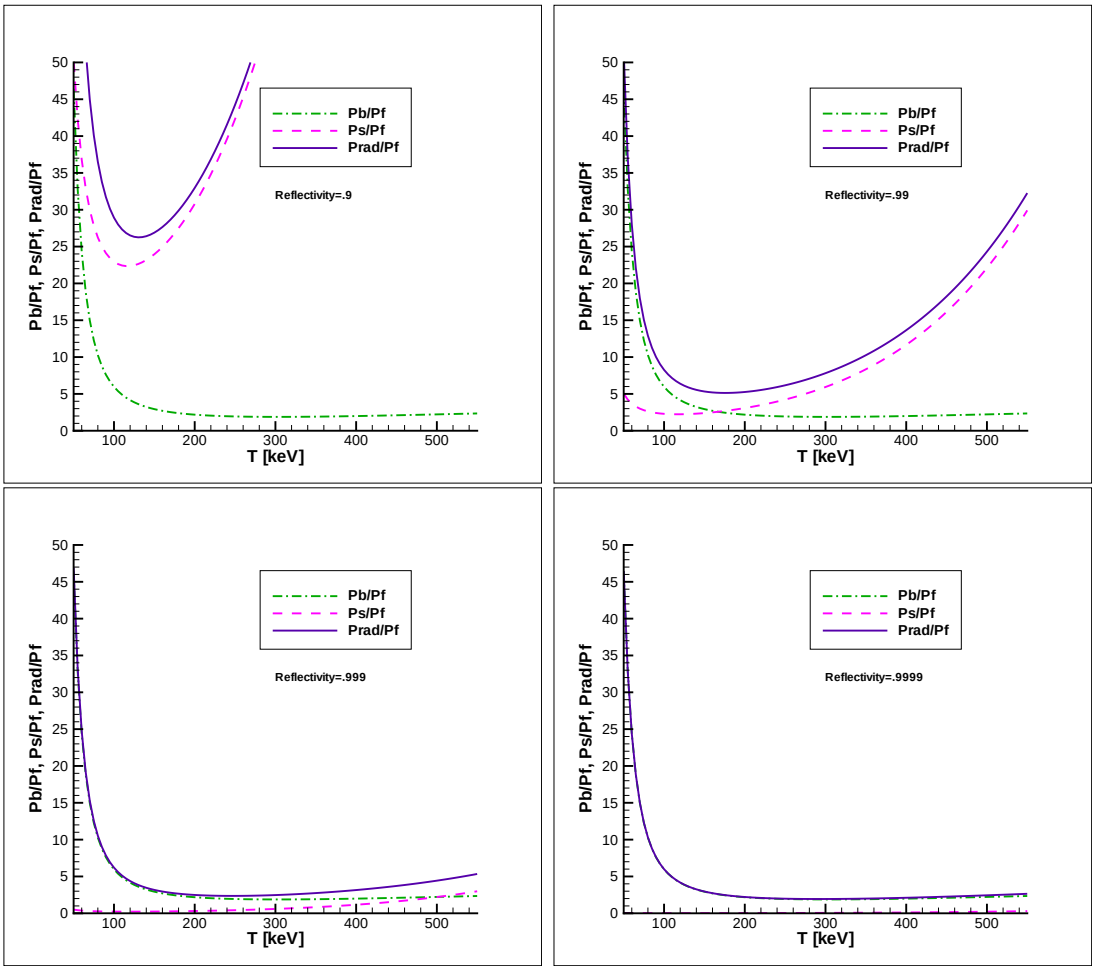

Figure 3.1: Power ratios as a function of temperature for different reflectivities (.9, .99, .999, .9999). P_b is bremsstrahlung radiation power, P_s is synchrotron radiation power, and P_{rad} is $P_b + P_s$.

$p-^{11}B$ system would work at around 160 KeV giving an optimal balance between bremsstrahlung and synchrotron losses. However, assuming P_i is derived from a somewhat optimistic 50% efficient recovery from P_{rad}, a $Q > 1$ is only possible when P_{rad}/P_f ratio is below 2. In the case of .9999 reflectivity, synchrotron radiation becomes unimportant. Bremsstrahlung radiation is heavily concentrated in the x-ray band and cannot be easily reflected. In the remaining cases, T=300 keV and R=.9999 were assumed, as the best case scenario possible. Even then, radiation losses are a multiple of the fusion power (roughly 1.8) indicating the GDM may

function only in a driven mode, because ignition may not be feasible. Remember that radiation losses are recaptured as heat, and a significant fraction of the energy is converted back into electrical energy to drive the GDM system. Fortunately, high Q is not necessary for GDM operation; only slightly greater than 1 is needed.

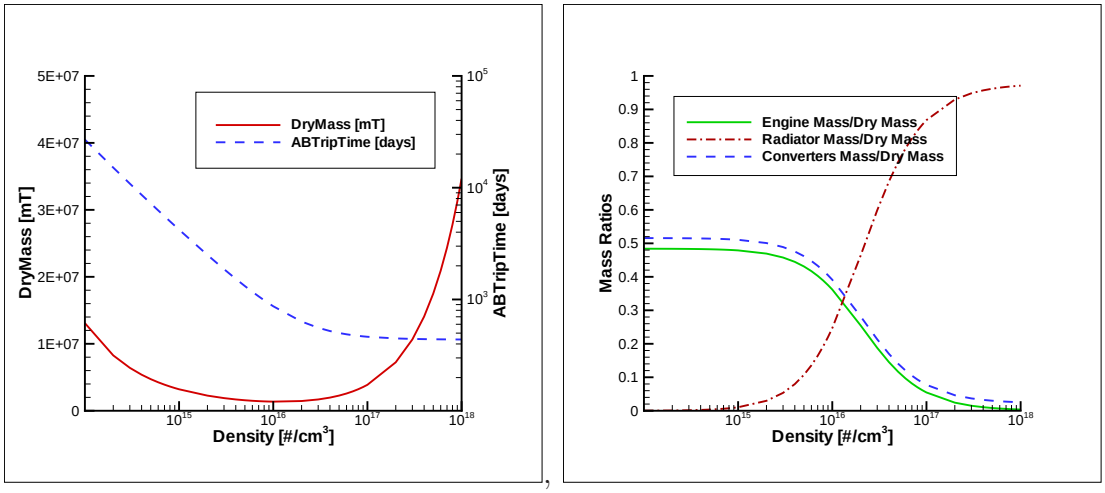

Figure 3.2: System mass, trip time, and component mass fractions as a function of plasma density.

Figure 3.2 explores the effects of plasma density on our GDM propulsion system. Greater density increases total fusion power and thrust, but it also increases the radiation load with corresponding thermal converters and radiators. The first chart indicates an optimum density of 2.0×10^{16} particles per cubic centimeter leads to the minimum dry mass of the system as well as approaching the best trip time. The second chart explains this by showing how the thermal radiator mass dominates the system above the optimum density.

The fuel ratio, $\frac{n_B}{n_p}$, also has a significant effect on the GDM system. The primary driver of this is the much greater charge of boron atoms (Z=5). ^{11}B contributes, on a per atom basis, much more to bremsstrahlung radiation than a single hydrogen proton. Additionally, it also adds to the electron density increasing the synchrotron radiation. Of course, too little ^{11}B reduces the fusion power. Figure 3.3 clearly

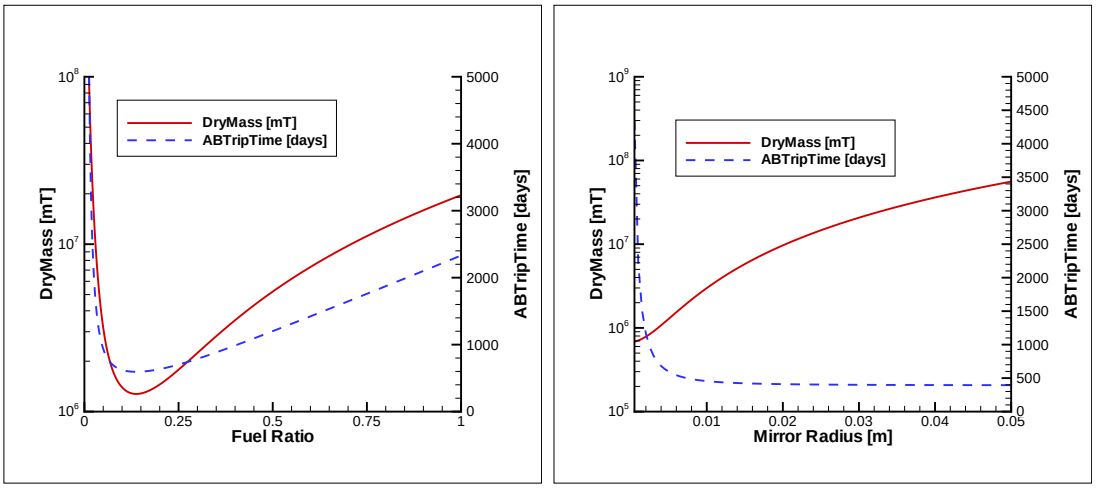

Figure 3.3: Fuel fraction and mirror radius impact on system mass and trip time.

indicates that a fuel ratio of .15 produces the optimal dry mass and trip time.

With the various system parameters optimized, the actual size of the system is a direct function of its radius, which is specified through the mirror radius. Dry mass and trip time are also plotted against the mirror radius in Figure 3.3. While shrinking the radius continues to reduce the total mass, the diminishing thrust increases travel time. Choosing a mirror radius of .005 meters gives close to optimal trip time with minimum mass.

As such, the best system possible requiring $Q > 1$ is detailed in Table 3.3. Unfortunately, such a system is 24 kilometers long, weighing over a million metric tons, and takes a year and half to reach Mars. Fundamentally, the large bremsstrahlung losses increase system size beyond a practical limit to achieve a $Q > 1$ design.

3.4 Nuclear Electric Assisted Approach

If the $Q > 1$ requirement is relaxed and supplemental power is generated with a nuclear electric fission reactor, the size of the system can be reduced. This is done

—Input Parameters—	
Reaction Type	$p-^{11}B$
Plasma Density	2×10^{16} $\#/cm^3$
Hydrogen Density	1.7×10^{16} $\#/cm^3$
Boron-11 Density	2.61×10^{15} $\#/cm^3$
Electron Density	3.04×10^{16} $\#/cm^3$
Plasma Temperature	300 keV
Beta (vacuum)	0.95
Plasma Mirror Ratio	100
Plasma Mirror Radius	0.005 m
Halo Thickness	0.1 m
Shield Magnet Gap	0.1 m
Shield Thickness	0.19 m
Injector Eff.	1
Thermal Conv. Eff.	0.45
Direct Conv. Eff.	0.9
Magnet Current Den.	2.5×10^8 MA/m^2
Destination Mars	7.8e+10 m
—Calculated Parameters—	
Vacuum magnetic field, Bp0	80.07 Tesla
Gain Factor, Q	1.22222
Plasma Length, L	23635 m
Injection Energy, Ein	1464.34 keV
Loss Energy, EL	600 keV
Thrust	150985 N
Thrust Power	4.44×10^5 MW
Injection Power	2.17×10^6 MW
Fusion Power	2.65×10^6 MW
Bremsstrahlung Power	4.67×10^6 MW
Synchrotron Power	1.67×10^5 MW
Total Dry Mass	1.28×10^6 mT
Engine Mass Fraction	0.29
Converters Mass Fraction	0.30
Radiator Mass Fraction	0.41
I_{sp}	693791 s
Round Trip Time	3.27 years
Trip Time AB	1.63 years
Fusion Power	1.43×10^{10} $watts/m^3$
Bremsstrahlung Power	2.51×10^{10} $watts/m^3$
Pb/Pf	1.76
Synchrotron Power	8.97×10^8 $watts/m^3$
Ps/Pf	0.06

Table 3.3: Optimized $Q > 1$ $p-^{11}B$ GDM.

by replacing the equation for the critical Q in the model[23] with the following

$$Q_c = \frac{1 - F\eta_i\eta_D}{F\eta_i\eta_D + \eta_i(\frac{P_{ne}-P_H}{P_f}) + \eta_i(\eta_t - F\eta_D)\frac{P_n+P_r}{P_f}}, \tag{3.10}$$

where η are the efficiencies of the injector, the direct converter, and the thermal converter, P are the total powers of fusion energy, nuclear electric, heating, neutron losses and radiation losses, and F is the fraction of charged particles entering the direct converter, while $F - 1$ would be the fraction used for thrust. In the original model, P_{ne} and P_H are taken as zero, F is $\frac{1}{2}$, and η_i, η_D, and η_t are 1.0, .9, and .45 respectively; this gives Q_c equal to 1.22. By introducing supplemental power as a fraction of the fusion power and adding the mass of an advanced nuclear electric space power system based on Smith[39], the reduced system parameters can be found in Figure 3.4. For a $p-^{11}B$ T=300 keV system, the effects of supplemental power are moderate overall. However, with $Q < 1$ being acceptable, the temperature can be reduced to a more reasonable 160 keV. Also shown in Figure 3.4, the impact from nuclear electric assist is significant on the system size and mass. Nonetheless, the system remains unsuitably large.

Applying the same nuclear electric power assist to the original $D-T$ system, the length of the system is reduced and as the required Q is lowered the necessary radiator mass decreases. However, the specific power of the nuclear electric generator is much less than the specific power of the $D - T$ system. The additional mass required for power generation more than offsets any savings on radiator mass resulting in a net increase in the dry mass and trip time. Parameters for a nuclear assisted $D - T$ system can be found in Figure 3.5.

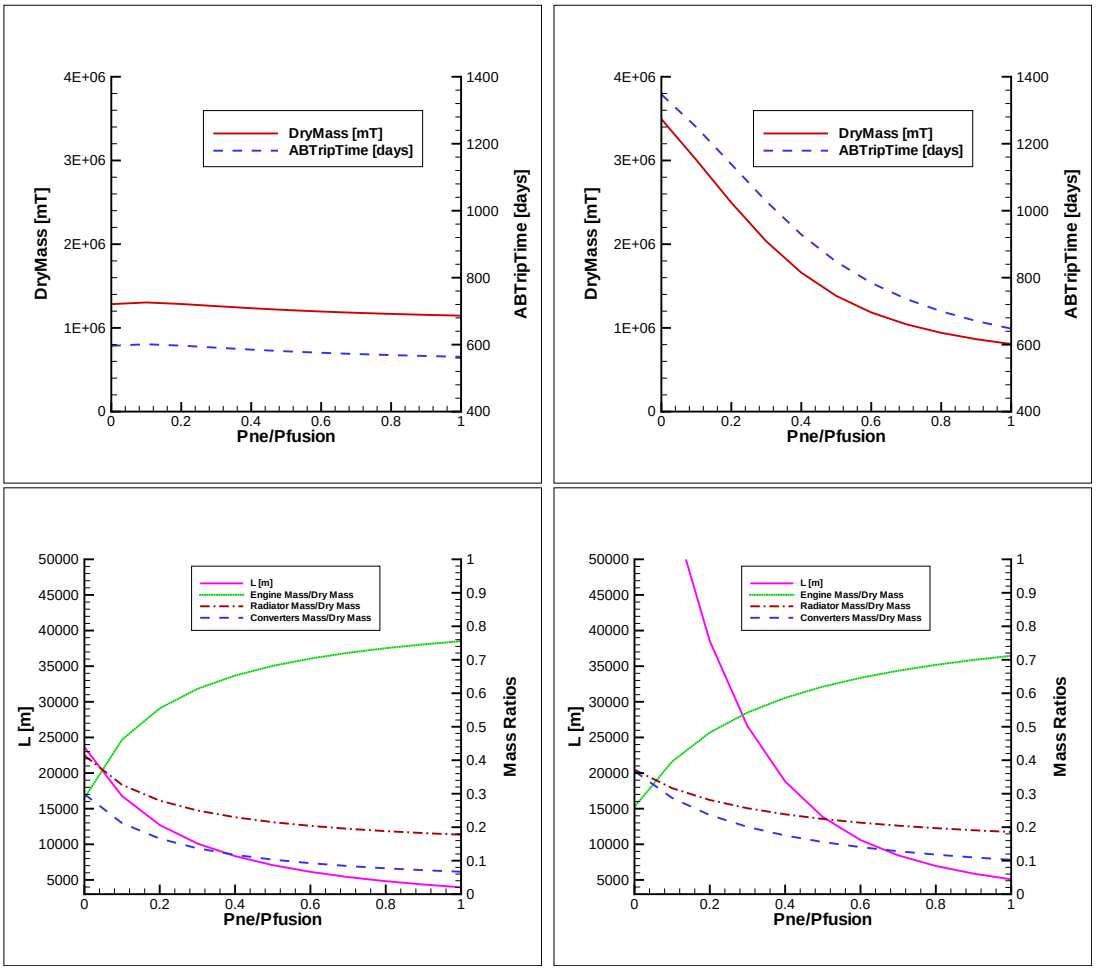

Figure 3.4: System parameters based on the nuclear assist fraction. T=300 keV on the left and T=160 keV on the right.

3.5 Conclusions

The original GDM designs were quite massive at hundreds of metric tons, and 75% of their mass were radiators to shed excess heat from energetic neutrons not contained by the magnetic confinement. An often-mentioned solution is to use aneutronic advanced fusion fuels such as $p-^{11}B$. Using the Kammash GDM model, the radiative losses from bremsstrahlung radiation in $p-^{11}B$ GDM system are too great to develop a practical system with a homogeneous plasma. Even relaxing the expectation of $Q > 1$ in a $p-^{11}B$ system and assisting with nuclear electric power, the system size

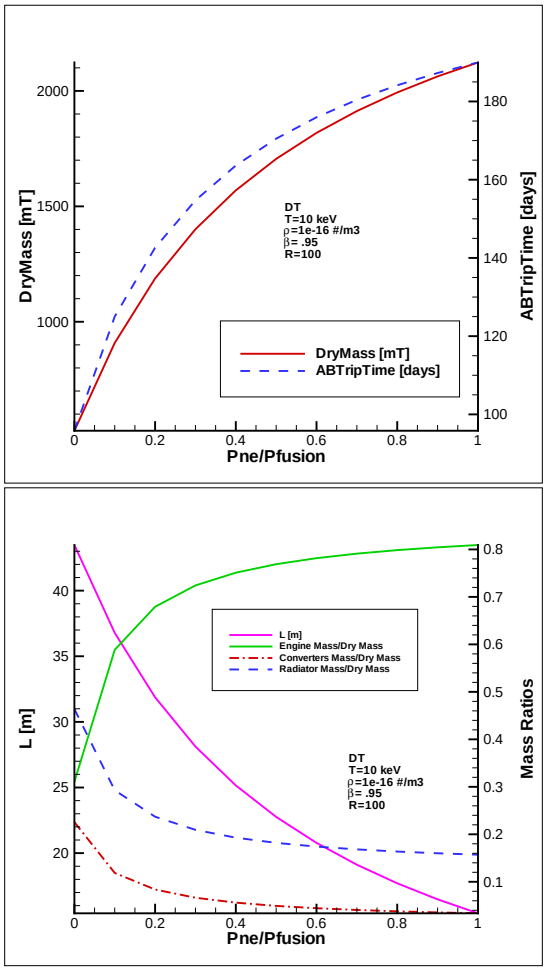

Figure 3.5: System parameters based on the nuclear assist fraction.

and mass remain too large.

Nonetheless, the aneutronic nature, availability, and non-radioactive nature of advanced fusion fuels remain attractive. If such a system is to be developed, it will require a non-uniform plasma at lower temperatures and a computational MHD model to evaluate it.

The $D-T$ GDM system, while feasible at around 500 metric tons and a 2 month one-way trip time to Mars, is still quite large. A future research goal is to explore the development path from plasma rockets to GDMs by exploring potential hybrid systems. For the simple homogeneous plasma Kammash model, a nuclear-assisted

$D-T$ GDM, while shorter in length, has greater mass and increased trip times compared to the original system design. Nonetheless, the decreased performance is almost linear as Q is decreased, which suggests that hybrid systems are possible, if less than optimal. Again, a non-uniform plasma where fusion reactions do not depend on random collisions seems to be better suited to finding a development path from plasma rockets to fusion propulsion systems.

CHAPTER IV

COMPUTATIONAL MAGNETOHYDRODYNAMIC MODELING TOOL

At the outset of this work, the goal was to model advanced electric space propulsion systems with higher density plasmas using the ideal MHD equations. Available tools were either ideal MHD codes without complex geometry capability or CFD codes capable of modeling complex geometries without MHD solvers. It was decided that the easiest approach was to add MHD solvers to a 3-D complex geometry code rather than add complex geometry abilities to a MHD code.

The foundation of this computational modeling effort was a CFD code developed by Eric Charlton and named OSCAR, Octree Solution to Conservation-laws over Arbitrary Regions.[9] OSCAR was an Euler, finite-volume modeling tool with a 3-dimensional, adaptive Cartesian grid generator for aircraft aerodynamics applications. OSCAR was a serial C++ code, developed primarily as research platform for testing parametric geometry generation and adaptive cartesian algorithms.

This chapter will describe OSCAR and how the author extended its capabilities including adaptive grid refinement based on the magnetic field, algorithms for generating background magnetic field for containing the plasmas of interest, MHD

boundary conditions, and the MHD explicit and implicit solvers. For some original aspects of OSCAR, only a brief description is given here and more detailed explanations can be found in Charlton's original work.[9]

4.1 Non-dimensionalization

Unless noted otherwise, the following equations are specified in non-dimensional terms. Four independent dimensional terms are required to define the variables involved in the computer simulation of a GDM under assumptions of ideal magnetohydrodynamics. The terms used in this work include a characteristic length (L_∞), density (ρ_∞), speed (a_∞), and magnetic field strength (B_∞). L_∞ is typically chosen to be the approximate radius of the plasma at its narrowest point, the GDM's magnetic throat. The terms, ρ_∞ and a_∞, are the anticipated density and speed of sound at the center of the containment system. The magnetic dimensional term, B_∞, is the anticipated magnetic field at the center of the GDM divided by $\sqrt{\mu_0}$, thereby removing μ_0 from the governing equations.

Dimensional conversion factors for other variables can be derived from the four original independent dimensional terms including values for pressure, temperature (both K and eV), energy, and power. Pressure units are $\mathrm{N/m^2}$ or $\mathrm{kg/(s^2\ m)}$ resulting in a dimensional factor, $p_\infty = \rho_\infty a_\infty^2$. Temperature does not generally appear in non-dimensional form, but can be derived from non-dimensional density, pressure, and the ideal equation of state. In dimensional units

$$p = \sum_j n_j k T_j \tag{4.1}$$

and assuming $T_e = T_i$ with z and n_i being the average ion charge and the ion density

$$p = (z+1) n_i k T. \tag{4.2}$$

With m being the average mass of a mole of ions in kg/mole and the universal gas constant $R = kN_a$, then

$$T[K] = \frac{m}{z+1}\frac{a_\infty}{R}\frac{p}{\rho} = .12027\frac{m}{z+1}a_\infty\frac{p}{\rho} \tag{4.3}$$

or

$$T[eV] = \frac{k}{e}\frac{1}{R}\frac{m}{z+1}a_\infty\frac{p}{\rho} = 1.036427^{-5}\frac{m}{z+1}a_\infty\frac{p}{\rho} \tag{4.4}$$

4.2 Grid Generation

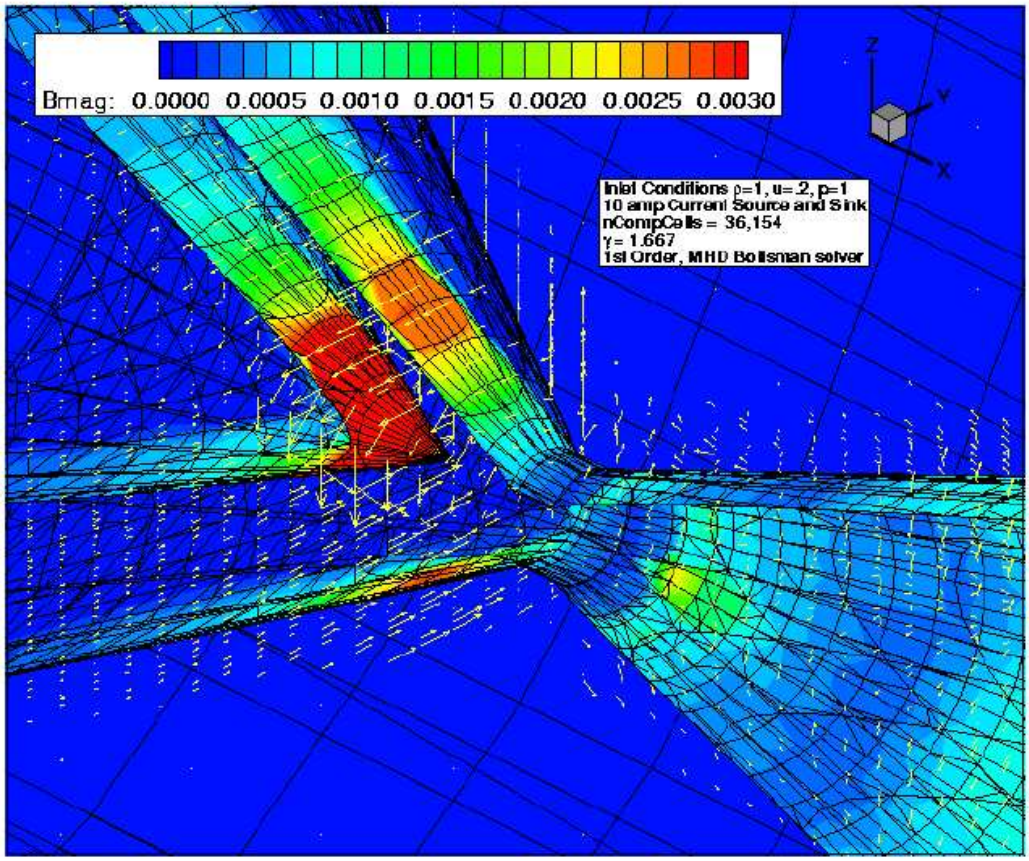

Figure 4.1: Sample Cartesian grid of an arcjet propulsion system.

4.2.1 3D Cartesian Adaptive Grids

OSCAR generates a Cartesian octree grid. The root cell, representing the whole domain, is a cube which is subdivided into eight children cells which in turn are also subdivided in eight children cells and so on. Each leaf cell is a cubic cut or uncut cell. An uncut Cartesian cell simply has six interfaces with neighboring cells.

All geometries in OSCAR are represented by polyhedrons made from a collection of polygons. Each polygon is a collection of points in a plane; the rotation order of the points determines a normal vector that points into the flow region of the simulation based on the right hand rule. Any cell that intersects a geometry, typically a physical object in the flow field, is considered a cut cell. Polygons that intersect a cell are recut to fit within the cell and become a boundary interface. Boundary conditions associated with the geometry in question are assigned to the boundary interface. There are as many boundary interfaces in a cut cell as necessary to represent the geometry contained in that cell. A new volumetric centroid is determined for the cut cell. Split cells, where the geometry divides a cell into separate regions, are not allowed and eliminated with additional grid refinement.

The octree grid described above has the ability to resolve any arbitrary geometry defined with polygons. Refinement does not have to be uniform, allowing refinement to occur around complex geometric surfaces or in flow regions of interest. In OSCAR, the grids are adaptive, automatically refining where needed. The initial adaptive criterion is based on the curvature of any geometries present. As the flow solution develops additional refinements can occur using the following criteria: curl of the velocity to resolve vorticity, divergence of the velocity to sharpen gradients and shocks, gradients of entropy values, curl of the magnetic field to find current flows, and the divergence of the magnetic field to reduce discretization errors of the

magnetic fields. The last two criteria were added by the author to the original scheme for modeling plasma propulsion systems.

$$|\nabla \times \mathbf{V}|, |\nabla \mathbf{V}|, \left|\nabla p - a^2 \nabla \rho\right|, |\nabla \times \mathbf{B}|, |\nabla \cdot \mathbf{B}| \tag{4.5}$$

Cell values for each of the criteria listed above and a standard deviation, σ, for each criteria's distribution are generated. Any cell with a value greater than $n\sigma$, where n is some constant multiple input by the user, is refined. In addition to solution-adaptive refinement, the operator can define regions of the flow simulation where additional refinement should occur or not be allowed. Finally, no cell may be bordered by cells more than one level of refinement below, so the grid is smoothed with additional refinement where necessary. OSCAR is also capable of adaptive coarsening to remove unnecessary resolution.

4.2.2 Stretch Mapping

Given the extremely large aspect ratios of GDM systems, where the plasma might be 100s of meter long with a radius of a few centimeters, the cubic only nature of OSCAR's grid cells was limiting. In order to get adequate radial resolution down to centimeters, the resulting grid has excessive axial resolution. Not only are the total number of grid cells much larger than necessary, but the corresponding cell volumes and allowable time steps are smaller as well.

Rather than rewrite OSCAR to handle rectangular cells, a stretch mapping was introduced into the code. Given a scaling stretch vector, $\mathbf{S} = (\mathbf{S_x}, \mathbf{S_y}, \mathbf{S_z})$, all inputted geometries and locations are divided by the scaling factors except the dimensions of the root cell which must remain cubic. OSCAR proceeds to grid the case using cubic cells, but the cell volumes and the area of every interface are scaled up by the stretch vector and used for updating the state.

4.3 Magnetohydrodynamic Solvers

4.3.1 MHD State Vectors

Each cell stores physical properties as a standard finite-volume formulated average state vector, **W**. The original OSCAR code only supported the fluid state with the Euler equations; it was extended to plasmas with the ideal MHD equations by the author. For ideal MHD, the primitive state vector is

$$\mathbf{W} = (\rho, u, v, w, B_x, B_y, B_z, p)^T, \tag{4.6}$$

and with $\rho E = \frac{p}{\gamma - 1} + \frac{1}{2}\rho q^2$ and $q^2 = u^2 + v^2 + w^2$ the conservative vector would be

$$\mathbf{U} = (\rho, \rho u, \rho v, \rho w, B_x, B_y, B_z, E)^T. \tag{4.7}$$

Although the mathematical formulation of the solvers in OSCAR are all done with conservative vectors, the state vectors are stored and limited in primitive form.

4.3.2 Gradients and Limiting

To achieve 2nd order accuracy, gradients for the primitive state value are determined using least squares reconstruction. When determining the state values at an interface between cells, the state values are extrapolated from the cell centroid and the average state to the interface centroid using the gradients. To preserve monotonicity, a limiter is applied to each individual property.

A classic min-mod limiter of the form

$$\mathbf{\Phi_i} = min \left\{ \begin{array}{c} 1 \\ min(\frac{|W_i^{cell} - max(W_i^{neighbors})|}{|W_i^{cell} - max(W_i^{interfaces})|} \\ min(\frac{|W_i^{cell} - min(W_i^{neighbors})|}{|W_i^{cell} - min(W_i^{interfaces})|} \end{array} \right\} \tag{4.8}$$

is generally used, where W_i refers to each individual scalar property of the primitive state vector. Usually each property is limited separately, but the greater constraint of $\Phi = min(\Phi_i)$ is also available.

Another limiter by Venkatakrishnan[42] was also implemented by the author to avoid limit cycling and the need for freezing the limiter.

$$\mathbf{\Phi_i} = min \left\{ \begin{array}{c} 1 \\ \phi(|W_i^{cell} - max(W_i^{neighbors})|, |W_i^{cell} - max(W_i^{interfaces})|) \\ \phi(|W_i^{cell} - min(W_i^{neighbors})|, |W_i^{cell} - min(W_i^{interfaces})|) \end{array} \right\} \tag{4.9}$$

and

$$\phi = \frac{1}{\Delta_-} \left(\frac{\left(\Delta_+^2 + \epsilon^2\right) \Delta_- + 2\Delta_-^2 \Delta_+}{\Delta_+^2 + 2\Delta_-^2 + \Delta_- \Delta_+ + \epsilon^2} \right) \tag{4.10}$$

where $\Delta_- = |W_i^{cell} - max(W_i^{interfaces})|$ or $|W_i^{cell} - min(W_i^{interfaces})|$ and $\Delta_+ = |W_i^{cell} - max(W_i^{neighbors})|$ or $|W_i^{cell} - min(W_i^{neighbors})|$. The ϵ factor is an attempt to improve on accuracy that was lost with limiting. ϵ^2 is generally taken to be $(K\Delta x)^3$ where K is a constant. If K is taken to be zero, then limiting is enforced everywhere, reducing the accuracy and slowing convergence. When K is set anywhere from .1 to 5, it restricts limiting first in regions of near-constant flow and then in regions of greater and greater variability by drowning out the $\Delta_\pm$ values in the limiter. When K is large enough, there is effectively no limiting. While convergence improves, unphysical oscillations can become evident in the solutions and even cause the solution to become unstable.

4.3.3 Governing Equations

The ideal MHD equations assume inviscid, continuum flow with conductance occurring on a much smaller time scale as to appear infinite at non-relativistic velocities. The eight resulting equations including conservation of mass, momentum, magnetic field, and energy in typical dimensional form are:

$$\frac{\partial \rho}{\partial t} + \nabla \cdot (\rho \mathbf{u}) = 0, \tag{4.11}$$

$$\frac{\partial (\rho \mathbf{u})}{\partial t} + \nabla \cdot \left(\rho \mathbf{u}\mathbf{u} + \left(p + \frac{\mathbf{B} \cdot \mathbf{B}}{2\mu_0} \right) \mathbf{I} - \frac{\mathbf{B}\mathbf{B}}{\mu_0} \right) = 0, \tag{4.12}$$

$$\frac{\partial \mathbf{B}}{\partial t} + \nabla \cdot (\mathbf{u}\mathbf{B} - \mathbf{B}\mathbf{u}) = 0, \text{and} \tag{4.13}$$

$$\frac{\partial E}{\partial t} + \nabla \cdot \left[\left(E + p + \frac{\mathbf{B} \cdot \mathbf{B}}{2\mu_0} \right) \mathbf{u} - \frac{1}{\mu_0} (\mathbf{u} \cdot \mathbf{B}) \mathbf{B} \right] = 0. \tag{4.14}$$

The non-dimensional form of the MHD equations used in this work are solved in their symmetrizable form and are shown below.[18, 35]

$$\frac{\partial \rho}{\partial t} + \nabla \cdot (\rho \mathbf{u}) = 0 \tag{4.15}$$

$$\frac{\partial (\rho \mathbf{u})}{\partial t} + \nabla \cdot \left(\rho \mathbf{u}\mathbf{u} + \left(p + \frac{\mathbf{B} \cdot \mathbf{B}}{2} \right) \mathbf{I} - \mathbf{B}\mathbf{B} \right) = -\mathbf{B} \nabla \cdot \mathbf{B} \tag{4.16}$$

$$\frac{\partial \mathbf{B}}{\partial t} + \nabla \cdot (\mathbf{u}\mathbf{B} - \mathbf{B}\mathbf{u}) = -\mathbf{u} \nabla \cdot \mathbf{B} \tag{4.17}$$

$$\frac{\partial E}{\partial t} + \nabla \cdot \left[\left(E + p + \frac{\mathbf{B} \cdot \mathbf{B}}{2} \right) \mathbf{u} - (\mathbf{u} \cdot \mathbf{B}) \mathbf{B} \right] = - (\mathbf{u} \cdot \mathbf{B}) \nabla \cdot \mathbf{B} \, . \tag{4.18}$$

Using the symmetrizable form means the $\nabla \cdot \mathbf{B}$ in the source terms is never assumed to be zero. Rather, it is retained and can be considered a corrective term to compensate for numerically introduced, but unphysical, $\nabla \cdot \mathbf{B}$.

$$\mathbf{S}_{\nabla \cdot \mathbf{B}} = -\nabla \cdot \mathbf{B} \begin{pmatrix} 0 \\ \mathbf{B} \\ \mathbf{u} \\ \mathbf{u} \cdot \mathbf{B} \end{pmatrix} \tag{4.19}$$

In addition, there are physical source terms in our simulations to accountant for mass injections, synchrotron and bremsstrahlung radiation, and fusion energy.

$$\mathbf{S}_{physical} = \mathbf{S}_i + \mathbf{S}_b + \mathbf{S}_s + \mathbf{S}_f \tag{4.20}$$

These physical source terms are detailed later in the chapter. The physical and $\nabla \cdot \mathbf{B}$ source terms are logically kept separate, because the physical source terms are calculated for each cell in a volumetric fashion while the $\nabla \cdot \mathbf{B}$ source terms are calculated at each interface with the fluxes and integrated over the surface of each cell. With the flux vector represented as

$$\mathbf{F} = \begin{pmatrix} \rho\mathbf{u} \\ \rho\mathbf{u}\mathbf{u} + \left(p + \frac{\mathbf{B}\cdot\mathbf{B}}{2}\right)\mathbf{I} - \mathbf{B}\mathbf{B} \\ \mathbf{u}\mathbf{B} - \mathbf{B}\mathbf{u} \\ \mathbf{u}\left(E + p + \frac{\mathbf{B}\cdot\mathbf{B}}{2}\right) - (\mathbf{u}\cdot\mathbf{B})\,\mathbf{B} \end{pmatrix}^T . \tag{4.21}$$

We can write the whole system as

$$\frac{\partial \mathbf{U}}{\partial t} + (\nabla \cdot \mathbf{F})^T = \mathbf{S}_{\nabla\cdot\mathbf{B}} + \mathbf{S}_{physical} \tag{4.22}$$

4.3.4 Split Magnetic Field Formulation

Due to the exceedingly large magnetic fields in a GDM system, magnetic terms can dominate the system and small errors in the magnetic field can have profound effects on the wave system modeled by the Roe linearization. Therefore, to increase accuracy, the magnetic field can be separated into two components, a perturbation and the background embedded field.[34]

$$\begin{aligned} \mathbf{B} &= \mathbf{B}_0 + \mathbf{B}_1 \qquad \mathbf{U}_1 = (\rho, \rho\mathbf{u}, \mathbf{B}_1, E_1)^T \\ E_1 &= \frac{p}{\gamma - 1} + \rho\frac{\mathbf{u}\cdot\mathbf{u}}{2} + \frac{\mathbf{B}_1\cdot\mathbf{B}_1}{2} \\ \frac{\partial \mathbf{U}_1}{\partial t} &+ (\nabla \cdot \mathbf{F}_1)^T + (\nabla \cdot \mathbf{G})^T = \mathbf{S}_1 \end{aligned} \tag{4.23}$$

$$\mathbf{F}_1 = \begin{pmatrix} \rho\mathbf{u} \\ \rho\mathbf{u}\mathbf{u} + \left(p + \frac{\mathbf{B}_1\cdot\mathbf{B}_1}{2}\right)\mathbf{I} - \mathbf{B}_1\mathbf{B}_1 \\ \mathbf{u}\mathbf{B}_1 - \mathbf{B}_1\mathbf{u} \\ \mathbf{u}\left(E_1 + p + \frac{\mathbf{B}_1\cdot\mathbf{B}_1}{2}\right) - (\mathbf{u}\cdot\mathbf{B}_1)\,\mathbf{B}_1 \end{pmatrix}^T \tag{4.24}$$

$$\mathbf{S}_1 = -\nabla\cdot\mathbf{B}_1 \begin{pmatrix} 0 \\ \mathbf{B} \\ \mathbf{u} \\ \mathbf{u}\cdot\mathbf{B}_1 \end{pmatrix} \tag{4.25}$$

$$\mathbf{G} = \begin{pmatrix} 0 \\ (\mathbf{B}_0\cdot\mathbf{B}_1)\,\mathbf{I} - (\mathbf{B}_0\mathbf{B}_1 + \mathbf{B}_1\mathbf{B}_0) \\ \mathbf{u}\mathbf{B}_0 - \mathbf{B}_0\mathbf{u} \\ (\mathbf{B}_0\cdot\mathbf{B}_1)\,\mathbf{u} - (\mathbf{u}\cdot\mathbf{B}_1)\,\mathbf{B}_0 \end{pmatrix}^T \tag{4.26}$$

In this form, the Roe approximate flux function retains the identical form as before, except it can no longer be dominated by errors in the full magnetic field. No assumptions were made about the relative sizes of $\mathbf{B}_0$ and $\mathbf{B}_1$. The only requirements are that the embedded field satisfy $\frac{\partial\mathbf{B}_0}{\partial t} = 0$, $\nabla\cdot\mathbf{B}_0 = 0$, and $\nabla\times\mathbf{B}_0 = 0$.

The resulting finite volume formulation would be

$$\frac{d\mathbf{U}_i}{dt}V_i + \sum_{faces}\mathbf{F}_1\cdot\hat{\mathbf{n}}dS + \sum_{faces}\mathbf{G}\cdot\hat{\mathbf{n}}dS = -\begin{pmatrix} 0 \\ \mathbf{B} \\ \mathbf{u} \\ \mathbf{u}\cdot\mathbf{B} \end{pmatrix}_i \sum_{faces}\mathbf{B}\cdot\hat{\mathbf{n}}dS \tag{4.27}$$

and the residual term alluded to in the multi-stage update below is

$$\mathbf{R} = -\begin{pmatrix} 0 \\ \mathbf{B} \\ \mathbf{u} \\ \mathbf{u}\cdot\mathbf{B} \end{pmatrix}_i \sum_{faces} \mathbf{B}\cdot\hat{\mathbf{n}}dS - \sum_{faces} \mathbf{F}\cdot\hat{\mathbf{n}}dS - \sum_{faces} \mathbf{G}\cdot\hat{\mathbf{n}}dS\ . \tag{4.28}$$

4.4 Explicit Update

Using one of the approximate Riemann solvers described in the next section, a flux and a maximum wave speed are calculated for every interface. A local time step for each cell is calculated by dividing the cell volume by a sum of maximum wave speeds times the interface area.

$$\Delta t = \frac{V\cdot CFL}{\sum_{ifaces} max(\lambda_i)A_i} \tag{4.29}$$

With CFL=1.0, this gives us a standard CFL limited time step. If solving for a steady state solution, we can use the local time stepping. If running time-accurate, the minimum time step across all cells, or a manually inputted time step, is applied globally.

The fluxes in each cell are summed for the cell's residual, $d\mathbf{U}/dt$. Using each cell's previous conservative state vector, $\mathbf{U}$, the residual, and the time step, the cell state is updated with a 2nd order multi-stage scheme.

$$\mathbf{U}^{(0)} = \mathbf{U}^n \qquad k = 1\ldots m \tag{4.30}$$

$$\mathbf{U}^{(k)} = \mathbf{U}^{(0)} + \frac{\alpha_k \Delta t}{V_i}\mathbf{R}\left(\mathbf{U}^{(k-1)}\right) \tag{4.31}$$

$$\mathbf{U}^{(n+1)} = \mathbf{U}^{(m)} \tag{4.32}$$

At each stage the state vector is converted back into a primitive state vector, $\mathbf{W}$, for flux calculations. Original code for the explicit MHD flux solver was by Linde[28].

It was incorporated into OSCAR's explicit update by the author and extended to include the split magnetic field.

4.5 Implicit Update

The author derived and implemented a fully implicit version of the symmetrizable ideal MHD equations in OSCAR as follows. Given a hyperbolic system of PDEs in a finite volume formulation with $\mathbf{U}$ as a conservative state vector and $\mathbf{F}$ as the interface flux, the differential equation is

$$\frac{d\mathbf{U}}{dt} + \frac{1}{V}\sum_{faces} \mathbf{F}\cdot\hat{\mathbf{n}}ds = \mathbf{S} \tag{4.33}$$

For this implicit derivation, we start with the future time step $(n+1)$ and work backwards.

$$\frac{d\mathbf{U}^{n+1}}{dt} + \frac{1}{V}\sum_{faces} \mathbf{F}^{n+1}\cdot\hat{\mathbf{n}}ds = \mathbf{S}^{n+1} \tag{4.34}$$

Using a Taylor's approximation, where $\delta_t\mathbf{U}^{n+1} = \mathbf{U}^{n+1} - \mathbf{U}^n$, L is left state, and R is right state.

$$\mathbf{F}^{n+1} = \mathbf{F}^n + \frac{\partial\mathbf{F}^n}{\partial\mathbf{U}_L^n}\delta_t\mathbf{U}_L^{n+1} + \frac{\partial\mathbf{F}^n}{\partial\mathbf{U}_R^n}\delta_t\mathbf{U}_R^{n+1} \tag{4.35}$$

$$\mathbf{S}^{n+1} = \mathbf{S}^n + \frac{d\mathbf{S}^n}{d\mathbf{U}^n}\delta_t\mathbf{U}^{n+1} \tag{4.36}$$

Assume left state is the current cell's state and the right state is the neighboring cell's state value or a boundary condition state, marked with $*$.

$$\frac{\delta_t\mathbf{U}^{n+1}}{\Delta t} + \frac{1}{V}\sum_{faces}\left(\mathbf{F}^n + \frac{\partial\mathbf{F}^n}{\partial\mathbf{U}^n}\delta_t\mathbf{U}^{n+1} + \frac{\partial\mathbf{F}^n}{\partial\mathbf{U}_*^n}\delta_t\mathbf{U}_*^{n+1}\right)\cdot\hat{\mathbf{n}}ds = \mathbf{S}^n + \frac{\partial\mathbf{S}^n}{\partial\mathbf{U}^n}\delta_t\mathbf{U}^{n+1} \tag{4.37}$$

Separate n and $n+1$ terms.

$$\frac{\delta_t \mathbf{U}^{n+1}}{\Delta t} + \frac{1}{V}\sum_{faces}\left(\frac{\partial \mathbf{F}^n}{\partial \mathbf{U}^n}\delta_t \mathbf{U}^{n+1} + \frac{\partial \mathbf{F}^n}{\partial \mathbf{U}_*^n}\delta_t \mathbf{U}_*^{n+1}\right)\cdot \hat{\mathbf{n}} ds - \frac{\partial \mathbf{S}^n}{\partial \mathbf{U}^n}\delta_t \mathbf{U}^{n+1} = -\frac{1}{V}\sum_{faces}\mathbf{F}^n \cdot \hat{\mathbf{n}} ds + \mathbf{S}^n \quad (4.38)$$

Convert to $\mathbf{Ax} = \mathbf{b}$ form where $\mathbf{Q}$ is the vector of state vectors $\mathbf{U}$.

$$\left[\frac{\mathbf{I}}{\Delta t} + \frac{\partial \mathcal{F}^n}{\partial \mathbf{Q}^n} - \frac{\partial \mathcal{S}^n}{\partial \mathbf{Q}^n}\right]\delta_t \mathbf{Q}^{n+1} = -Residual(\mathbf{Q}^n) = \frac{\delta_t \mathbf{Q}^n}{\Delta t} \quad (4.39)$$

where $\frac{\partial \mathcal{F}^n}{\partial \mathbf{Q}^n}$ and $\frac{\partial \mathcal{S}^n}{\partial \mathbf{Q}^n}$ are matrix representations for the $\frac{1}{V}\sum_{faces}\left(\frac{\partial \mathbf{F}^n}{\partial \mathbf{U}^n} + \frac{\partial \mathbf{F}^n}{\partial \mathbf{U}_*^n}\right)\cdot \hat{\mathbf{n}} ds$ terms and $\frac{\partial \mathbf{S}^n}{\partial \mathbf{U}^n}$ terms.

The inclusion of a split magnetic field in the formulation results in the expansion of the $\frac{\partial \mathcal{F}^n}{\partial \mathbf{Q}^n}$ term to include perturbation and background magnetic field fluxes, $\frac{1}{V}\sum_{faces}\left(\frac{\partial \mathbf{F}_1^n}{\partial \mathbf{U}^n} + \frac{\partial \mathbf{F}_1^n}{\partial \mathbf{U}_*^n}\right)\cdot \hat{\mathbf{n}} ds$ terms and $\frac{1}{V}\sum_{faces}\left(\frac{\partial \mathbf{G}^n}{\partial \mathbf{U}^n} + \frac{\partial \mathbf{G}^n}{\partial \mathbf{U}_*^n}\right)\cdot \hat{\mathbf{n}} ds$ terms, as defined in 4.3.4.

4.6 Flux Functions

Up to this point both the explicit and implicit schemes have been derived using a generic flux function, $\mathbf{F}$, and its derivative. In the split magnetic field derivation, there is an additional flux, $\mathbf{G}$, and its derivative. A Roe approximate Riemann solver is the primary flux function in this work.

Starting with a traditional Roe average flux function,

$$\mathbf{F}(\mathbf{U}_L, \mathbf{U}_R) = \frac{1}{2}(\mathbf{F}_L + \mathbf{F}_R) - \frac{1}{2}|\mathbf{A}|(\mathbf{U}_R - \mathbf{U}_L), \quad (4.40)$$

and substituting $|\mathbf{A}| = \mathbf{L}|\mathbf{\Lambda}|\mathbf{R}$, $\mathbf{F}_L = \mathbf{A}_L\mathbf{U}_L$, and $\mathbf{F}_R = \mathbf{A}_R\mathbf{U}_R$, gives

$$\mathbf{F}(\mathbf{U}_L, \mathbf{U}_R) = \frac{1}{2}(\mathbf{A}_L\mathbf{U}_L + \mathbf{A}_R\mathbf{U}_R) - \frac{1}{2}\mathbf{L}|\mathbf{\Lambda}|\mathbf{R}(\mathbf{U}_R - \mathbf{U}_L), \quad (4.41)$$

where $\mathbf{A}_L = \mathbf{A}(\mathbf{U}_L)$ and $\mathbf{A}_R = \mathbf{A}(\mathbf{U}_R)$. $\mathbf{L}$ and $\mathbf{R}$ are calculated using a simple state average, $\mathbf{U} = \frac{\mathbf{U}_L + \mathbf{U}_R}{2}$. While $|\mathbf{\Lambda}|$ wave speeds are calculated using the simple state average, an entropy fix is applied to the magneto-acoustic waves only based on the left and right states to exclude any unphysical expansion shocks.

$$|\lambda_k^*| = \begin{cases} |\lambda_k|, & |\lambda_k| \geq \frac{\delta\lambda_k}{2} \\ \frac{\lambda_k^2}{\delta\lambda_k} + \frac{\delta\lambda_k}{4}, & |\lambda_k| < \frac{\delta\lambda_k}{2} \end{cases} \tag{4.42}$$

where $\delta\lambda_k = max(4(\lambda_{kR} - \lambda_{kL}), 0)$.

See Appendix A for the complete MHD Roe approximate Riemann solver eigenvectors, $\mathbf{A}(\mathbf{U})$, $\mathbf{L}$, $|\mathbf{\Lambda}|$, and $\mathbf{R}$. For a more general and complete derivation see Powell et al.[34]

4.6.1 Flux function derivatives

For an implicit finite volume scheme based on the formulation above, the derivative of the flux vector is necessary, which is a component of the $\mathbb{A}$ matrix in $\mathbb{A}\mathbf{x} = \mathbf{b}$ implicit system. To find $\partial\mathbf{F}/\partial\mathbf{U}$, one takes the derivative of a particular flux function. For example, begin with a traditional Roe average flux function,

$$\begin{aligned} \mathbf{f}(\mathbf{u}_L, \mathbf{u}_R) &= \mathbf{f}_L + \mathbf{A}_\mathbf{m}(\mathbf{u}_R - \mathbf{u}_L) \\ &= \mathbf{f}_R - \mathbf{A}_\mathbf{p}(\mathbf{u}_R - \mathbf{u}_L) \\ &= \frac{1}{2}(\mathbf{f}_L + \mathbf{f}_R) - \frac{1}{2}|\mathbf{A}|(\mathbf{u}_R - \mathbf{u}_L). \end{aligned} \tag{4.43}$$

Taking the derivative of the flux function gives

$$\frac{\partial\mathbf{f}}{\partial\mathbf{u}_L} = \frac{1}{2}\frac{d\mathbf{f}_L}{d\mathbf{u}_L} - \frac{1}{2}\left(-|\mathbf{A}| + \frac{\partial|\mathbf{A}|}{\partial\mathbf{u}_L}(\mathbf{u}_R - \mathbf{u}_L)\right). \tag{4.44}$$

$\frac{\partial|\mathbf{A}|}{\partial\mathbf{u}_L}$ is truly ugly. Since we plan to use this to create a matrix, $\mathbb{A}$, which will be assumed constant as part of a linear system, we can assume that $|\mathbf{A}|$ is constant allowing us to simplify the result further.

$$\frac{\partial\mathbf{f}}{\partial\mathbf{u}_L} = \frac{1}{2}\frac{d\mathbf{f}_L}{d\mathbf{u}_L} + \frac{1}{2}|\mathbf{A}| \tag{4.45}$$

Using the Jacobian, $\frac{d\mathbf{f}_L}{d\mathbf{u}_L} = \mathbf{A}_L$, we get the following

$$\frac{\partial\mathbf{f}}{\partial\mathbf{u}_L} = \frac{1}{2}\mathbf{A}_L + \frac{1}{2}|\mathbf{A}| \tag{4.46}$$

and similarly

$$\frac{\partial\mathbf{f}}{\partial\mathbf{u}_R} = \frac{1}{2}\mathbf{A}_R - \frac{1}{2}|\mathbf{A}|. \tag{4.47}$$

However, this form assumes a one-dimensional flux, although with 3-D states and used in 3-D simulations. Often, a further simplifying assumption is that the direction of the flux is aligned with the x-axis and the $\hat{\mathbf{n}}$ vector is (1,0,0). By defining $\mathbf{K}$ as a transformation matrix that converts from simulation coordinates $(\hat{x}, \hat{y}, \hat{z})$ to the flux normal coordinates $(\hat{n}, \hat{\tau}_1, \hat{\tau}_2)$ where the $\hat{\tau}$s are perpendicular axes, we can write the above in more general form where $\mathbf{F}$ and $\mathbf{U}$ are in simulation coordinates.

$$\begin{aligned}\mathbf{F}(\mathbf{U}_L, \mathbf{U}_R, \mathbf{K}) = \mathbf{K}^{-1}\Bigg(&\frac{1}{2}\left(\mathbf{F}_L(\mathbf{K}\mathbf{U}_L) + \mathbf{F}_R(\mathbf{K}\mathbf{U}_R)\right)\\ &-\frac{1}{2}|\mathbf{A}(\mathbf{K}\mathbf{U}_L, \mathbf{K}\mathbf{U}_R)|\left[\mathbf{K}\mathbf{U}_R - \mathbf{K}\mathbf{U}_L\right]\Bigg)\end{aligned} \tag{4.48}$$

Taking the derivative of the flux function gives

$$\begin{aligned}\frac{\partial\mathbf{F}}{\partial\mathbf{U}_L} = \mathbf{K}^{-1}\Bigg(&\frac{1}{2}\frac{d\mathbf{F}_L(\mathbf{K}\mathbf{U}_L)}{d\mathbf{U}_L} - \frac{1}{2}\Big(-|\mathbf{A}(\mathbf{K}\mathbf{U}_L, \mathbf{K}\mathbf{U}_R)|\mathbf{K}\\ &+\frac{\partial|\mathbf{A}(\mathbf{K}\mathbf{U}_L, \mathbf{K}\mathbf{U}_R)|}{\partial\mathbf{U}_L}\left[\mathbf{K}\mathbf{U}_R - \mathbf{K}\mathbf{U}_L\right]\Big)\Bigg).\end{aligned} \tag{4.49}$$

Eliminating $\frac{\partial|\mathbf{A}(\mathbf{KU}_L,\mathbf{KU}_R)|}{\partial \mathbf{U}_L}$ as before,

$$\frac{\partial \mathbf{F}}{\partial \mathbf{U}_L} = \mathbf{K}^{-1}\left(\frac{1}{2}\frac{d\mathbf{F}_L(\mathbf{KU}_L)}{d\mathbf{U}_L} + \frac{1}{2}|\mathbf{A}(\mathbf{KU}_L,\mathbf{KU}_R)|\mathbf{K}\right). \tag{4.50}$$

Using $\frac{d\mathbf{F}_L(\mathbf{KU}_L)}{d\mathbf{U}_L} = \frac{d\mathbf{F}_L(\mathbf{KU}_L)}{d\mathbf{KU}_L}\frac{d\mathbf{KU}_L}{d\mathbf{U}_L} = \mathbf{A}_L(\mathbf{KU}_L)\mathbf{K}$, we get the following

$$\frac{\partial \mathbf{F}}{\partial \mathbf{U}_L} = \mathbf{K}^{-1}\left(\frac{1}{2}\mathbf{A}_L(\mathbf{KU}_L)\mathbf{K} + \frac{1}{2}|\mathbf{A}(\mathbf{KU}_L,\mathbf{KU}_R)|\mathbf{K}\right) \tag{4.51}$$

or

$$\frac{\partial \mathbf{F}}{\partial \mathbf{U}_L} = \mathbf{K}^{-1}\left(\frac{1}{2}\mathbf{A}_L(\mathbf{KU}_L) + \frac{1}{2}|\mathbf{A}(\mathbf{KU}_L,\mathbf{KU}_R)|\right)\mathbf{K} \tag{4.52}$$

and similarly

$$\frac{\partial \mathbf{F}}{\partial \mathbf{U}_R} = \mathbf{K}^{-1}\left(\frac{1}{2}\mathbf{A}_R(\mathbf{KU}_R) - \frac{1}{2}|\mathbf{A}(\mathbf{KU}_L,\mathbf{KU}_R)|\right)\mathbf{K}. \tag{4.53}$$

Additionally, the split magnetic field flux, $\mathbf{G}$, from Section 4.3.4 also has a relatively straightforward derivative. Both flux derivatives can be found in Appendix B.

4.6.2 Source terms

Using the symmetrizable form of the MHD equations, we have corrective source terms as described previously in 4.3.4. In addition, our GDM simulations involve actual source terms in two forms. First, the injection of relatively cool plasma into the center of the GDM confinement field requires an arbitrarily set mass flow that is distributed over a spherical volume. Given that the plasma is assumed to have some initial temperature, there is a small energy flux also associated with the mass injection. Second, there are fusion energy and radiation loss source terms.

$$\mathbf{S}_1 = -\nabla\cdot\mathbf{B}_1\begin{pmatrix} 0 \\ \mathbf{B} \\ \mathbf{u} \\ \mathbf{u}\cdot\mathbf{B}_1 \end{pmatrix} \tag{4.54}$$

$$\frac{\partial \mathbf{S}}{\partial \mathbf{U}_L} = \begin{bmatrix} 0 & 0 & 0 & 0 & 0 & 0 & 0 & 0 \\ 0 & 0 & 0 & 0 & B_n + \frac{B_x}{2} & 0 & 0 & 0 \\ 0 & 0 & 0 & 0 & \frac{B_y}{2} & B_n & 0 & 0 \\ 0 & 0 & 0 & 0 & \frac{B_z}{2} & 0 & B_n & 0 \\ \frac{-B_n u}{\rho} & \frac{B_n}{\rho} & 0 & 0 & \frac{u}{2} & 0 & 0 & 0 \\ \frac{-B_n v}{\rho} & 0 & \frac{B_n}{\rho} & 0 & \frac{v}{2} & 0 & 0 & 0 \\ \frac{-B_n w}{\rho} & 0 & 0 & \frac{B_n}{\rho} & \frac{w}{2} & 0 & 0 & 0 \\ \frac{-B_n(\mathbf{u}\cdot\mathbf{B})}{\rho} & \frac{B_x B_n}{\rho} & \frac{B_y B_n}{\rho} & \frac{B_z B_n}{\rho} & \frac{(\mathbf{u}\cdot\mathbf{B})}{2} + B_n u & v B_n & w B_n & 0 \end{bmatrix} \tag{4.55}$$

where $B_n = (B_{Lx} + B_{Rx})/2$.

$$\frac{\partial \mathbf{S}}{\partial \mathbf{U}_R} = \begin{bmatrix} 0 & 0 & 0 & 0 & 0 & 0 & 0 & 0 \\ 0 & 0 & 0 & 0 & \frac{B_x}{2} & 0 & 0 & 0 \\ 0 & 0 & 0 & 0 & \frac{B_y}{2} & 0 & 0 & 0 \\ 0 & 0 & 0 & 0 & \frac{B_z}{2} & 0 & 0 & 0 \\ 0 & 0 & 0 & 0 & \frac{u}{2} & 0 & 0 & 0 \\ 0 & 0 & 0 & 0 & \frac{v}{2} & 0 & 0 & 0 \\ 0 & 0 & 0 & 0 & \frac{w}{2} & 0 & 0 & 0 \\ 0 & 0 & 0 & 0 & \frac{(\mathbf{u}\cdot\mathbf{B})}{2} & 0 & 0 & 0 \end{bmatrix} \tag{4.56}$$

Two types of radiative losses are considered: bremsstrahlung and synchrotron radiation. Bremsstrahlung radiation results from the deceleration of energetic electrons due to collisions in the plasma. Synchrotron radiation originates from the interaction of charged particles with a magnetic field. Synchrotron radiation is the same as cyclotron radiation, but corrected for relativistic effects.

From Stacey[40], we use

$$\mathbf{P}_b = 4.8 \times 10^{-43} z^2 n_i n_e T_e^{\frac{1}{2}} [MW/m^3] \tag{4.57}$$

for the bremsstrahlung power loss, where z is the average charge of the ions, the densities are in $[\#/m^3]$, and the electron temperature is in $[keV]$. The densities and temperature are simplified by assuming $n_e = zn_i = zn$ and $T_e = T_i = T$. Additionally, the equation needs to be non-dimensionalized using the terms ρ_∞, a_∞, and L_∞.

$$n[\#/m^3] = 6.02214179 \times 10^{23} \frac{\rho\rho_\infty}{m} \tag{4.58}$$

and from $p = n_e kT_e + n_i kT_i = (z+1)nkT$

$$T[keV] = 1.03642686 \times 10^{-8} \frac{m}{1+z} a_\infty^2 \frac{p}{\rho} \tag{4.59}$$

where m is the average molecular weight in $[kg/mole]$ and p and ρ are non-dimensional values. Substituting the simplified non-dimensional forms into P_b equation above, one gets

$$\mathbf{P}_b = 1.8 \times 10^7 \frac{z^3}{m^{3/2}(z+1)^{1/2}} \rho_\infty^2 a_\infty p^{1/2} \rho^{3/2} [W/m^3]. \tag{4.60}$$

Converting to a non-dimensionalized energy source term requires dividing by $\rho_\infty a_\infty^3 / L_\infty$ and results in

$$\mathbf{S}_b = -1.8 \times 10^7 \frac{z^3}{m^{3/2}(z+1)^{1/2}} \frac{\rho_\infty L_\infty}{a_\infty^2} p^{1/2} \rho^{3/2}. \tag{4.61}$$

Finally, the implicit algorithm will also need the Jacobian,

$$\frac{\partial \mathbf{S}_b}{\partial \mathbf{U}} = \begin{bmatrix} 0 & 0 & 0 & 0 & 0 & 0 & 0 & 0 \\ 0 & 0 & 0 & 0 & 0 & 0 & 0 & 0 \\ 0 & 0 & 0 & 0 & 0 & 0 & 0 & 0 \\ 0 & 0 & 0 & 0 & 0 & 0 & 0 & 0 \\ 0 & 0 & 0 & 0 & 0 & 0 & 0 & 0 \\ 0 & 0 & 0 & 0 & 0 & 0 & 0 & 0 \\ 0 & 0 & 0 & 0 & 0 & 0 & 0 & 0 \\ \frac{3}{2} k_b p^{\frac{1}{2}} \rho^{\frac{1}{2}} + \frac{q^2}{2} h_b & -u h_b & -v h_b & -w h_b & -B_x h_b & -B_y h_b & -B_z h_b & h_b \end{bmatrix} \tag{4.62}$$

where $k_b = -1.7722 \times 10^7 \frac{z^3}{m^{3/2}(z+1)^{1/2}} \frac{\rho_\infty L_\infty}{a_\infty^2}$ is a constant containing all the parameters for a specified case and $h_b = \frac{k_b(\gamma-1)}{2} \frac{\rho^{\frac{3}{2}}}{p^{\frac{1}{2}}}$ is a holding variable to simplify the expression.

To model synchrotron radiation, we use

$$\mathbf{P}_s = 6.2 \times 10^{-17} B_f^2 n_e T_e \left(1 + T_e/204\right) [W/m^3] \tag{4.63}$$

from Rose[36] where B_f is in Tesla, n_e is $[\#/m^3]$, and T is in [keV]. Using the substitutions above, $B_f^2 = B^2 a_\infty^2 \rho_\infty \mu_0$, and dividing by $\rho_\infty a_\infty^3 / L_\infty$ gives

$$\mathbf{S}_s = -.387 \frac{z}{z+1} a_\infty \rho_\infty \mu_0 L_\infty B^2 p (1 - 5.08 \times 10^{-17} a_\infty^2 \frac{m}{z+1} \frac{p}{\rho}). \tag{4.64}$$

Again, taking $k_{s1} = -.387 \frac{z}{z+1} a_\infty \rho_\infty \mu_0 L_\infty$ and $k_{s2} = 5.08 \times 10^{-17} a_\infty^2 \frac{m}{z+1}$, we find the Jacobian to be

$$\frac{\partial \mathbf{S}_b}{\partial \mathbf{U}} = \begin{bmatrix} 0 & 0 & 0 & 0 & 0 & 0 & 0 & 0 \\ 0 & 0 & 0 & 0 & 0 & 0 & 0 & 0 \\ 0 & 0 & 0 & 0 & 0 & 0 & 0 & 0 \\ 0 & 0 & 0 & 0 & 0 & 0 & 0 & 0 \\ 0 & 0 & 0 & 0 & 0 & 0 & 0 & 0 \\ 0 & 0 & 0 & 0 & 0 & 0 & 0 & 0 \\ 0 & 0 & 0 & 0 & 0 & 0 & 0 & 0 \\ -\frac{k_{s1} B^2 p^2}{\rho^2} - \frac{h_{s1} q^2}{2} & -u h_{s1} & -v h_{s1} & -w h_{s1} & B_x h_{s2} & B_y h_{s2} & B_z h_{s2} & h_{s1} \end{bmatrix} \tag{4.65}$$

with $h_{s1} = -k_{s1} \mathbf{B}^2 (\gamma - 1) \left(1 - \frac{2 k_{s2} p}{\rho}\right)$ and $h_{s2} = -2 p k_{s1} (1 - \frac{k_{s2} p}{\rho}) - h_{s1}$

The fusion power generated by any two species, designated here with subscripts as the lighter and heavier components, can be written

$$\mathbf{P}_f = n_L n_H \langle \sigma v \rangle E_0 \tag{4.66}$$

where n is the particle density $[\#/m^3]$, E_0 is the energy produced in a single fusion reaction, and the velocity-averaged cross-section, $\langle \sigma v \rangle$, in $[m^3/s\#]$ is replaced with

function of temperature unique to each pairing of fusion fuels. Taking f to be the fraction of the lighter fuel gives $n_L = fn$ and $n_H = (1-f)n$. Using the substitution for n above and accounting for units, we get

$$\mathbf{P}_F = 5.810 \times 10^{34} \rho_\infty^2 \frac{f(1-f)}{m^2} E_0 \langle \sigma v \rangle \rho^2 [W/m^3] \tag{4.67}$$

with $\langle \sigma v \rangle$ in $[m^3/s\#]$, m in $[kg/mole]$, E_0 in $[MeV/\#]$, and ρ non-dimensional. Finally, dividing by $\rho_\infty a_\infty^3 / L_\infty$ to complete the non-dimensionalization, we get

$$\mathbf{S}_F = 5.810 \times 10^{34} \frac{f(1-f)}{m^2} E_0 \frac{\rho_\infty L_\infty}{a_\infty^3} \langle \sigma v \rangle \rho^2. \tag{4.68}$$

Setting $k_f = 5.810 \times 10^{34} \frac{f(1-f)}{m^2} E_0 \frac{\rho_\infty L_\infty}{a_\infty^3}$, the corresponding Jacobian is

$$\frac{\partial \mathbf{S}_f}{\partial \mathbf{U}} = \begin{bmatrix} 0 & 0 & 0 & 0 & 0 & 0 & 0 & 0 \\ 0 & 0 & 0 & 0 & 0 & 0 & 0 & 0 \\ 0 & 0 & 0 & 0 & 0 & 0 & 0 & 0 \\ 0 & 0 & 0 & 0 & 0 & 0 & 0 & 0 \\ 0 & 0 & 0 & 0 & 0 & 0 & 0 & 0 \\ 0 & 0 & 0 & 0 & 0 & 0 & 0 & 0 \\ 0 & 0 & 0 & 0 & 0 & 0 & 0 & 0 \\ \frac{q^2}{2} h_f + 2k_f \langle \sigma v \rangle \rho + k_f \rho^2 \frac{\partial \langle \sigma v \rangle}{\partial \rho} & -uh_f & -vh_f & -wh_f & -B_x h_f & -B_y h_f & -B_z h_f & h_f \end{bmatrix} \tag{4.69}$$

with $h_f = k_f \rho^2 (\gamma - 1) \frac{\partial \langle \sigma v \rangle}{\partial p}$. To implement the fusion energy source term requires $\langle \sigma v \rangle$, $\frac{\partial \langle \sigma v \rangle}{\partial \rho}$, and $\frac{\partial \langle \sigma v \rangle}{\partial p}$. For deuterium-tritium, $D-T$, it is

$$\langle \sigma v \rangle_{DT} = 1.66058 \times 10^{-30} \Big(8.29 \times 10^{10} T^{-2/3} e^{(-4.524 T^{-2/3} - 156.25 T^2)} \big(1 + 17.2T + 175T^2\big) + 8.12 \times 10^8 T^{-.712} e^{(-.506 T^{-1})} \Big) \tag{4.70}$$

where T is in $[K/10^9]$. $T[K/10^9]$, in terms of the non-dimensionalized p and ρ, is $T = 1.204 \times 10^{-10} \frac{ma_\infty^2}{z+1} \frac{p}{\rho} = k_T p/\rho$, which gives

$$\langle \sigma v \rangle_{DT} = 1.66058 \times 10^{-30} \left(8.29 \times 10^{10} (\frac{pk_T}{\rho})^{-2/3} e^{(-4.524(\frac{pk_T}{\rho})^{-2/3} - 156.25(\frac{pk_T}{\rho})^2)} \left(1 + 17.2(\frac{pk_T}{\rho}) + 175(\frac{pk_T}{\rho})^2 \right) + 8.12 \times 10^8 (\frac{pk_T}{\rho})^{-.712} e^{(-.506(\frac{pk_T}{\rho})^{-1})} \right). \quad (4.71)$$

Differentiating $\langle \sigma v \rangle_{DT}$, the derivatives in terms of p and ρ are

$$\frac{\partial \langle \sigma v \rangle_{DT}}{\partial p} = 1.66058 \times 10^{-30} \left(\left(\frac{4.753 \times 10^{11} (\frac{pk_T}{\rho})^{1/3} + 4.375 \times 10^{13} (\frac{pk_T}{\rho})^{2/3}}{p} + \frac{4.300 \times 10^{12} \rho (\frac{pk_T}{\rho})^{2/3} - 5.527 \times 10^{10} (\frac{pk_T}{\rho})^{1/3}}{k_T p^2} + \frac{2.500 \times 10^{11} \rho^2 (\frac{pk_T}{\rho})^{2/3}}{k_T^2 p^3} - \frac{6.563 \times 10^{12} k_T (\frac{pk_T}{\rho})^{1/3}}{\rho} - \frac{4.456 \times 10^{14} k_T^2 p (\frac{pk_T}{\rho})^{1/3}}{\rho^2} - \frac{4.534 \times 10^{15} k_T^3 p^2 (\frac{pk_T}{\rho})^{1/3}}{\rho^3} \right) e^{(\frac{-4.524}{(\frac{pk_T}{\rho})^{2/3}} - 156.25(\frac{pk_T}{\rho})^2)} + \left(-\frac{5.781 \times 10^8 k_T}{\rho (\frac{pk_T}{\rho})^{1.712}} + \frac{4.109 \times 10^8 \rho}{p^2 k_T (\frac{pk_T}{\rho})^{0.712}} \right) e^{(-.506(\frac{pk_T}{\rho})^{-1})} \right) \quad (4.72)$$

and

$$\frac{\partial \langle \sigma v \rangle_{DT}}{\partial \rho} = 1.66058 \times 10^{-30} \left(\left(\frac{4.375 \times 10^{13} (\frac{pk_T}{\rho})^{2/3} - 4.753 \times 10^{11} (\frac{pk_T}{\rho})^{1/3}}{\rho} + \frac{5.527 \times 10^{10} (\frac{pk_T}{\rho})^{1/3} - 4.300 \times 10^{12} (\frac{pk_T}{\rho})^{2/3}}{k_T p} + \frac{2.500 \times 10^{11} \rho (\frac{pk_T}{\rho})^{2/3}}{k_T^2 p^2} + \frac{6.563 \times 10^{12} p k_T (\frac{pk_T}{\rho})^{1/3}}{\rho^2} + \frac{4.456 \times 10^{14} k_T^2 p^2 (\frac{pk_T}{\rho})^{1/3}}{\rho^3} + \frac{4.534 \times 10^{15} k_T^3 p^3 (\frac{pk_T}{\rho})^{1/3}}{\rho^4} \right) e^{(\frac{-4.524}{(\frac{pk_T}{\rho})^{2/3}} - 156.25(\frac{pk_T}{\rho})^2)} + \left(\frac{5.781 \times 10^8 k_T p}{\rho^2 (\frac{pk_T}{\rho})^{1.712}} - \frac{4.109 \times 10^8}{k_T p (\frac{pk_T}{\rho})^{0.712}} \right) e^{\frac{-.506}{(\frac{pk_T}{\rho})}} \right). \quad (4.73)$$

4.7 Parallel Implementation and PETSc

The introduction of an implicit scheme into OSCAR increased the computational demand compared to the original explicit scheme by roughly an order of magnitude. In order to compensate for this, the implicit scheme was parallelized from the outset.

Given the unstructured and octree format of OSCAR's Cartesian grid, the implicit system described above produces a sparse **A** matrix that is heavily block-diagonally based, but is definitely not structured or symmetric. The Parallel Extensible Toolkit for Scientific (PETSc) computing library was chosen due to its plethora of numerical, iterative methods for solving sparse systems. By integrating this package into OSCAR as the parallel solver for our implicit system, the user has a large selection of iterative algorithms and preconditioners to choose from.

In the original implementation, OSCAR generated the grid and computed all the elements of the implicit system serially. PETSc could then assemble and solve the implicit system in parallel. While trivial to implement, it became apparent that the serial calculation of the matrix and vector elements was more than half the computational runtime. As such, generation of the implicit system was also parallelized. Since geometry generation and grid adaption only occur occasionally, those aspects of OSCAR remain serial.

On overview of OSCAR's parallel implementation is as follows:

- a grid is generated/adapted serially by the master process
- cell volumes and interface characteristics (areas, normals, and neighboring cell indexes) are broadcast once to all processes
- solver is started

- all cell states and gradients, if 2nd order, are broadcast to all processes
- in parallel, each process works through its share of the interface list calculating block elements of the **A** matrix, beginning with general interfaces then calculating boundary interfaces
- in parallel, each process works through its share of the cell list calculating the local time step, modifying that according to input parameters, and generating $\mathbf{I}/\Delta t$
- in parallel, each process works through its share of the cell list calculating source term elements of the **A** matrix and explicit residuals

4.8 Generating Background Magnetic Fields

Whether using standard MHD or the split magnetic field formulation, there is often a background magnetic field for each MHD simulation. There are three different types of background magnetic fields that can be imposed using OSCAR: uniform, simple mirror field, and arbitrary current segments.

4.8.1 Uniform B-field

A given magnetic vector, $\mathbf{B} = (B_x, B_y, B_z)$, is imposed throughout the simulation. Such fields were used for shock polar validation cases.

4.8.2 Simple Mirror Field

A GDM system is composed of two axisymmetric magnetic mirrors. The magnetic fields of the axisymmetric mirrors can be represented by the following equations

$$B_z = B_0 \left[1 - \alpha cos(u) I_0(\rho)\right] \tag{4.74}$$

$$B_r = B_0 \alpha sin(u) I_1(\rho) \tag{4.75}$$

where

$$u = \frac{2\pi z}{L} \quad \rho = \frac{2\pi r}{L} \quad \alpha = \frac{R_m - 1}{R_m + 1}$$

with R_m being the mirror ratio and I_n is a modified Bessel function. This is illustrated in Figure 4.2.[33] In general, this field is overly simplistic for representing GDM designs.

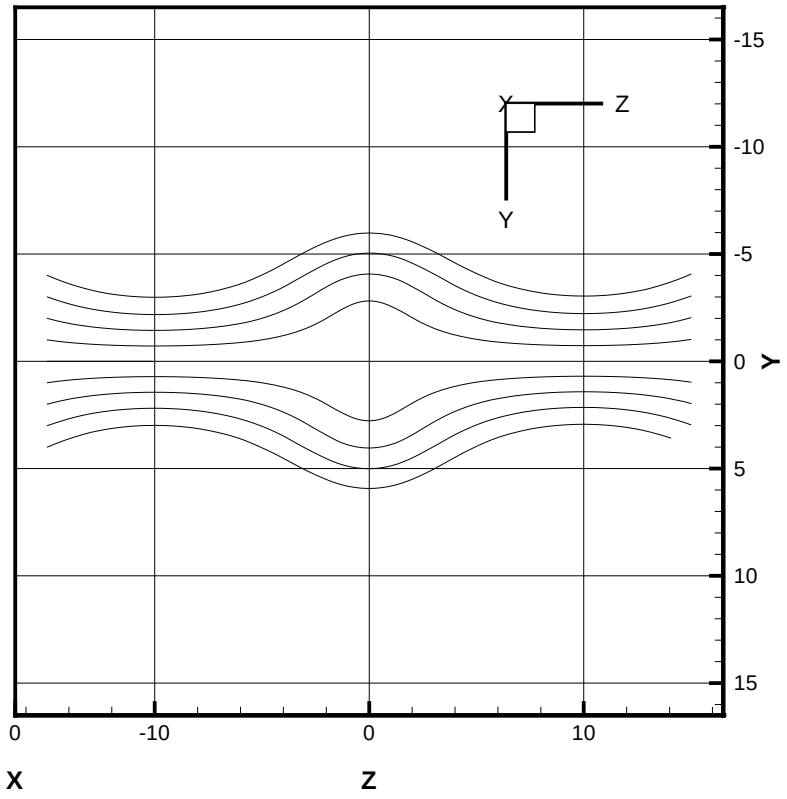

Figure 4.2: Magnetic field lines for simple mirror containment field.

4.8.3 Arbitrary Current Segments

The most flexible method for generating background magnetic fields is to define line segments with a specified current flow. The magnetic field at a particular cell

centroid is the summation of all the Biot-Savart contributions from each and every current segment.

$$\mathbf{B} = \sum_{all\ segments} d\mathbf{B} = \sum_{all\ segments} \frac{\mu_0}{4\pi} \frac{i\ d\mathbf{s} \times \hat{\mathbf{r}}}{r^2}, \tag{4.76}$$

where $\mathbf{r}$ is the vector difference from the center of the line segment to the cell centroid and $d\mathbf{s}$ is the length of the line segment. This formulation requires that $\mathbf{r} \gg d\mathbf{s}$. The current segments cannot be directly in the flow, but must be contained within geometries in the flow simulation or outside the flow domain. OSCAR checks for this and produces warnings when $\mathbf{r}$ approaches $d\mathbf{s}$.

Current segments are automatically generated by OSCAR to represent ring magnets given the ring magnet's center, radius, normal vector, and current.

4.8.4 B_0 Field Divergence

Physically, the divergence of the magnetic field is zero, $\nabla \cdot \mathbf{B} = 0$. However, the discretization of the domain in a numerical method introduces some small divergence into each cell. Using the complete MHD equations without dropping the $\nabla \cdot \mathbf{B}$ source terms, as described above, results in an 8-wave model which dissipates any divergence in the magnetic field due to numerical error. In the split magnetic field version, the background magnetic field is assumed to have no divergence. When the background magnetic field is calculated as described in the following sections, it also has non-zero divergence due to discretization errors.

In an attempt to remove this divergence, a Brackbill and Barnes projection method that solves a Poisson equation for the divergence error in the magnetic field was implemented.[6] Any vector field can be decomposed into separate curl and divergence components, $\mathbf{B} = \nabla \times \psi + \nabla\phi$. Taking the divergence of that equation gives $\nabla \cdot B = \nabla^2\phi$. Solving the Poisson problem, $\nabla^2\phi = \nabla \cdot B$, produces ϕ. The

gradient of ϕ is the divergence of the given magnetic field; subtract from the field to obtain a new divergence-free magnetic field, $\mathbf{B}^* = \mathbf{B} - \nabla\phi$.

To solve the Poisson problem on OSCAR's Cartesian grid, each cell is assumed to be the center of a 3D, centered, 7-point stencil. Each neighboring point is presumed to be at the cell center of a similarly sized cell at a distance of the cell's dimension, Δl. In its simplest form, the update equation would look like

$$\phi_{ijk}^{n+1} = \frac{\phi_{i-1}^n + \phi_{i+1}^n + \phi_{j-1}^n + \phi_{j+1}^n + \phi_{k-1}^n + \phi_{k+1}^n + \Delta l^2 \nabla \cdot \mathbf{B}}{6} \tag{4.77}$$

.

Due to stretch mapping ability in OSCAR, the cells are not necessarily cubic. Replacing Δl with Δx, Δy, and Δz, we get

$$\begin{aligned}\phi_{ijk}^{n+1} =& \Big(\Delta y^2\Delta z^2(\phi_{i-1}^n + \phi_{i+1}^n) + \Delta x^2\Delta z^2(\phi_{j-1}^n + \phi_{j+1}^n) + \\ & \Delta x^2\Delta y^2(\phi_{k-1}^n + \phi_{k+1}^n) + \Delta x^2\Delta y^2\Delta z^2 \nabla \cdot \mathbf{B}\Big) / \\ & \Big(2\Delta y^2\Delta z^2 + 2\Delta x^2\Delta z^2 + 2\Delta x^2\Delta y^2\Big).\end{aligned} \tag{4.78}$$

4.9 Boundary Conditions

Every computational cell is defined by a list of interfaces. If it is a simple interface, there is a neighboring cell state and a flux can be calculated between the cells. Otherwise, it is a boundary interface, where the left state is the limited cell state at the interface and the right state is determined by the boundary condition. At this point in development, OSCAR has over 20 types of boundary conditions available. Only the ones relevant to simulating GDMs are described here .

4.9.1 Far Field Boundary Conditions

Given a specified far field state, $\mathbf{U}_{FF}$, a straightforward far field BC is to simply over-specify it by using $\mathbf{U}_{FF}$ as the neighbor state at a boundary interface. Such

boundary conditions work well for supersonic Euler conditions where all the waves are traveling outward and no information about the boundary condition state is convected back into the flow simulation. In subsonic cases, over-specification can work if the flow state is close the far field state. When an error is introduced, it will be small, it will appear primarily near the boundary, and it will probably not significantly alter the total solution unless the case is strongly dependent on external conditions.

However, in this current work the MHD equations were used to model GDMs. The large magnetic fields combined with low mass densities produced very fast Alfven wave speeds, $\mathbf{V}_A = \frac{\mathbf{B}}{\sqrt{\rho}}$ in non-dimensional form. While the GDM exhaust jets are clearly supersonic, they are not necessarily superfast. The MHD equations in symmetric form have 8 waves: entropy, magnetic-flux, forward and backward running Alfven waves, and forward and backward slow and fast magneto-acoustic waves.

$$\lambda_e, \lambda_d = u_n \tag{4.79}$$

$$\lambda_A = u_n \pm B_n/\sqrt{\rho} \tag{4.80}$$

$$\lambda_{f,s} = u_n \pm c_{f,s} \tag{4.81}$$

In GDM cases, all flow at the far field boundaries is outward. This guarantees at least five of eight waves are outward. As B_t approaches zero on the outflow boundaries, the slow magneto-acoustic wave speed approaches the acoustic wave speed, $c_s \rightarrow a$. Assuming the flow is supersonic, it is possible that the backwards-traveling magneto-sonic slow wave also travels outwards, which reduces the inflowing waves from three to two.

The number of specified far field boundary properties should correlate with the number of inflowing waves. Since we prefer to specify primitive variables, we need

to consider the characteristic waves and variables to avoid specifying primitive properties that might conflict with internal properties of the flow solution.

We specify the two tangential magnetic field components and the pressure at the boundary. The density, velocity vector, normal magnetic field, and any embedded magnetic field vector are simply taken from the internal cell state.

4.9.2 Symmetric Boundary Conditions

Given the axisymmetric nature of the GDM, symmetric boundary conditions can be used on the x and y planes to reduce the simulation to 90° of the full 360°. This leaves 1/4 the volume, and therefore 1/4 the cells. Symmetric boundary conditions simply use the internal flow solution state and flip the direction of the normal velocity and magnetic field vectors.

$$\mathbf{U}^* = \mathbf{U} \tag{4.82}$$

$$u_n^* = -u_n \tag{4.83}$$

$$B_n^* = -B_n \tag{4.84}$$

$$B_{0n}^* = -B_{0n} \tag{4.85}$$

4.10 Summary

This chapter documents all the mathematical models that underlie the computational ideal-MHD model necessary for numerically simulating a GDM. It started with the non-dimensionalization of the physical parameters and Cartesian grid generation including the author's addition of magnetic-term adaptive refinement and a stretch mapping to address the extreme GDM aspect ratios. Then, ideal MHD state vectors with 2nd order gradients and the governing equations, which involve a split magnetic field formulation to account for the immense background magnetic fields

of GDM magnetic confinement system, are detailed. Explicit and implicit updates based on an approximate Roe flux function are derived. The explicit scheme was based on Charlton's original update[9] in OSCAR with the incorporation of Linde's ideal MHD Roe flux solver[28], while the implicit scheme was derived and implemented by the author. The implicit scheme is necessary to address wave speeds that can be a few percent the speed of light in a GDM and traveling waves along the length of the GDM. Source terms, both corrective terms from the symmetrizable form of the MHD equations and energy terms to account for fusion energy generation and synchrotron and bremsstrahlung radiation losses, are described along with their derivatives. The last three sections review additional improvements and extensions by the author detailing how the model was implemented on parallel computing systems using the PETSc linear solver library, how the GDM magnetic field was numerically generated, and the issues addressed by the boundary conditions.

CHAPTER V

MHD COMPUTATIONAL RESULTS

Computational results from the previously described numerical ideal-MHD 3-D algorithm are presented in three sections. First, the code was validated using shock polars, plasma flows with oblique angle shocks in perpendicular/parallel magnetic fields. Second, a GDM experimental setup was simulated to demonstrate the ability to simulate GDM magnetic containment in a realistic geometry. The GDM experiment modeled is not fusion-capable and has relatively weaker magnetic fields making the numerical simulation less demanding. Third, a full $deuterium - tritium$ $(D-T)$ GDM simulation was developed and run computationally. The goal is to confirm the viability of the GDM fusion propulsion concept with higher level of fidelity than the analytical model presented in Chapter II and provide a design tool for further refinement of the concept.

5.1 Validation with Shock Polars

Validation of the ideal MHD physics was done using shock polars. An analytical solution of the Rankine-Hugoniot relations for a normal MHD shock can be found in Tidman.[41] Oblique shock relations were derived by accounting for the velocity parallel to the shock front and angle, θ, between the B field and the velocity normal

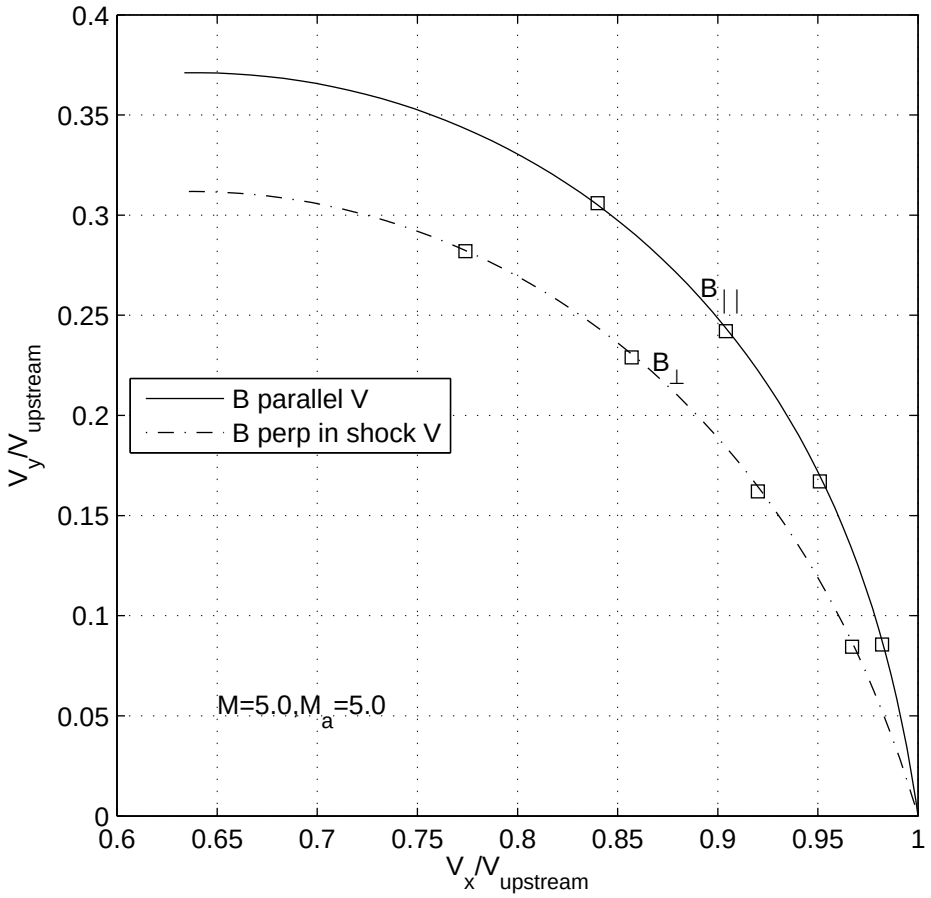

Figure 5.1: Computational shock polar solutions against the analytical solution for ideal MHD.

to the shock front. The normal MHD shock Rankine-Hugoniot relations result in a cubic equation which was solved numerically for the change in the normal velocity across the shock. After adding the shock parallel velocity component back in, the total velocity behind the oblique MHD shock for many different angles generated a shock polar curve that can be found in Figure 5.1. On top of the curves for the two cases, the magnetic field parallel to the velocity and the magnetic field perpendicular to the velocity in the plane of the shock, solutions for oblique shocks resulting from 5, 10, 15, and 20 degree wedges are plotted. The relationship between the flow velocity,

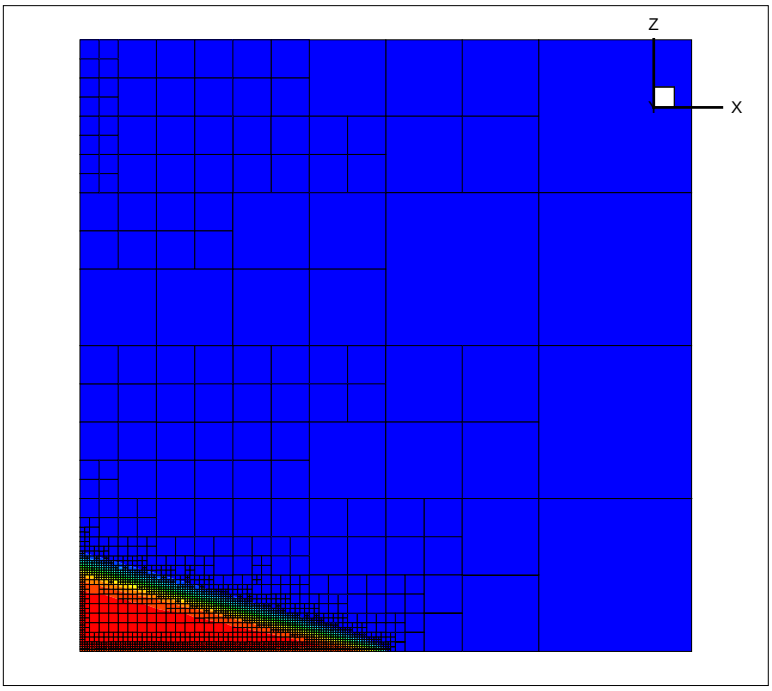

Figure 5.2: Computational shock polar solutions for parallel flow and 5 degree wedge. Flow is rotated to 5 degrees off the grid axis and the wedge half of the bottom boundary conditions is a solid wall boundary.

gasdynamic properties, and the magnetic field strength are established with the non-dimensional with the traditional and Alfvenic Mach numbers; in this case, both were 5.0. An example grid and flow solution is pictured in Figure 5.2. The computational MHD solution agrees very well with the ideal MHD analytical solutions.

5.2 Simulation of a GDM Experiment

Emrich [16] [15] built and ran experiments with a "cold," not fusion capable, experimental GDM setup at NASA Marshall Space Flight Center. His research objective was to test plasma stability in the GDM magnetic mirror when it functions as a nozzle. Specifically, he was looking at the interaction of good and bad magnetic curvature with various regimes of subsonic and supersonic flow through the mirror on the production of flute instabilities. The MHD simulation presented in this work

Figure 5.3: Picture of the experimental apparatus built by Emrich at NASA Marshall. [15]

assumes infinite conductance and cannot reproduce the flute instabilities that Emrich was documenting. The goal of simulating the Emrich experimental setup was simply to validate our GDM computational model against the closest available real world system. In the process, the ability to model any arbitrary magnetic confinement field with a high aspect ratio containing a gasdynamic plasma was demonstrated.

Main chamber length	2.0 m
Main chamber diameter	0.2 m
Mirror chamber length	0.5 m
Mirror chamber diameter	0.06 m
Number of main chamber magnets	17
Number of mirror chamber magnets	12
Magnet current	up to 3000 A
Vacuum magnetic field in chamber	up to .35 T (centerline)
Vacuum magnetic field in mirror	up to 2.05 T (centerline)
Microwave injector power	1000 W
Typical Plasma Parameters	
Plasma density	10^{13} cm^{-3}
Plasma radius	0.04 m
Plasma temperature	2 eV

Table 5.1: Physical aspects of Emrich GDMs experiment.[16]

Main chamber magnets z-position from center	+/- 0, .12, .24, .36, .48, .60, .72, .84, .96 m
Main chamber magnets radius	.30 m
Main chamber magnetic field	.05 T
Mirror chamber magnets z-position from center	+/- 1.0, 1.025, 1.05, 1.075, 1.10, 1.125, 1.15, 1.175, 1.20, 1.225, 1.25, 1.275 m
Mirror chamber magnets radius	.15 m
Mirror chamber magnetic field	.45 T
Plasma Parameters	
Initial plasma density	10^{13} cm^{-3}
Plasma injection radius	0.02 m
Mass flow injection	6 sccm or $1.8e-7$ kg/s
Energy flow injection	1.29 J/s

Table 5.2: Inputs into the MHD simulation of Emrich GDM experiment.

Table 5.1 lists key parameters of the Emrich experiment. The Emrich experiment, pictured in Figure 5.3, was similar to the typical GDM design with a main chamber capped with two magnetic mirrors. One magnetic mirror end incorporated the gas injection and electron resonance heating capability, while the other magnetic mirror has a vacuum plenum to collect the plasma that passes through the mirror. The plasma is injected and heated in one end and exits out the other end.

Based on the experimental parameters, the MHD simulation inputs were determined. The main chamber has 17 ring magnets, and the magnetic mirror was created with 23 ring magnets. Their exact positions are listed in Table 5.2. The heated plasma was injected at the center of the simulated GDM and allowed to escape out of both magnetic mirrors on either end. Figure 5.4 plots a length-wise slice of the Emrich simulation in its true aspect ratio and a Z-axis at 1/50th scale. The remaining figures are all plotted with the Z-axis at 1/50th scale.

The Emrich test case establishes the capability to model the basic geometry of the GDM field. Flow field results qualitatively match the experiment. The axial

magnetic field generated by the simulation can be seen in Figure 5.4. Steady state operation results in plasma confinement represented by the density contours in Figure 5.5. Figure 5.6 displays the resulting velocity fields of plasma flow out of the magnetic

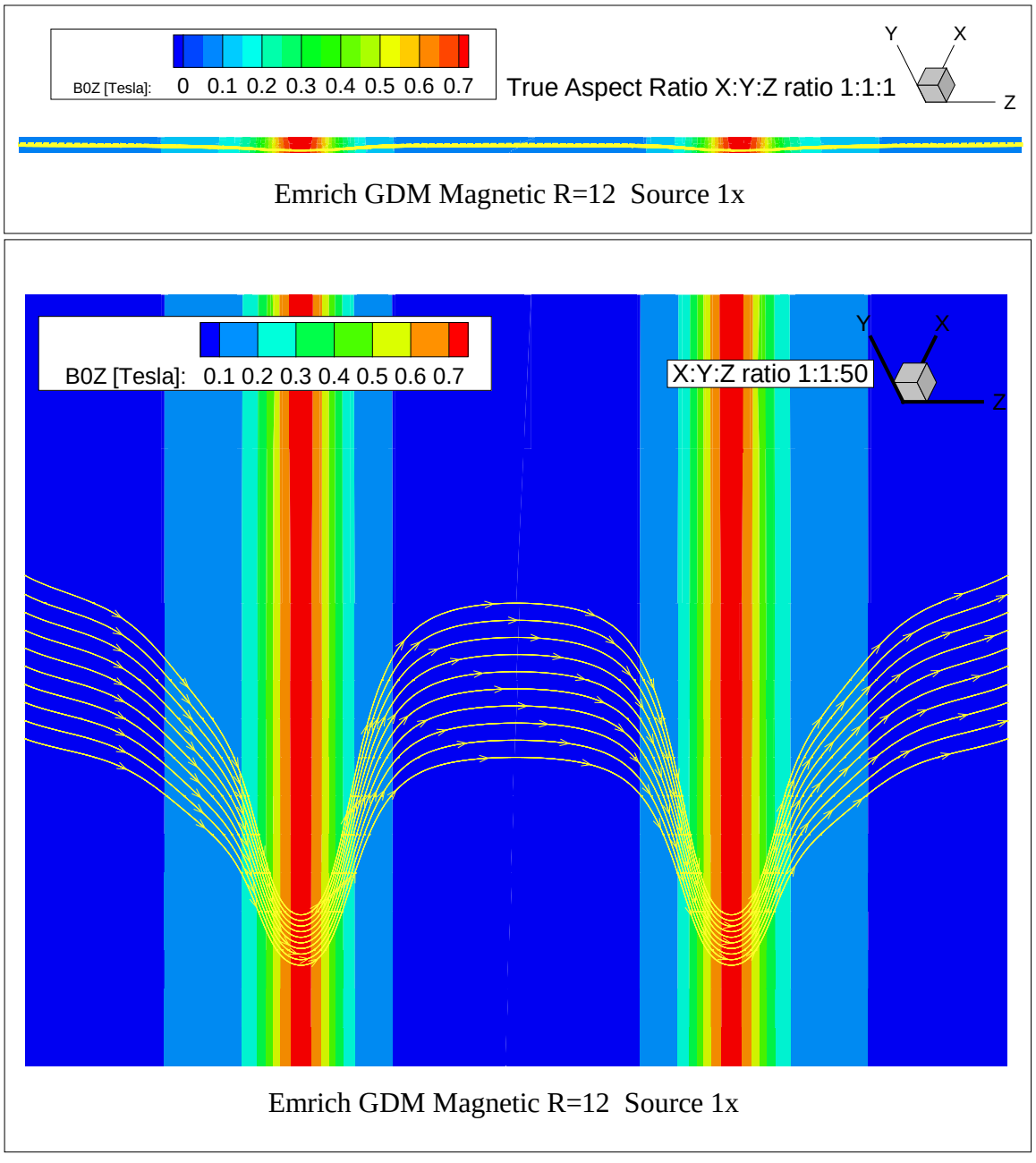

Figure 5.4: Axial component of the magnetic field in the experimental GDM setup presented in true aspect ratio, 1:1:1, and with the Z-axis compressed to 1/50th, 1:1:50.

mirrors.

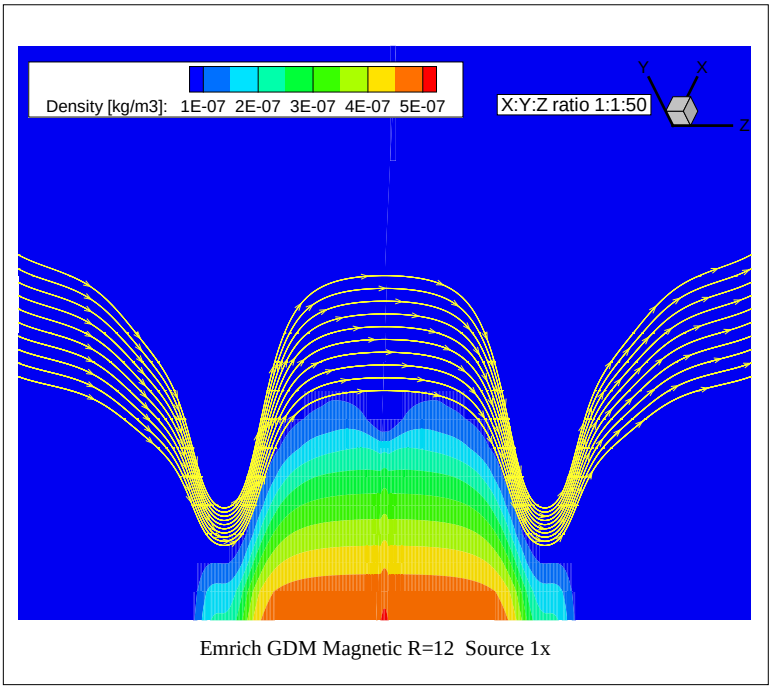

Figure 5.5: Simulation of the density in the experimental GDM setup.

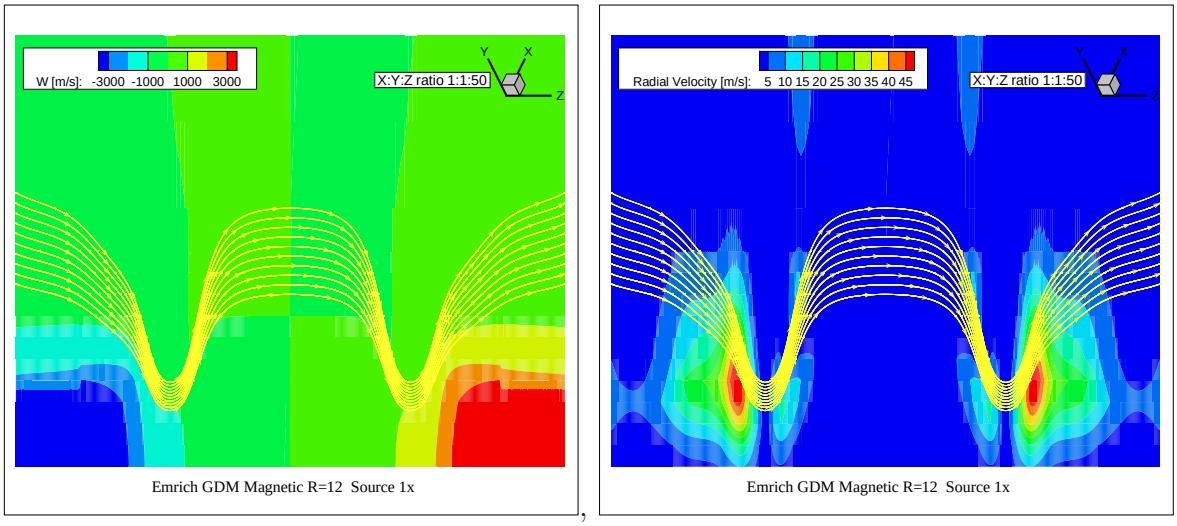

Figure 5.6: Axial and radial velocities in the Emrich experimental GDM setup.

However, the anticipated and initial density of 10^{13} cm^{-3} or 6.63×10^{-7} kg/m^3 is not maintained in the GDM simulation. A number of factors explain why the numerical results have a 10% to 50% lower plasma density. First, the experimental density is estimated from single point measurements. Second, the GDM experiment was a transient, pulsed device designed to produce data on plasma stability, not steady state operating characteristics. As such, it would never be capable of continuous plasma injection and operation similar to the simulated results below. Third, the experimental flow was not bi-directional, but the plasma was generated in one mirror and then exhausted into a vacuum through the other mirror. In contrast, the MHD numerical simulation injects plasma at the center of the GDM and exhausts through both mirrors. This last possibility provides the most likely explanation for the observed differences between experiment and simulation.

5.2.1 GDM Grid Convergence

Grid resolution for GDM configurations is driven by the number of cells across the throat of the magnetic mirror. In the Emrich GDM simulation, as well as in following cases, the initial grid was refined to a minimum of 3 or 4 cells of resolution across the anticipated plasma radius at the center of the throat with similar resolution extending another 2 to 3 radii outwards. Grid convergence was confirmed by adaptively refining a converged case with area of forced refinement in the throat region, doubling the grid resolution in the throat and anywhere in the flow field with significant gradients. Such cases would rapidly reconverge with changes of less than 1%. With some early coarse grids that only had 1 or 2 cells across the plasma radius at the throat, system properties changed by typically 5-10% leading to the rule of thumb of 3-4 cells described above.

5.3 GDM Deuterium-Tritium Simulation

The ultimate goal of this work is to further our understanding of gasdynamic (GDM) mirrors and their potential with a full 3-D computational model. In this vein, a $D-T$ GDM simulation, based on Kammash's original work, was built and run. Energy source terms, both fusion power generation and radiation losses, were required in addition to the base MHD plasma simulation. The case parameters are also more challenging than the Emrich experimental setup, the aspect ratio and the magnetic fields (550 Tesla at the throat, beyond practicality with today's technology) are much greater. These challenges require more computational cells to resolve the system and smaller timesteps due to greater wave speeds. Physically, the larger plasma mass relative to mass flow also means greater relaxation times for the entire system.

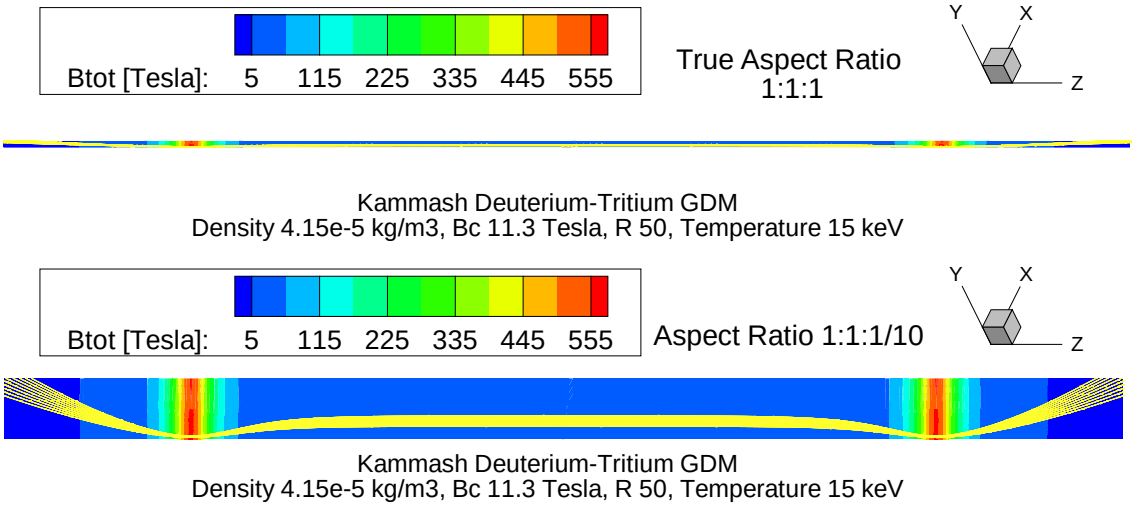

Figure 5.7: Simulation of the Kammash $D-T$ GDM, total magnetic field. True aspect ratio and 1:1:1/10 aspect ratio.

With a plasma radius and throat radius of .07 meters and .01 meters, respectively, along with a length of 32 meters, the aspect ratio is over 3000, without even accounting for plasma expansion in the magnetic nozzles. Figure 5.7 shows a plot of

an axisymmetric radial slice of the GDM in true aspect ratio and with the Z-axis, the lengthwise or axial axis, compressed by a factor of 1/10. The reader should always remember the GDM is long and thin, although all future plots are compressed along the Z-axis by a factor of 150.

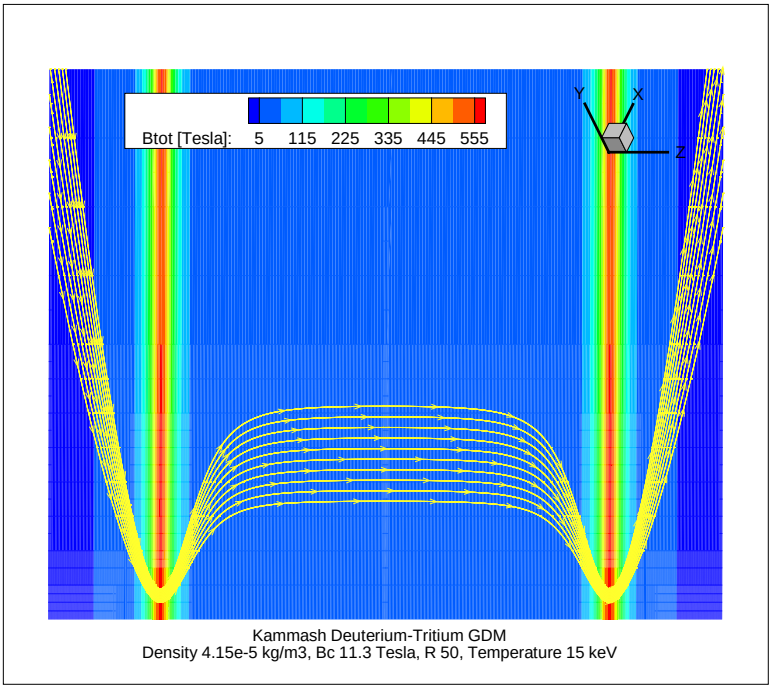

Figure 5.8: Simulation of the Kammash $D-T$ GDM, total magnetic field. Radial slice of axisymmetric field with the centerline at the bottom. Estimated plasma containment surface is at the center of the plotted magnetic streamlines.

Figure 5.8, in a compressed aspect ratio of 1:1:150, is the background magnetic field of the $D-T$ GDM. The desired vacuum magnetic field at the center was 11.3 Tesla. With mirror ratio of 50, the field at the throats is roughly 550 Tesla. The field was numerically integrated based on inputted ring magnets or current coils listed in Table 5.3.

Figures 5.9 and 5.10 give a sense of grid resolution. Remember that the Z-axis is compressed by a factor of 150. Figure 5.9 shows the overall relative grid resolution. Grid refinement was directed at the magnetic throats and in the center at the point

Main chamber magnets number	157
Main chamber magnets	from 15.8 m to -15.8 m
z-position from center	at intervals of .2 m
Main chamber magnets radius	.30 m
Main chamber magnetic field	11.3 T
Mirror chamber magnets number	12 each
Mirror chamber magnets	from +/-15.89 m to +/-16.11 m
z-position from center	at intervals of .02 m
Mirror chamber magnets radius	.30 m
Mirror chamber magnetic field	565 T
Plasma Parameters	
Initial plasma density	10^{16} cm^{-3}
Plasma injection radius	0.07 m
Mass flow injection	1.63×10^{-2} kg/s
Energy flow injection	1.88×10^{10} J/s

Table 5.3: Inputs into MHD simulation of Kammash $D-T$ GDM experiment.

of mass injection. The adaptive refinement algorithm automatically resolved the exit plumes based on the velocity gradients. Figure 5.10 is a closeup of the grid in the containment throat showing at least 5 cell widths across the radius of the throat.

The $D-T$ GDM simulation residual dropped from 1.5×10^{-2} to 3.3^{-5} over 2 million timesteps. However, the pressure and temperature of the system had dropped below the values required to generate enough fusion energy to replace energy losses. Figure 5.11 plots the pressure with the scale's upper limit set to the required pressure, and it is apparent that the system has grown too cold to sustain fusion. Reviewing the unsteady development of the case, the initial conditions fail to produce enough fusion energy to compensate for the radiation losses. The high temperature and high pressure plasma exhausts out of both mirrors, causing the density to drop. At the same time, radiation losses exceed the fusion power generated, causing the plasma to cool and the fusion energy production to drop. Given that the simulation is steady state with larger timesteps in the center than in the mirrors due to wave speed and

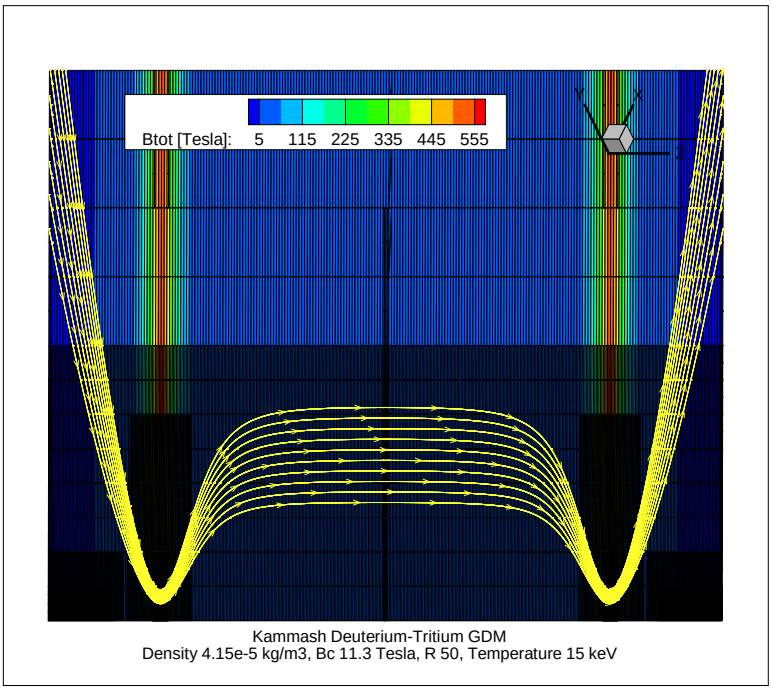

Figure 5.9: Simulation of the Kammash $D-T$ GDM, grid.

cell size limitations, the density drop overshoots equilibrium. The residual bottoms out as the cold injected plasma slowly begins to increase the density within the containment field since the exit mass flow has dropped due to lower pressures and densities; the resulting pattern can be seen in Figure 5.12. In short, the $D-T$ GDM simply failed to ignite.

Examination of the synchrotron power losses in Figure 5.13 suggests the problem. Most notable is the extremely large synchrotron power loss at the throats. This was not accounted for in Kammash's original non-dimensional analytical model. It explains why the simulation does not match the analytical model. The synchrotron losses are directly due to the large magnetic fields. While the magnetic mirrors act similar to a converging and diverging nozzle, they instigate extremely large synchrotron power losses on the exiting plasma. The GDM will at least have to be longer to compensate for the additional power loss. However, the energy loss within

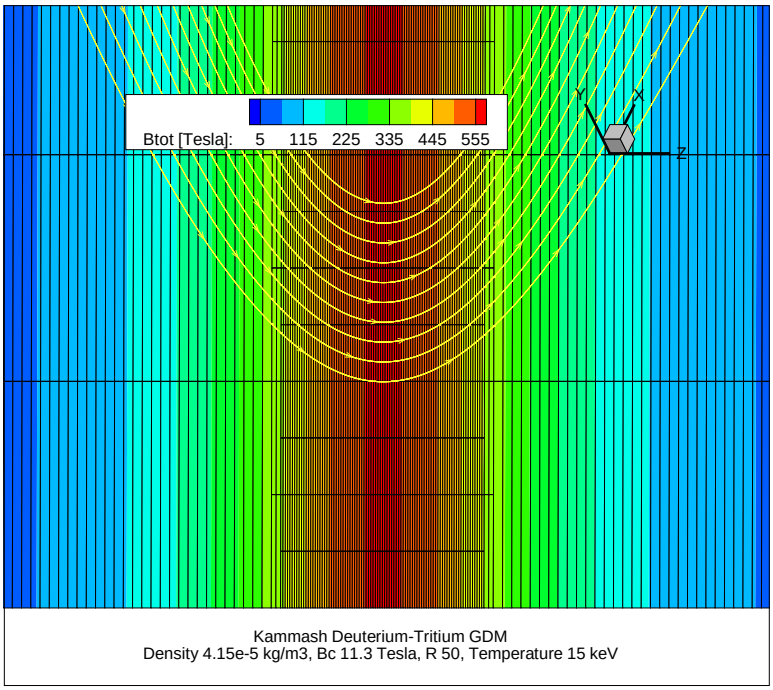

Figure 5.10: Simulation of the Kammash $D-T$ GDM, close-up of grid in throat.

the converging and diverging magnetic nozzle will also impact the exit velocity and specific impulse of exiting plasma. It may also have stability implications for the plasma flow, although none were observed with the ideal MHD simulation.

5.3.1 Computational Performance

The $D-T$ case described had 117,000 computational cells and ran for 2 million time steps with a runtime of roughly 70 days. The runtime was not contiguous, but involved numerous restarts over a 5 month period either due to scheduler termination at the end of the requested run period or due to computer hangup from either a node hardware failure or network failure. A typical parallel job submission was for 168 hours with 16 processes on 8 dual-processor AMD Opteron nodes on the Nyx supercomputer at the University of Michigan, where most nodes are connected with a high-speed commercial gigabit ethernet switch rather than parallel computing optimized Infiniband connections. Under these conditions with local time stepping

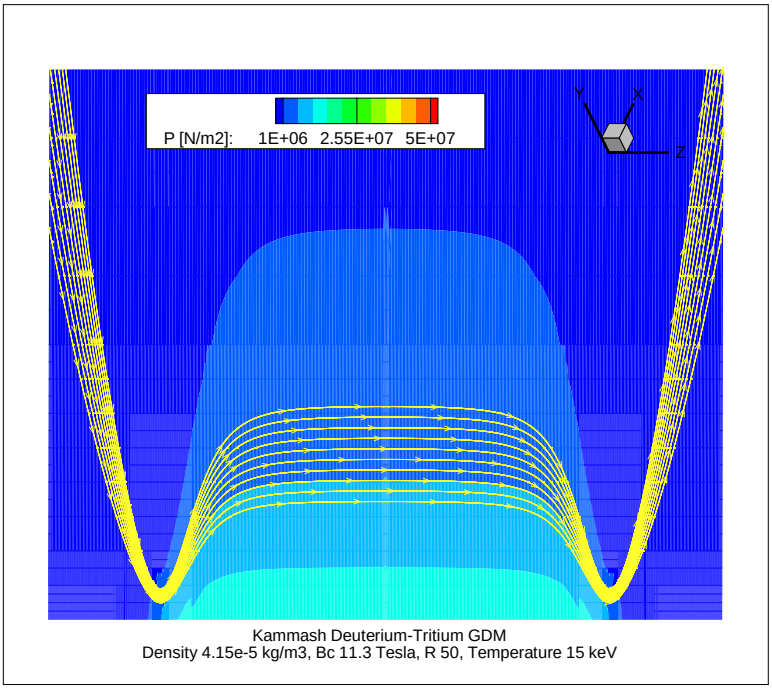

Figure 5.11: Simulation of the Kammash $D-T$ GDM, pressure.

of twice the CFL limit, the simulation would complete one global timestep in about 3 seconds. Each slave process required a little over 300 Mbs of memory, while the master process used just under 400 Mbs of memory. Memory requirements were proportional to the number of cells, with a 858,000 cell refined $D-T$ case requiring just under 3 Gbs of memory per process.

Under the conditions described above, roughly 70% of runtime was involved with generating the implicit system and 30% was required for solving the implicit system. Generating the implicit system involves broadcasting all current cell states to all the processes, calculating all the 8x8 matrix elements based on interfaces and source terms, and assembling those elements into the PETSc matrix, which respectively required 5%, 51%, and 12% of total runtime. Calculation of the matrix elements was coded by the author with matrix block rows of 8, corresponding to the 8 state variables, divided evenly between all processes, which resulted in nearly perfect load

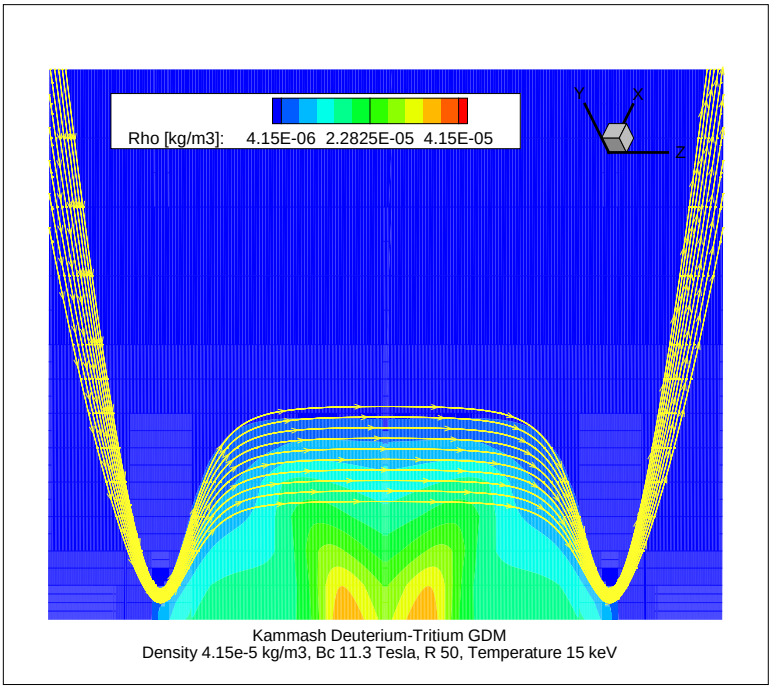

Figure 5.12: Simulation of the Kammash $D-T$ GDM, density.

balancing. Time for calculation of elements was simply proportional to the number of cells divided by the number of processes. Solution of the implicit system was done completely with PETSc routines. Solution time was primarily driven by the multiple of the CFL limit used. As the time step multiple of the CFL limit was increased, the implicit system would become stiffer and require more iterations of the linear solver to reach a time step solution until it would fail to converge. In the $D-T$ case CFL multiples of up to 4 times and in the Emrich case multiples up to 10 times the CFL limit would converge. However, the PETSc solvers require significant amounts of communication in the form of numerous small messages for which the Nyx commercial gigabit ethernet is not optimized for. Whenever time step multiples were increased to near their maximum, the computation time for the implicit solver would dominate performance. The author generally kept the CFL multiples low enough that less than half the runtime was devoted to simply solving

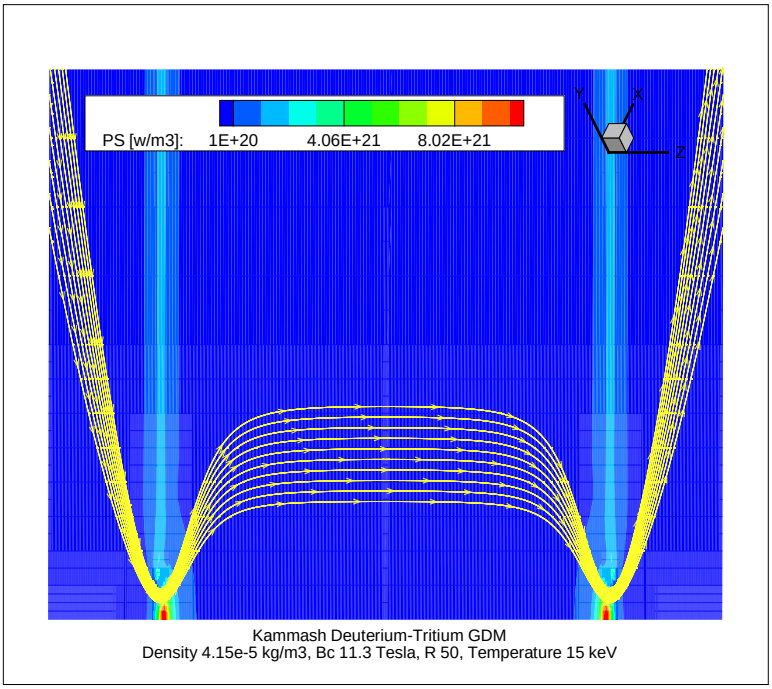

Figure 5.13: Simulation of the Kammash $D-T$ GDM, synchrotron power loss.

the implicit system, which generally corresponded to a less than a dozen iterations of the implicit system solver.

Parallel efficiency on the Nyx platform ranged greatly from roughly .6 to .9, depending primarily on the ratio between work required to generate the implicit system and work required to solve the linear system. As mentioned above, when the CFL multiple was increased, the implicit system became stiffer and the effort required to solve the system increased nonlinearly. Generation of the implicit system requires less communication bandwidth and is near-perfectly load-balanced, resulting in a parallel efficiency greater than .9. Solution of the implicit is more communication-intensive and probably has a parallel efficiency around .6 or .7. The Nyx platform at the University of Michigan uses commercial gigabit ethernet routers providing good, but not great, communication speeds. MHD implicit test cases other than the GDMs were also run on Nyx using either Infiniband nodes or on a single large node

with 8 processors. In both cases, the author saw much higher parallel efficiencies. However, the single node was limited to 8 processes and had memory limitations, and the Infiniband nodes were not generally available.

The large computational runtime for GDM cases are driven by three factors. First, the extremely large magnetic fields create extremely large Alfven wavespeeds, V_a. In the $D-T$ case, V_a is .5% the speed of light in the center of the containment field and over 20% the speed of light in the throat. With corresponding cell lengths on the order of 10 to 1 cm, the CFL limit is extremely restrictive. Second, to address the first issue an implicit algorithm was derived and implemented to allow for timesteps greater than the CFL limit. The implicit algorithm is roughly an order of magnitude more demanding than the explicit algorithm, increasing the computational requirements. Unfortunately, CFL multiples beyond the range of 5-10 produce overly stiff implicit systems that PETSc could not solve. The author suspects that cells inside the throat magnetic field, yet outside the plasma flow with background densities 10-100 times lower, are the source of the implicit system stiffness due to extreme eigenvectors. Third, the physical relaxation time of the GDM systems is large compared with allowable timesteps. In the $D-T$ GDM case the mass flow of the entire plasma column would turn over in roughly 1/1000th of second. A 10% change in total system mass would take 1/10th that, or 1×10^{-4} seconds, based on the extremely optimistic assumption that the mass flow difference is equal to the originally anticipated mass flow rate. In reality, as the system moves toward an equilibrium density, the escaping mass flow rate would approach the injection rate and slow the rate of change in the density. Dividing the relaxation time for a 10% density change with the CFL timestep limit in the throat gives a requirement of 600,000 timesteps. CFL timestep limits in the majority of the GDM simulation

are less restrictive by an order of magnitude or two, and the implicit algorithm is capable of local time stepping at a multiple of the CFL limit. However, the physical relaxation time is likely an order of magnitude or two greater as well. Given this reasoning and the author's experience, converging a GDM case that is off by 10% from initial conditions would require roughly 1 million timesteps to converge.

5.4 Summary

Simulation results from the MHD model presented in Chapter IV were presented. A validation case based on analytical shock polars confirms that the computational code reproduces the ideal MHD systems of equations correctly. A simulation of a non-fusion experimental GDM by Emrich demonstrated that the model is capable of reproducing the physical characteristics of a GDM configuration. Lastly, a simulation of a full $D-T$ Kammash GDM was attempted. While it failed to completely converge, the cause was a failure to ignite. The simulation revealed that the failure to ignite was due to previously unanticipated levels of synchrotron radiation in the magnetic mirrors of the GDM.

CHAPTER VI

CONCLUSIONS

The goal of this body of work was to advance our understanding of gasdynamic mirror (GDM) fusion propulsion systems. Kammash's analytical model [22] suggested that $deuterium-tritium$ ($D-T$) and $deuterium-^3helium$ ($D-^3He$) GDMs were feasible, but they were large at 250 to 100,000 metric tons with up to 75% of the mass accounted for by radiators rather than confinement magnets. Starting from that point, this effort has explored alternate GDM concepts, identified the challenges for modeling GDMs using computational MHD approaches, and found solutions to a number of those challenges.

6.1 Finding 1: Aneutronic fuel $proton-^{11}boron$ is not practical in a self-sustaining GDM

$D-T$ and $D-^3He$ GDMs as proposed by Kammash are limited by neutron and radiation energy losses from the contained fusion plasma before the plasma leaves the magnetic nozzles for propulsion. More exotic aneutronic fusion fuels are often suggested as potential solutions to this problem, but they had never been modeled in a GDM system.

Aneutronic $p-^{11}B$ GDMs were calculated using the same iterative parametric model and shown to be impractical. A temperature of 300 keV was determined

to maximize fusion power relative to bremsstrahlung radiation power losses. With the optimal 300 keV temperature $p-^{11}B$ GDMs were parametrically varied to find the optimal plasma density, fuel ratio, and mirror radius. Both dry mass and trip time were used as measures of effectiveness. Even with advantageous assumptions about synchrotron radiation reflection and positing futuristic non-destructive magnetic technology capable of producing 800 Tesla magnetic fields, the best possible $p-^{11}B$ GDM was over 23 kilometers long, almost 1.3 million metric tonnes, and took over a year and half to reach Mars. The size was driven by the GDM design of a self-sustaining nuclear reactor with more fusion energy out than in, $Q > 1$, combined with the overwhelming bremsstrahlung radiation energy losses from operating at 300 keV.

6.2 Finding 2: Driven GDMs offer some benefits

Finding 1 suggests that simply invoking exotic advanced fusion fuels of the aneutronic variety with the necessary futuristic technologies will not make the original self-sustaining GDM concept more viable. In reality, higher fusion temperatures will aggravate the problem of radiation losses. An alternate approach for improving the viability of GDMs are driven GDMs. They did not achieve a self-sustaining nuclear fusion reaction, but are driven by nuclear electric power supplies.

The iterative analytical model was extended to model GDMs driven by external nuclear fission power sources. The power balance equation for Q that produces the target Q of 1.22 for GDMs was modified to account for some fraction of externally provided power from a nuclear electric reactor. As the external power generated is increased, the required Q decreases. Q values less than 1.22 require shorter fusion plasma confinement times, and the GDM length and mass decrease correspondingly.

When this approach was applied to the optimal $p-^{11}B$ GDM with a 300 keV temperature, the driven system had a reduced length of 5000 meters. The specific power of the nuclear electric systems were comparable to that of the $p-^{11}B$ GDM. While length was reduced, performance remained relatively constant. To examine a less technologically demanding system, a $p-^{11}B$ GDM operating at only 160 keV and driven by a nuclear electric system was modeled parametrically. Without nuclear electric assistance, the 160 keV $p-^{11}B$ GDM performed far worse than the optimal 300 keV system, as would be expected with a higher proportion of radiation losses relative to fusion power produced. As the nuclear electric power increases as fraction of the fusion power, the performance of the driven non-optimal 160 keV $p-^{11}B$ system approaches the performance of the original 300 keV system. By considering driven GDM systems, you can lower the fusion temperatures and associated technology requirements. Nonetheless, $p-^{11}B$ GDMs are still not practical, having masses on the order of a million metric tonnes.

The new driven-GDM parametric model was also applied to the more viable $D-T$ GDM. In this case, the specific power of the $D-T$ GDM is higher than that of the nuclear electric reactors. Increasing the fraction of power generated by the nuclear electric reactors decreases system performance in terms of both greater dry mass and longer trip times. When the nuclear electric reactors are producing as much power as the fusion GDM, the system is four times heavier and requires more than twice the time to reach Mars. While the driven systems are not preferable to the original $D-T$ GDM concept, it does demonstrate that there is a viable development path from non-fusion plasma rockets to breakeven self-sustaining GDM rockets.

6.3 Finding 3: Challenges for computational MHD modeling of GDMs include an extreme aspect ratio, massive background magnetic fields, large numerical wave speeds, and traveling waves

In order to explore GDM concepts that are between a non-nuclear plasma rocket and full self-sustaining GDM, a three-dimensional magnetohydrodynamic (MHD) computational modeling effort was initiated. In modeling GDM systems, a number of challenges were identified, including the large aspect ratio, the extreme magnetic fields, numerical wave speeds that are time-step limiting, and traveling waves between the magnetic mirrors. These challenges are described here, while the next finding describes the solutions implemented.

The GDM concept is a long thin plasma column with magnetic mirrors at both ends. The plasma column radius is a few centimeters in the center and can be less than one centimeter in the throat, while the length of the GDM plasmas start at 10 meters and extend to 100s, even 1000s, of meters. The MHD simulation needs to resolve the flow to the millimeter scale in the radial direction while spanning the 10s to 1000s of meters in the axial direction.

In the MHD system of equations, both the momentum and energy conservation equations include terms that incorporate both the fluid dynamic and magnetic pressures. When the magnetic field is extremely intense, the magnetic pressure or even the numerical errors in calculating the magnetic pressure terms can overwhelm the fluid dynamic pressure. The GDM concepts have magnetic fields that range from 10 Tesla to many 100s of Tesla. While the gasdynamic and magnetic pressure ratio, β, may approach unity at the center of the GDM plasma column, at the radial edge of the plasma column, the gasdynamic pressure drops towards the vacuum of space,

and either magnetic mirror can have a mirror ratio that increases the magnetic field strength by two orders of magnitude. As such, there are parts of the simulation, especially just outside the plasma column within the magnetic mirrors, where the magnetic field is many orders of magnitude greater than the fluid dynamic pressure. Since the fluid dynamic flow in the throats happens to be an important factor in plasma containment and exhaust velocities, the great difference in magnetic and gasdynamic pressure needs to be addressed in GDM simulations.

Fundamental to the stability of a numerical scheme are the wave speeds. In an explicit finite volume scheme, stability dictates that the timestep is limited in order to keep the numerical waves from crossing other numerical interfaces. The MHD system has seven wave speeds including the Alfven wave, B/ρ. Again, the GDM concept has extremely large magnetic fields and the density drops off to the vacuum of space as you move radially out of the plasma column. This results in Alfven wave speeds that are a few percent of the speed of light in the magnetic mirrors where the required resolution drops down to fractions of a centimeter. The resulting timestep limitations are severe and need to be addressed.

Lastly, the long thin plasma column of the GDM trapped between two magnetic mirrors is physically similar to a shock tube. Any disturbance, whether from initial conditions or a numerical artifact, creates a traveling wave along the plasma column. As the wave travels into the magnetic mirror, part of it will pass through the magnetic nozzle and out through the simulation boundary, but part of the wave will be reflected and again travel the length of the GDM system. Numerical viscosity will have a dampening effect on the smaller numerical waves, but physical waves, such as having magnetic mirrors of different strengths at either end, require that the information must be communicated from end to end of the simulation. Given the length of

the GDMs and correspondingly large number of cells with the timestep limitations previously mentioned, these traveling waves demand significant additional computer run time unless otherwise addressed.

6.4 Finding 4: Solutions to numerical challenges

In developing the MHD simulation of a GDM, the author addressed the four challenges identified in the previous finding. The solutions are detailed throughout Chapter IV, and are briefly reviewed here.

To address the aspect ratio of the GDM system, a stretched mapping was introduced into the Cartesian grid representation. A Cartesian gridding approach typically uses cubic cells to subdivide the domain. In this MHD simulation of a GDM, a stretch mapping allows for easy adjustment of the X to Y to Z ratio. In this work, the Z dimension, which was along the axis of the GDM, was generally set to be 10 times greater than the X and Y dimensions. This effectively reduces the computational load by an order of magnitude. Areas that require axial resolution, such as the throats and mass source injection, were simply refined further using adaptive refinement capabilities. Reducing the number of cells along the length of the GDM also helps mitigate the traveling wave problem, but it does not eliminate it.

A solution for simulating the massive magnetic fields of the GDM, a split magnetic field approach developed by Powell[34], was implemented. This separates the constant background magnetic field from a fluctuating magnetic field induced by the MHD flow. Given that the fluctuating magnetic field is much smaller than the background field, this very nicely removes excessive errors introduced by large magnetic pressure terms. It should be noted that this does not affect the MHD wave speeds,

since the full magnetic field is still represented in the MHD system of equations, just split into a constant part and a fluctuating part. Therefore, this split magnetic field approach does not address the wave speed/timestep challenge.

In order to compensate for the short timesteps of an explicit approach, a fully implicit version of the MHD equations with a split magnetic field was derived and implemented. The implicit scheme greatly increases the computational demand, since a linear system of equations then needs to be solved. The MHD simulation was parallelized and the PETSc library used to meet this additional demand. Unfortunately, timesteps greater than roughly 10 times the CFL limit result in numerical instability due to the stiffness in the implicit system from the large range of wave speeds. Since the parallelized approach can meet the increased computational demands, the expanded timestep decreases the time to a solution by an order of magnitude. The fully implicit approach also addresses the traveling wave issue, since information from one end of the GDM can be transmitted to the other end of the GDM each timestep through the implicit linear system.

6.5 Finding 5: Physical challenges to full 3-D numerical MHD models of GDMs including additional sources of significant energy loss remain

The 3-D implicit algorithm proved capable of simulating the GDM plasma flows, fusion energy generation, and power losses, but the computational demand was still too much to do system studies. However, it did provide insight into the plasma flow inside the GDM throat, showing synchrotron energy losses that are not accounted for in the parametric model.

In addition to the challenges addressed previously, two fundamental physical limitations remain that demand excessive computational resources. First, as with any

steady state computational solution, the rate of change in the solution decreases as you approach a steady state. In the GDM system this is aggravated by its configuration. The difference between the injection mass source and the loss of plasma through the magnetic mirrors determines whether the density of the whole plasma column is increasing or decreasing. While the implicit scheme helps transmit that information throughout the simulation, it still takes many timesteps to achieve an equilibrium. The simplest solution is to set the initial conditions to an accurate estimate of the steady state solution in order to limit the systemic relaxation time required.

Using the analytic model to set the initial conditions was attempted. However, MHD GDM simulations demonstrated a second fundamental physical limitation not previously anticipated, namely, that the increased magnetic fields at the throat produce significant unanticipated radiation losses. Given that the synchrotron radiation is proportional to B^2, a mirror ratio of 100 means that synchrotron radiation losses at the mirror are 10,000 times greater per unit volume than in the majority of the plasma column. If the throat accounts for only a tenth of one percent of the total length, synchrotron radiation from the mirrors would be double the synchrotron emission anticipated by the parametric model.

While this does not necessarily invalidate the analytic model or the GDM concept, it does suggest that the parametric model underestimates the length of the GDM system. Unfortunately, if the GDM being simulated is not long enough, then breakeven is not achieved and the fusion reaction is not self-sustaining. The plasma will simply continue to cool and devolve into an unheated plasma rocket. Without a more accurate estimate for the initial conditions and length of the GDM, the computing power requirements for full 3-D MHD simulation remain excessive and

unpredictable.

6.6 Future Work

While a 3-D MHD model of a GDM has been demonstrated, the computational demand makes it impractical as a design tool. Key to improving its convergence is an accurate estimate of the system properties for initial conditions. The next step in modeling GDM systems is to develop a 1-D numerical model. In such a model, plasma radius and synchrotron radiation losses would be a function of the magnetic field strength at the centerline. Mass, momentum, and energy fluxes could be iteratively integrated along the length of the GDM to determine the steady state properties of the GDM. These estimates could then be used as initial conditions for the full 3-D ideal MHD model of a GDM.

Along the lines of 3-D simulations with only one grid cell across the magnetic throat's radius, such a 1-D model will likely be off by at least 5-10%. A 2-D model that is integrated both axially and radially would provide an even more accurate estimate for input into a 3-D model as initial conditions. In the case of axisymmetric GDMs, such as those discussed in this work, a 2-D model would likely be just as accurate as the 3-D model. However, numerous non-axisymmetric magnetic mirror concepts exist, particularly ones that address bad curvature instability issues explored by Emrich, so there remains a need for 3-D simulations of GDMs.

Regardless, the full 3-D MHD simulation of a GDM is so computationally demanding that even if computational resources were available, it would be inefficient to model the whole GDM in 3-D given the extreme aspect ratio of the system. The author anticipates that a hybrid 1-D and 3-D simulation would be the most efficient solution. The full 3-D MHD simulation described here can be applied to key sec-

tions of the GDM, such as the magnetic nozzles or energy/mass injection areas. The boundary conditions of these much smaller 3-D simulations would be derived from the solution of a 1-D model representing the GDM's long plasma column. The 1-D model would allow information to travel much more quickly along the GDM column between the more complicated sections of the GDM modeled with the 3-D MHD model. Such a scheme would make further system design studies of a GDM possible.

With reference to the 3-D MHD model only, there remain a number of possibilities for improvement. Obviously, porting the code to an order-of-magnitude more powerful supercomputer would produce estimated runtimes of a few weeks, which is almost practical. A supercomputer with improved communications bandwidth and particularly latency would also give better parallel efficiency and scaling. Using unstructured Cartesian grids produces a sparse, but unstructured, implicit system; using a structured grid for the implicit system would open the door to numerous linear solvers that are more efficient on parallel systems. Another possibility is to remove cells in the GDM throat's magnetic field but outside the plasma flow by creating an unphysical geometry to occupy the volume. This may remove stiffness from the implicit system and allow for higher multiples of CFL limit to be achieved. Lastly, further validation of the complete MHD physics model including the energy source terms could be explored. Experiments with gasdynamic traps studied at the Budker Institute of Nuclear Physics in Novosibirsk might provide a suitable validation case.

APPENDICES

APPENDIX A

Ideal MHD Roe Approximate Rieman Solver Eigenvectors

Below are the matrices that compose the Roe approximate Riemann solver flux function,

$$\mathbf{F}(\mathbf{U}_L, \mathbf{U}_R) = \frac{1}{2}\left(\mathbf{A}_L\mathbf{U}_L + \mathbf{A}_R\mathbf{U}_R\right) - \frac{1}{2}\mathbf{L}|\mathbf{\Lambda}|\mathbf{R}(\mathbf{U}_R - \mathbf{U}_L), \tag{A.1}$$

referenced in Chapter IV

$$|\mathbf{\Lambda}| = (u, u, u + \frac{B_x}{\rho}, u - \frac{B_x}{\rho}, u + c_f, u - c_f, u + c_s, u - c_s)^T \tag{A.2}$$

$$\mathbf{A} = \begin{bmatrix} 0 & 1 & 0 & 0 & 0 & 0 & 0 & 0 \\ -u^2+\frac{q^2}{2}(\gamma-1) & -u(\gamma-3) & -v(\gamma-1) & -w(\gamma-1) & -B_x(\gamma-1) & -B_y(\gamma-2) & -B_z(\gamma-2) & \gamma-1 \\ -uv & v & u & 0 & 0 & -B_x & 0 & 0 \\ -uw & w & 0 & u & 0 & 0 & -B_x & 0 \\ 0 & 0 & 0 & 0 & u & 0 & 0 & 0 \\ \frac{vB_x-uB_y}{\rho} & B_y/\rho & -B_x/\rho & 0 & 0 & u & 0 & 0 \\ \frac{wB_x-uB_z}{\rho} & B_z/\rho & 0 & -B_x/\rho & 0 & 0 & u & 0 \\ \frac{B_x(vB_y+wB_z)}{\rho}+ & & & & & & & \\ u(\frac{q^2}{2}(\gamma-2)- & \frac{q^2}{2}-u^2(\gamma-1)- & -\frac{B_xB_y}{\rho}- & -\frac{B_xB_z}{\rho}- & -u(\gamma-1)B_x & -vB_x- & -wB_x- & u\gamma \\ \frac{\gamma}{\gamma-1}\frac{p}{\rho}-\frac{B_y^2+B_z^2}{\rho}) & \frac{\gamma}{\gamma-1}\frac{p}{\rho}-\frac{B_y^2+B_z^2}{\rho} & uv(\gamma-1) & uw(\gamma-1) & & u(\gamma-2)B_y & u(\gamma-2)B_z & \end{bmatrix} \tag{A.3}$$

$$\mathbf{L} = \begin{bmatrix} 1-\frac{q^2(\gamma-1)}{2a^2} & \frac{u(\gamma-1)}{a^2} & \frac{v(\gamma-1)}{a^2} & \frac{w(\gamma-1)}{a^2} & \frac{B_x(\gamma-1)}{a^2} & \frac{B_y(\gamma-1)}{a^2} & \frac{B_z(\gamma-1)}{a^2} & \frac{-(\gamma-1)}{a^2} \\ 0 & 0 & 0 & 0 & 1 & 0 & 0 & 0 \\ \frac{-w\beta_y+v\beta_z}{\sqrt{2}\rho} & 0 & -\frac{\beta_z}{\sqrt{2}\rho} & \frac{\beta_z}{\sqrt{2}\rho} & 0 & -\frac{\beta_z}{\sqrt{2}\rho} & \frac{\beta_z}{\sqrt{2}\rho} & 0 \\ \frac{-w\beta_y+v\beta_z}{\sqrt{2}\rho} & 0 & -\frac{\beta_z}{\sqrt{2}\rho} & \frac{\beta_z}{\sqrt{2}\rho} & 0 & \frac{\beta_z}{\sqrt{2}\rho} & -\frac{\beta_z}{\sqrt{2}\rho} & 0 \\ \frac{2q^2(\gamma-1)\alpha_s+uc_s\alpha_s+sgn(B_x)c_f\alpha_f(v\beta_y+w\beta_z)}{2a^2\rho} & \frac{(-u(\gamma-1)+c_s)\alpha_s}{2a^2\rho} & \frac{-v(\gamma-1)\alpha_s+sgn(B_x)c_f\alpha_f\beta_y}{2a^2\rho} & \frac{-w(\gamma-1)\alpha_s+sgn(B_x)c_f\alpha_f\beta_z}{2a^2\rho} & \frac{-B_x(\gamma-1)\alpha_s}{2a^2\rho} & \frac{-B_y(\gamma-1)\alpha_s}{2a^2\rho}-\frac{\alpha_f\beta_y}{2a\sqrt{\rho}} & \frac{-B_z(\gamma-1)\alpha_s}{2a^2\rho}-\frac{\alpha_f\beta_z}{2a\sqrt{\rho}} & \frac{(\gamma-1)\alpha_s}{2a^2\rho} \\ \frac{2q^2(\gamma-1)\alpha_s-uc_s\alpha_s-sgn(B_x)c_f\alpha_f(v\beta_y+w\beta_z)}{2a^2\rho} & \frac{(-u(\gamma-1)+c_s)\alpha_s}{2a^2\rho} & \frac{-v(\gamma-1)\alpha_s+sgn(B_x)c_f\alpha_f\beta_y}{2a^2\rho} & \frac{-w(\gamma-1)\alpha_s+sgn(B_x)c_f\alpha_f\beta_z}{2a^2\rho} & \frac{-B_x(\gamma-1)\alpha_s}{2a^2\rho} & \frac{-B_y(\gamma-1)\alpha_s}{2a^2\rho}-\frac{\alpha_f\beta_y}{2a\sqrt{\rho}} & \frac{-B_z(\gamma-1)\alpha_s}{2a^2\rho}-\frac{\alpha_f\beta_z}{2a\sqrt{\rho}} & \frac{(\gamma-1)\alpha_s}{2a^2\rho} \\ \frac{2q^2(\gamma-1)\alpha_f+uc_f\alpha_f-sgn(B_x)c_s\alpha_s(v\beta_y+w\beta_z)}{2a^2\rho} & \frac{(-u(\gamma-1)+c_f)\alpha_f}{2a^2\rho} & \frac{-v(\gamma-1)\alpha_f+sgn(B_x)c_s\alpha_s\beta_y}{2a^2\rho} & \frac{-w(\gamma-1)\alpha_f+sgn(B_x)c_s\alpha_s\beta_z}{2a^2\rho} & \frac{-B_x(\gamma-1)\alpha_f}{2a^2\rho} & \frac{-B_y(\gamma-1)\alpha_f}{2a^2\rho}+\frac{\alpha_s\beta_y}{2a\sqrt{\rho}} & \frac{-B_z(\gamma-1)\alpha_f}{2a^2\rho}+\frac{\alpha_s\beta_z}{2a\sqrt{\rho}} & \frac{(\gamma-1)\alpha_f}{2a^2\rho} \\ \frac{2q^2(\gamma-1)\alpha_f-uc_f\alpha_f+sgn(B_x)c_s\alpha_s(v\beta_y+w\beta_z)}{2a^2\rho} & \frac{(-u(\gamma-1)+c_f)\alpha_f}{2a^2\rho} & \frac{-v(\gamma-1)\alpha_f+sgn(B_x)c_s\alpha_s\beta_y}{2a^2\rho} & \frac{-w(\gamma-1)\alpha_f+sgn(B_x)c_s\alpha_s\beta_z}{2a^2\rho} & \frac{-B_x(\gamma-1)\alpha_f}{2a^2\rho} & \frac{-B_y(\gamma-1)\alpha_f}{2a^2\rho}+\frac{\alpha_s\beta_y}{2a\sqrt{\rho}} & \frac{-B_z(\gamma-1)\alpha_f}{2a^2\rho}+\frac{\alpha_s\beta_z}{2a\sqrt{\rho}} & \frac{(\gamma-1)\alpha_f}{2a^2\rho} \end{bmatrix} \tag{A.4}$$

$$\mathbf{R} = \begin{bmatrix}
1 & 0 & 0 & 0 & \rho\alpha_s \\
u & 0 & 0 & 0 & \rho(u-c_s)\alpha_s \\
v & 0 & \frac{-\rho\beta_z}{\sqrt{2}} & \frac{-\rho\beta_z}{\sqrt{2}} & v\rho\alpha_s - sgn(B_x)\rho c_f\alpha_f\beta_y \\
w & 0 & \frac{\rho\beta_y}{\sqrt{2}} & \frac{\rho\beta_y}{\sqrt{2}} & v\rho\alpha_s - sgn(B_x)\rho c_f\alpha_f\beta_z \\
0 & 1 & 0 & 0 & 0 \\
0 & 0 & \frac{-\rho\beta_z}{\sqrt{2}} & \frac{-\rho\beta_z}{\sqrt{2}} & \sqrt{p\gamma}\alpha_f\beta_y \\
0 & 0 & \frac{\rho\beta_y}{\sqrt{2}} & \frac{\rho\beta_y}{\sqrt{2}} & \sqrt{p\gamma}\alpha_f\beta_z \\
\frac{q^2}{2} & B_x & \frac{\rho(w\beta_y - v\beta_z)}{\sqrt{2}} & \frac{\rho(w\beta_y - v\beta_z)}{\sqrt{2}} & (\frac{\gamma p}{\gamma-1} + \rho(\frac{q^2}{2} - uc_s))\alpha_s + (\sqrt{p\gamma(B_y^2+B_z^2)} - sgn(B_x)\rho c_f(v\beta_y + w\beta_z))\alpha_f
\end{bmatrix}$$

$$\begin{bmatrix}
\rho\alpha_s & \rho\alpha_f & \rho\alpha_f \\
\rho(u+c_s)\alpha_s & \rho(u-c_f)\alpha_f & \rho(u+c_f)\alpha_f \\
v\rho\alpha_s + sgn(B_x)\rho c_f\alpha_f\beta_y & v\rho\alpha_f + sgn(B_x)\rho c_s\alpha_s\beta_y & v\rho\alpha_f - sgn(B_x)\rho c_s\alpha_s\beta_y \\
v\rho\alpha_s + sgn(B_x)\rho c_f\alpha_f\beta_z & v\rho\alpha_f + sgn(B_x)\rho c_s\alpha_s\beta_z & v\rho\alpha_f - sgn(B_x)\rho c_s\alpha_s\beta_z \\
0 & 0 & 0 \\
\sqrt{p\gamma}\alpha_f\beta_y & -\sqrt{p\gamma}\alpha_s\beta_y & -\sqrt{p\gamma}\alpha_s\beta_y \\
\sqrt{p\gamma}\alpha_f\beta_z & -\sqrt{p\gamma}\alpha_s\beta_z & -\sqrt{p\gamma}\alpha_s\beta_z \\
(\frac{\gamma p}{\gamma-1} + \rho(\frac{q^2}{2} + uc_s))\alpha_s & (\frac{\gamma p}{\gamma-1} + \rho(\frac{q^2}{2} - uc_f))\alpha_f & (\frac{\gamma p}{\gamma-1} + \rho(\frac{q^2}{2} + uc_f))\alpha_f \\
+(\sqrt{p\gamma(B_y^2+B_z^2)} + sgn(B_x)\rho c_f(v\beta_y + w\beta_z))\alpha_f & +(\sqrt{-p\gamma(B_y^2+B_z^2)} + sgn(B_x)\rho c_s(v\beta_y + w\beta_z))\alpha_s & +(\sqrt{-p\gamma(B_y^2+B_z^2)} - sgn(B_x)\rho c_s(v\beta_y + w\beta_z))\alpha_s
\end{bmatrix} \quad \text{(A.5)}$$

APPENDIX B

Split Magnetic Field Flux Terms and Derivatives

When the ideal MHD equations are split between a constant background magnetic field and fluctuating component, there are additional fluxes to account for the background field. This flux vector, $\mathbf{G}_x$, and its derivative mentioned in Chapter IV Sections 4.3.4, 4.4, and 4.5 are listed below.

$$\mathbf{G}_x = \begin{pmatrix} 0 \\ \mathbf{B}_0 \cdot \mathbf{B}_1 - 2B_{0x}B_{1x} \\ -B_{0y}B_{1x} - B_{1y}B_{0x} \\ -B_{0z}B_{1x} - B_{1z}B_{0x} \\ 0 \\ vB_{0x} - B_{0y}u \\ wB_{0x} - B_{0z}u \\ (\mathbf{B}_0 \cdot \mathbf{B}_1)\, u - (\mathbf{u} \cdot \mathbf{B}_1)\, B_{0x} \end{pmatrix} \tag{B.1}$$

$$\frac{\partial \mathbf{G}_x}{\partial \mathbf{U}} = \begin{bmatrix} 0 & 0 & 0 & 0 \\ 0 & 0 & 0 & 0 \\ 0 & 0 & 0 & 0 \\ 0 & 0 & 0 & 0 \\ 0 & 0 & 0 & 0 \\ \frac{vB_{0x}+B_{0y}u}{\rho} & \frac{-B_{0y}}{\rho} & \frac{B_{0x}}{\rho} & 0 \\ \frac{wB_{0x}+B_{0z}u}{\rho} & \frac{-B_{0z}}{\rho} & 0 & \frac{B_{0x}}{\rho} \\ \frac{-(\mathbf{B}_0\cdot\mathbf{B}_1)u+(\mathbf{u}\cdot\mathbf{B}_1)B_{0x}}{\rho} & \frac{(\mathbf{B}_0\cdot\mathbf{B}_1)-B_{1x}B_{0x}}{\rho} & -\frac{B_{1y}B_{0x}}{\rho} & -\frac{B_{1z}B_{0x}}{\rho} \end{bmatrix}$$

$$\begin{bmatrix} 0 & 0 & 0 & 0 \\ -B_{0x} & B_{0y} & B_{0z} & 0 \\ -B_{0y} & -B_{0x} & 0 & 0 \\ -B_{0z} & 0 & -B_{0x} & 0 \\ 0 & 0 & 0 & 0 \\ 0 & 0 & 0 & 0 \\ 0 & 0 & 0 & 0 \\ 0 & B_{0y}u - vB_{0x} & B_{0z}u - wB_{0x} & 0 \end{bmatrix} \tag{B.2}$$

BIBLIOGRAPHY

BIBLIOGRAPHY

[1] Altseimer, J. H., Mader, G. F., and Sterwart, J. J. Operating characteristics and requirements for the NERVA flight engine. *Journal of Spacecraft and Rockets 8*, 7 (1971), 766–773.

[2] Baldwin, D. E. End-loss processes from mirror machines. *Rev. Mod. Phys. 49*, 2 (1977), 317–339.

[3] Bayyuk, S., Powell, K., and van Leer, B. A simulation technique for 2-D unsteady inviscid flows around arbitrarily moving and deforming bodies of arbitrary geometry. AIAA Paper 93-3391-CP, 1993.

[4] Bayyuk, S., Powell, K., and van Leer, B. Computation of flows with moving boundaries and fluid-structure interactions. In *13th AIAA Computational Fluid Dynamics Conference* (1997). AIAA Paper 97-1771.

[5] Best, R. W. Advanced fusion fuel cycles. *Fusion Technology 17* (1990), 661–665.

[6] Brackbill, J. U., and Barnes, D. C. The effect of nonzero $\nabla \cdot \mathbf{b}$ on the numerical solution of the magnetohydrodynamic equations. *Journal of Computational Physics 35* (1980), 426–430.

[7] Cassady, L. D., Longmier, B. W., Olsen, C. S., Ballenger, M. G., McCaskill, G. E., Ilin, A. V., Carter, M. D., Glover, T. W., Squire, J. P., and Chang Díaz, F. R. VASIMR performance results. In *46th AIAA/ASME/SAE/ASEE Joint Propulsion Conference and Exhibit* (2010). AIAA Paper 2010-6772.

[8] Chang Díaz, F. R. The VASIMR rocket. *Scientific American* (November 2000), 90–97.

[9] Charlton, E. F. *An Octree Solution to Conservation-laws over Arbitrary Regions (OSCAR) with Applications to Aircraft Aerodynamics.* PhD thesis, The University of Michigan, 1997.

[10] Cho, H., and et al. Recent progress in the gamma 10 tandem mirror. *Transactions of Fusion Science and Technology 47*, 1T (2005), 9–16.

[11] Dawson, J. M. Advanced fusion reactors. In *Fusion*, Teller, Ed., vol. 1: Part B. Academic Press, New York, 1981, pp. 453–501.

[12] De Zeeuw, D. L. *A Quadtree-Based Adaptively Refined Cartesian Grid Algorithm for Solution of the Euler Equations*. PhD thesis, The University of Michigan, 1993.

[13] De Zeeuw, D. L., Gombosi, T., Groth, C., Powell, K., and Stout, Q. An adaptive MHD method for global space weather simulations. *IEEE Transactions on Plasma Science 28* (2000), 1956–1965.

[14] Drake, B. G., Ed. *Human Exploration of Mars Design Reference Architecture 5.0*. NASA/SP-2009-566. NASA, 2009.

[15] Emrich, W. J. *Plasma Stability Studies of the Gasdynamic Mirror Fusion Propulsion Experiment*. PhD thesis, The University of Alabama in Huntsville, 2003.

[16] Emrich, W. J., and Hawk, C. W. Magnetohydrodynamic instabilities in a simple gasdynamic mirror propulsion system. *Journal of Propulsion and Power 21*, 3 (2005), 401–407.

[17] Fowler, T. K. Mirror theory. In *Fusion*, Teller, Ed., vol. 1: Part A. Academic Press, New York, 1981, pp. 291–355.

[18] Godunov, S. K. Symmetric form of the equations of magnetohydrodynamics. *Numerical Methods for Mechanics of Continuum Medium 1* (1972), 26–34.

[19] Heindler, M., and Kernbichler, W. Advance fuel fusion. In *Proceedings of the Fifth International Conference on Emerging Nuclear Energy Systems* (1989), pp. 177–82.

[20] Ivanov, A. A., Anikeev, A. V., Bagryansky, P. A., Bocharov, V. N., Deichuli, P. P., Karpushov, A. N., Maximov, V. V., Pod'minogin, A. A., Rogozin, A. I., Salikova, T. V., and Tsidulko, Y. A. Experimental study of curvature-driven flute instability in the gas-dynamic trap. *Physics of Plasmas 1*, 5 (1994), 1529–1535.

[21] Kammash, T., and Galbraith, D. L. Improved physics model for the gasdynamic fusion propulsion system. *Journal of Propulsion and Power 14*, 1 (1998), 24–8.

[22] Kammash, T., and Lee, M. J. Gasdynamic fusion propulsion system for space exploration. *Journal of Propulsion and Power 11*, 3 (1995), 544–53.

[23] Kammash, T., Lee, M. J., and Poston, D. I. High-thrust high-specific impulse gasdynamic fusion propulsion system. *Journal of Propulsion and Power 13*, 3 (1997), 421–7.

[24] Kammash, T., and Poston, D. I. A computational model for an open-cycle gas core nuclear rocket. *Nuclear Science and Engineering 122*, 1 (1996), 32.

[25] Kernbichler, W., Feldbacher, R., and Heindler, M. Parametric analysis of p-B11 as advanced reactor fuel. In *Proc. 10th Int. Conf. Plasma Physics and Controlled Nuclear Fusion Research (1984)* (1987), pp. 429–40.

[26] Kruglyakov, E. P., Dimov, G. I., and Koidan, V. S. Recent progress in mirror studies at Novosibirsk. *Transactions of Fusion Science and Technology 47*, 1T (2005), 1–8.

[27] Kwon, M., and et al. Progress in the study of rf heating and stabilization on hanbit mirror device. *Transactions of Fusion Science and Technology 47*, 1T (2005), 17–22.

[28] Linde, T. J. *A Three-Dimensional Adaptive Multifluid MHD Model of the Heliosphere*. PhD thesis, The University of Michigan, 1998.

[29] McNally, J. R. Physics of fusion fuel cycles. *Nuclear Technology/Fusion 2* (1982), 9–28.

[30] Mirnov, V. V., and Ryutov, D. D. Linear gasdynamic system for plasma confinement. *Soviet Technical Physics Letters 5*, 6 (1979), 279–280.

[31] Nevins, W. M. A review of confinement requirements for advanced fuels. *Journal of Fusion Energy 17*, 1 (1998), 25–32.

[32] Perkins, L. J., Hammer, J. H., and Drake, R. P. Fusion, the competition, and the prospects for alternative fusion concepts. In *Current Trends in International Fusion Research*, Panarella, Ed. 1997, ch. 23.

[33] Post, R. F. Review paper: The magnetic mirror approach to fusion. *Nuclear Fusion 27*, 10 (1987), 1579–739.

[34] Powell, K. G., Roe, P. L., Linde, T. J., Gombosi, T. I., and De Zeeuw, D. L. A solution-adaptive upwind scheme for ideal magnetohydrodynamics. *Journal of Computational Physics 154* (1999), 284–309.

[35] Powell, K. G., Roe, P. L., Myong, R. S., Gombosi, T. I., and De Zeeuw, D. L. An upwind scheme for magnetohydrodynamics. In *AIAA 12th Computational Dynamics Conference* (1995). AIAA Paper 95-1704.

[36] Rose, D. J., and Clark, M. P. *Plasmas and Controlled Fusion*. MIT Press, 1961.

[37] Sedwick, R., Zayas, D., and Kerrebrock, J. Magnetohydrodynamic vortex containment for gas core nuclear propulsion, part 1: Concept overview. *Journal of Propulsion and Power 23*, 1 (2007), 81–89.

[38] Sedwick, R., Zayas, D., and Kerrebrock, J. Magnetohydrodynamic vortex containment, part 2: Equilibrium of uranium fluoride fuel in hydrogen propellant. *Journal of Propulsion and Power 23*, 1 (2007), 90–98.

[39] Smith, B. M., Knight, T. W., and Anghaie, S. Overview of nuclear MHD power conversion for multi-megawatt electric propulsion. In *Space Technology and Applications International Forum-2001* (2001), El-Genk, Ed., American Institute of Physics, pp. 916–22.

[40] Stacey, W. M. *Fusion Plasma Physics*. John Wiley & Sons, 2005.

[41] Tidman, D. A., and Krall, N. A. *Shock Waves in Collisionless Plasmas*. John Wiley & Sons, 1971.

[42] Venkatakrishnan, V. Convergence to steady state solutions of the Euler equations on unstructered grids with limiters. *Journal of Computational Physics 118* (1995), 120–30.